UNIVERSITY OF Southampton

FACULTY OF ENGINEERING AND THE ENVIRONMENT

AERODYNAMICS AND FLIGHT MECHANICS RESEARCH GROUP

High-fidelity flow simulations of electroactive membrane wings

by

Giampaolo Cetraro

Thesis for the degree of Doctor in Philosophy

3rd June 2017

Abstract

This work is inspired by natural flyers such bats and insects. They show outstanding aerodynamic performance due to their flexible membrane wings and their ability to control its stiffness to improve manoeuvrability. In this work the fluid-structure coupling as well as the physics and the control of electroactive membranes have been simulated in a multiphysics framework. This study has allowed not only to have an insight of the flow mechanisms which allow a membrane wing to enhace lift and delay stall at high angles of attack but also lays the basis of the understanding of how an active control of the membrane's stiffness in response to the unsteadiness of the fluid-structure coupling can deliver a more stable flight. In particular, numerical simulations are conducted for an electroactive membrane wing in a laminar incompressible flow. The fluid-structure interaction problem is simulated for electroactive polymers whose shape and stiffness can be modified by applying an electric potential. The Maxwell stresses generated by the electric field across the membrane produce an in-plane relaxation. Results from this work show that a fixed voltage applied to a prestretched membrane results in an increased camber and therefore enhanced mean lift. Moreover, the effect of a partial activation is considered as well as an oscillating voltage across the membrane. The results presented in this work indicate that the lift is increased at angles of attack up to $\alpha = 12^{\circ}$ when the back section of the membrane is activated. In addition, lift is increased at higher angles of attack when the voltage oscillates at frequencies close to resonance of the coupled fluid-structure system. Finally, an active control has been simulated exploiting the electromechanical characteristics of electroactive polymers and using the membrane itself as a sensor. This work shows that when the whole surface of the membrane is used as sensor and actuator, a proportional integral control is able to reduce the membrane's oscillations at medium angles of attack, delivering a more stable flight and smoother response to a gust.

Acknowledgements

Thanks to my supervisors prof. Richard Sandberg and prof. Owen Tutty for giving me the opportunity of doing this research and for their support.

The author is grateful for the funding provided by EPSRC under grant number EP/J001465/1.

Declaration

I, Giampaolo Cetraro, declare that the thesis entitled *High-fidelity flow simulations of electroactive membrane wings* and the work presented in the thesis are both my own, and have been generated by me as the result of my original research. I confirm that:

1. This work was done wholly while in candidature for a research degree at this University;
2. Where any part of this thesis has previously been submitted for a degree or any other qualification at this University or any other institution, this has been clearly stated;
3. Where I have consulted the published work of others, this is always clearly attributed;
4. Where I have quoted from the work of others, the source is always given. With the exception of such quotations, this thesis is entirely my own work;
5. I have acknowledged all main sources of help;
6. Where the thesis is based on work done by myself jointly with others, I have made clear exactly what was done by others and what I have contributed myself;
7. Either none of this work has been published before submission, or parts of this work have been published as reported in Section 5.

Signed:
Date:

Contents

List of Figures

List of Tables

Nomenclature

Fluid:

α	angle of attack (AoA)	$[^\circ]$
p	pressure	$[\mathrm{N/m^2}]$
ν	kinematic viscosity	$[\mathrm{m^2/s}]$
ρ_f	fluid density	$[\mathrm{kg/m^3}]$
Re	Reynolds number	[-]
$\boldsymbol{U}$	velocity vector	$[\mathrm{m/s}]$
U_∞	freestream velocity	$[\mathrm{m/s}]$

Structure:

$\boldsymbol{B}, \boldsymbol{C}$	left and right Cauchy-Green deformation tensors	[-]
c	chord	$[\mathrm{m}]$
$\boldsymbol{E}$	Green-Lagrange strain tensor	[-]
E	Young modulus	$[\mathrm{N/m^2}]$
$\boldsymbol{F}$	deformation gradient tensor	[-]
h	thickness	$[\mathrm{m}]$
J	Jacobian, volume ratio ($= \det\boldsymbol{F}$)	[-]
κ	Bulk modulus	$[\mathrm{N/m^2}]$
λ, μ	Lamé parameters	$[\mathrm{N/m^2}]$
ν_p	Poisson's ratio	[-]

ρ_s	solid density	$[\mathrm{kg/m^3}]$
$\boldsymbol{\sigma}_e$	Cauchy (elastic) stress tensor	$[\mathrm{N/m^2}]$
$\boldsymbol{P}, \boldsymbol{S}$	1st and 2nd Piola-Kirchhoff stress tensors	$[\mathrm{N/m^2}]$
$\boldsymbol{u}$	displacement vector ($= \boldsymbol{x} - \boldsymbol{X}$)	$[\mathrm{m}]$
$\boldsymbol{v}$	solid velocity vector	$[\mathrm{m/s}]$
$\boldsymbol{x}$	current position vector	$[\mathrm{m}]$
$\boldsymbol{X}$	reference position vector	$[\mathrm{m}]$

Electrostatics:

$\mathbf{E}$	Electric field vector	$[\mathrm{kg\ m/s^3A}]$
ε_0	electric permittivity of vacuum	$[\mathrm{s^4A^2/kg\ m^3}]$
ε_R	relative dielectric permittivity	$[\text{-}]$
$\boldsymbol{J}$	current density	$[\mathrm{A/m^2}]$
k	electrical conductivity	$[\mathrm{s^3A^2/kg\ m^3}]$
ϕ	electric potential	$[\mathrm{kg\ m^2/s^3A}]$
ρ_c	charge density	$[\mathrm{s\ A/m^3}]$
$\boldsymbol{\sigma}_m$	Maxwell stress tensor	$[\mathrm{N/m^2}]$

Acronyms

ALE	Arbitrary Lagrangian Eulerian
AR	Aspect Ratio
CSM	Computational Structural Mechanics
CFD	Computational Fluid Dynamics
CV	Control Volume
DE	Dielectric Elastomers
DNS	Direct Numerical Simulation
EAP	Electroactive Polymers
FE	Finite Element
FV	Finite Volume
FSI	Fluid-Structure Interaction
OpenFOAM	Open Field Operation And Manipulation
LE	Leading Edge
MAV	Micro Air Vehicle
PISO	Pressure Implicit with Splitting of Operators
PIV	Particle Image Velocimetry
SIMPLE	Semi Implicit Method for Pressure Linked Equations
TE	Trailing Edge

Mathematical Notation

Throughout this work the following notation is adopted for tensor operations:

Inner product The inner product $(\cdot)$ operates on any two tensors of rank r_1 and r_2 such that the rank of the result $r = r_1 + r_2 - 2$. In particular:

- The inner product of two vectors $\boldsymbol{a}$ and $\boldsymbol{b}$ is commutative and produces a scalar $s = \boldsymbol{a} \cdot \boldsymbol{b}$ where

$$s = a_i b_i = a_1 b_1 + a_2 b_2 + a_3 b_3.$$

- The inner product of two tensors $\boldsymbol{T}$ and $\boldsymbol{S}$ produces a tensor $\boldsymbol{P} = \boldsymbol{T} \cdot \boldsymbol{S}$ whose components are evaluated as

$$P_{ij} = T_{ik} S_{kj}.$$

  It is non-commutative such that $\boldsymbol{T} \cdot \boldsymbol{S} = \left(\boldsymbol{S}^T \cdot \boldsymbol{T}^T \right)^T$.

Outer product or tensor product The outer product $(\otimes)$ of two vectors $\boldsymbol{a}$ and $\boldsymbol{b}$ is non-commutative and produces a tensor $\boldsymbol{T} = \boldsymbol{a} \otimes \boldsymbol{b} = (\boldsymbol{b} \otimes \boldsymbol{a})^T$ whose components are evaluated as

$$T_{ij} = a_i b_j.$$

Double inner product or double contraction of two tensors It produces a scalar $s = \boldsymbol{A} : \boldsymbol{B}$ which can be evaluated as the sum of the 9 products of the tensor components

$$s = A_{ij} B_{ij} = A_{11} B_{11} + A_{12} B_{12} + A_{13} B_{13} + \ldots$$

Chapter 1

Introduction

The interest in the research area of Micro Air Vehicle (MAV) is rapidly increasing. Development is driven by applications for civil and military purposes such as aerial photography, search-and-rescue or surveillance missions. In fact, one of the main advantages of these micro aircrafts is that they can perform remote observation of hazardous environments inaccessible to ground vehicles. MAVs have a set of constraints which are, in many ways, significantly different from those of conventional aircraft and are often best addressed by a multidisciplinary approach. Fast-response non-linear controls, nano-structures, integrated propulsion and lift mechanisms, highly flexible structures, and low Reynolds number ($Re \leq 10^5$) aerodynamics are just a few of the important features which may be combined for the development of a MAV. Furthermore, the rising development in miniaturized electronic systems is enabling many rapid advances in insect-sized aircraft. Also, many improvements have been done in the field of electroactive polymers used as artificial muscles. This technology looks very promising for applications such as bio-inspired MAVs. In fact birds and insects flying at low Reynolds number use membrane wings to control perfectly their attitude and manoeuvers. Not only the intrinsic membrane flexibility can deliver better aerodynamic performance than a fixed airfoil but the ability to modify its stiffness in response to the external flow conditions is the key factor to obtain an outstanding flight control.

The physics involved in the development of such devices is very complex and is not limited to the flow physics of a deformable membrane. In fact the design of electroactive membranes requires the understanding of non-linear (hyperelastic) constitutive law as well as electrostatics and electromechanical coupling. In order to address all these aspects a multi-physics simulation environment has been developed in this research with the OpenFOAM toolbox in order to help the design of electroactive membrane wings.

1.1 Review of membrane wings research

Bats and gliding mammals use thin compliant wings as lifting surfaces which twist and bend during the flight to achieve better aerodynamic characteristics. These animals with flexible membranes fly at low Reynolds numbers at moderate to high angles of attack, and show excellent flight capabilities and high maneuverability [15, 119]. In the case of bats, such control is obtained by changing the level of pre-tension in their wing membrane, thus effectively changing the wing shape and camber throughout the wingbeat cycle [29, 118, 123]. As consequence of its intrinsic flexibility, a membrane wing can delay stall at high angle of attack [77] as well as enhance its aerodynamic performance (i.e. lift-to-drag ratio) by controlling flow separation [109]. These flexibility effects on the wing aerodynamics are confirmed by a recent biological experiment [89], where bumblebees with experimentally manipulated wing stiffness showed an 8.6 per cent reduction in the vertical component of the aerodynamic force produced.

These characteristics, along with their light-weight nature, make membrane wings particularly suitable for MAV applications [110], especially where wind gust amplitudes are of the same order of magnitude as their flying speeds [111]. Moreover, Albertani et al. [1] have shown that membrane wings can significantly improve longitudinal static stability. These

studies have confirmed that membrane wings can be a suitable solution to make MAVs more controllable and efficient.

In order to simulate the equilibrium shapes of a membrane in steady conditions, calculations of potential flow [90], laminar flow [114], and turbulent flow [116] have been performed. It has been found that the potential flow theory is reliable only at low incidences. For higher incidences, viscous effects and flow separation need to be included for accurate simulations in steady flow. In particular, Smith and Shyy [114] showed that results from numerical simulation of the aeroelastic membrane wing problem in a steady laminar flow using the Navier-Stokes equations were significantly different than those from the potential theory at $Re = 10^3 - 10^4$. Therefore in a laminar regime at Re in the MAV flight regime, potential flow solutions may be inadequate. Further computations [108, 115] have investigated the response of a membrane airfoil to an unsteady free stream. Deformable thin airfoils have also been studied along with rigid-body wing kinematics (flapping wing) by Walker and Patil [141]. In their work Walker and Patil extended the potential flow theory around a flat plate in rigid motion (i.e. Theodorsen model) to deformable airfoils using Chebychev polynomials. Rigid body motion is described by the first two polynomials (plunging and pitching motion) and the other polynomials account for the deformation. However the deformation in Walker and Patil paper comes from a prescribed motion and not from the result of the fluid-structure coupling. In fact the main objective of their study is to show which deformation shapes and relative phase-shift between plunging and pitching motion would lead to a maximum thrust production.

Several experimental studies have also focused on the membrane deformation characteristics. For instance, Particle Image Velocimetry (PIV) measurements on compliant membrane aerofoils at high angles of attack carried out by Rojratsirikul et al. [103] have shown that the mean membrane shape is not very sensitive to the change in angle of incidence. Numerical simulations by Gordnier [51] reported that the mean camber increases with Reynolds number and that the mean membrane deflection is almost symmetrical in the chordwise direction for low incidences. How-

ever, as the angle of attack is increased, the point of maximum camber moves forward and the mean displacement of the membrane becomes more asymmetric. Studies by Galvao et al. [48] and Song et al. [119] have also shown that membrane wings delay stall by as much as 10%, prevent flow separation, and enhance lift-to-drag ratios. Other studies have started to analyse and characterise the interaction between vortex shedding and membrane vibrations. For example, Lian and Shyy [76] reported a correlation between the vibration frequency of the membrane and the vortex shedding frequency when analyzing the unsteady laminar-turbulent transition of flows over a membrane wing. Rojratsirikul et al. [103] reported that the vibrations occur at certain modes near the natural frequencies of the membrane, and that they are larger for the second mode at post stall incidences. Song et al. [119] showed that membrane deflection could be successfully approximated by a parabola and they presented a simple theoretical model to predict the membrane camber due to the aerodynamic loading. The model assumes that the membrane behaves like a linearly elastic material with Young's modulus, E, which is independent of strain. However, in reality, membranes have a strain dependent Young's modulus and exhibit an inverted J-shape stress-strain curve.

1.2 Review of Fluid-Structure Interaction

An effective development of a bio-inspired MAV concept will require a deep understanding of the unsteady aerodynamics at low Re and the associated Fluid-Structure Interaction (FSI). The intrinsic flexibility of membrane wings generates strong coupling between the unsteady fluid dynamics and the structural response, giving rise to tightly integrated, multidisciplinary physics. In fact, membrane wings may be subject to aeroelastic instabilities, which may limit their operating envelope, even when they operate in steady free stream at low incidences. Thus, a deep understanding of the FSI problem is needed.

Apart from membrane wings, a wide range of applications have been

studied exploiting FSI techniques in recent years. Some of them include yacht sails [8, 79, 131], parachutes [120, 149] and other fabric dynamics [11, 105], rotor dynamics [21, 47], and a vast number of biomedical applications including arterial blood flow [44, 50, 57], aortic heart valves [32, 140], and aortic aneurysms [128, 148].

Typically, in FSI modeling there are two main approaches: *monolithic* (direct) and *partitioned* (segregated). In the monolithic approach the governing equations for the fluid and the solid domains are expressed in terms of the same primitive variables (usually pressure and velocity [53]), and are solved simultaneously using a single large system of nonlinear equations. A big advantage of a monolithic approach is the use of a single domain where the fluid and solid characteristics are specified, which can lead to improved solution stability. Unfortunately some drawbacks to this approach are the requirement of highly complex and specialized software [37], the inefficiencies of using a single time step for all domains even if different time scales are present [59], the use of a single mesh which creates a challenge to have a grid of suitably high quality for both domains [112].

On the other hand, the partitioned scheme has gained popularity because of its modularity and possible re-use of separate efficient solvers [84]. The most important advantages of the partitioned approach are the ability to separately manage and develop the flow and structural solver [84, 121] and to employ separate meshes for the structure and the fluid, which often require different mesh resolutions. The known drawbacks to this approach are reported as the need to accurately and efficiently couple the two domains on the interface between fluid and solid [121], and the degradation of solution stability due to small errors in this coupling [39], as well as poor solution stability for weakly coupled schemes, or computationally expensive sub-iterations of a strongly coupled scheme [86] .

Partitioned methods can be further classified into *weak* [38] and *strong* coupling [100]. Strong coupling enforces continuity of velocity and stress at the fluid-solid interface through fixed-point iterations or Newton-type iterations at each time step [44], while weak coupling requires only one so-

lution of each field per time step in a sequentially staggered manner and is thus particularly appealing in terms of efficiency. Weak coupling could produce reasonable results when the coupling is not tight as in aeroelasticity problems of full-scale airplanes, where the time lag between the flow solution and the structural solution can be generally neglected and does not affect the accuracy and stability of the results [38]. However, when the density of the solid is comparable to that of the fluid as in hemodynamics or for fabric materials, a tighter coupling between fluid and structure is required as an additional fluid acceleration acting on the solid – referred to as *added mass effect* – may destabilize a weakly coupled numerical scheme [26, 46]. In fact in weakly coupled schemes the fluid forces are calculated for the predicted structural displacements rather than for the correct ones. Therefore a large difference between predicted and actual displacement might lead to incorrect results and instability issues.

On the contrary the simple fixed-point iterations used in strong coupling problems may either not converge or be computationally expensive due to the large number of iterations in case of intnse interaction. For this reason Mok et al. [87] introduced Aitken acceleration to FSI with a dynamic relaxation factor for enhanced robustness and stability. To increase computational efficiency, Fernandez et al. [41] proposed a semi-implicit coupling scheme based on the pressure correction method where only the pressure is coupled with the structure while non-linear and viscous terms are updated explicitly. A semi-implicit coupling scheme using algebraic splitting has also been proposed by Quaini and Quarteroni [99]; this approach shares a similar efficiency increase as the scheme of Fernandez et al. [41].

Even though the partitioned approach requires a particular attention at the fluid-solid interface to ensure an accurate and stable solution, the use of a strong coupled algorithm can provide results that are equivalent to those from a monolithic approach [6, 20, 84].

1.3 Review of Finite Volume Method for structures

The computional modeling of FSI involves a combination of solvers, typically a Finite Volume (FV) solver for the flow domain, a Finite Element (FE) solver for the structural analysis and a third code for coupling, data interpolation and simulation management. FV methods traditionally use low-order approximations on structured or unstructured meshes and iterative solvers while FE methods often use high-order elements on unstructured meshes using direct solvers. The different approaches of the two methods impose limitations on the way of coupling and might create issues in the model setup. It has been shown that for many applications the two techniques are equivalent and the difference between FE and FV discretization of second-order accurate, partial differential equations is small [60]. For this reason and to overcome the drawback of coupling FE and FV solvers, some attempts have been made to model the entire FSI framework in the context of FE [142] or FV [68, 112] methods.

With regard to FV analysis, its usage has gained popularity in Computational Structural Mechanics (CSM) from the early 90's due to the attractively simple but strongly conservative nature of the method [36, 83]. At present, the FV method has been applied to a large range of stress analysis problems in linear-elasticity [64, 113, 143], thermo-elastoplasticity [33], incompressible elasticity [14], contact mechanics [22] as well as fluid–structure interactions [53, 54, 68, 69, 112]. Moreover, solid mechanics solvers have been recently included in the OpenFOAM-extend version [98], including solvers for non-linear elasticity in the Total or Updated Lagrangian formulation [23, 132]. These FV solvers as well as the linear elastic solver developed by Jasak and Weller [64] are based on

- the second-order accurate discretization on control volumes of arbitrary polyhedral shape,
- a segregated solution procedure, in which the displacement components are solved consecutively and

- iterative solvers for the systems of linear algebraic equations.

The Total and Lagrangian formulation are used to describe large strain and large rotation which can occur in the nonlinear analysis of a membrane. These formulations are implemented in OpenFOAM for materials with a Saint Venant-Kirchhoff constitutive equation, which is the simplest hyper-elastic material model being just an extension of the linear elastic law to the nonlinear regime. An incompressible Mooney-Rivlin constitutive equation has been studied with the FV method by Bijelonja et al. [14]. In order to deal with incompressibility, the hydrostatic pressure which features in the constitutive equation, has been treated as an additional dependent variable and calculated with a Semi-Implicit Method for Pressure-Linked Equations (SIMPLE) algorithm [94].

A big advantage of using the finite volume method for solid mechanics rather than the finite element one is that when dealing with (nearly) incompressible matherials (Poisson ratio ν_p approaching 0.5) results are not affected by the locking effect. Locking is a numerical error that occurs in FE analysis due to the linear nature of quadrilateral elements. The linear elements do not accurately model the curvature present in the actual material under bending, and a shear stress is introduced. The additional fictitious shear stress causes the element to reach equilibrium with smaller displacements, i.e. FE methods produce results showing stiffness far greater then would be expected, rendering the results useless [9]. On the contrary for the range of cases simulated by Bijelonja et al. [14], the FV method appears to be locking free.

Therefore using the FV method can be very beneficial when dealing with fluid-structure interaction problems. Not only the FVM is locking free and strongly conservative for large deformations, but it is also very efficient in terms of coupling with a FVM fluid solver especially if both fluid and solid solver belongs to the same simulation tool box. In fact no external applications needs to be run and the data between fluid and solid are exchanged more efficiently as they are already in the same format. Ultimately fluid and solid solver can be seen as modules of the OpenFOAM toolbox allowing easier extension to other physics models, e.g. multiphase

or turbulent flow, solid plasticity or viscoelasticity, etc.

1.4 Review of Electro Active Polymers

The most effective way to activate a membrane is by means of Dielectric Elastomers (DE). They belong to the category of electroactive polymers (EAPs) as they convert electric energy into mechanical work exploiting the electrostriction phenomenon. This technology, also known as artificial muscle [25, 95], has been intensely studied in the last few years because of its attractive features such as large deformation, fast response, light weight, silent operation and low cost [18]. EAPs have been widely used for diverse applications, including robotics [96], motors [2], adaptive optics [13] and bioengineering [45].

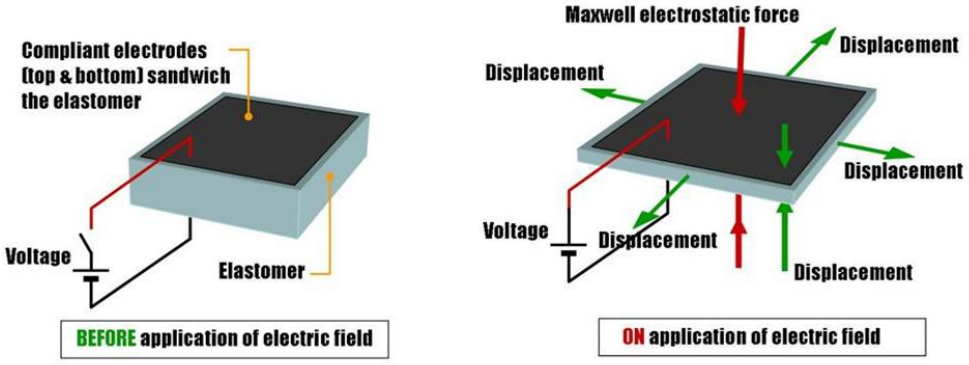

Figure 1.1: Schematics of a dielectric elastomer [122].

EAPs essentially consist of an elastomeric film coated on both sides with compliant electrodes (Fig. 1.1). These electrodes act as a capacitor: when a voltage is applied the electrostatic force generates a compressive pressure which squeezes the dielectric in the thickness direction, causing a stretching in the other two directions (expansion in area). The achievable voltage-induced deformation is strongly affected by how mechanical loads are pre-applied. Using an acrylic elastomer, experiments have demonstrated voltage-induced expansion in area by 160% with a membrane biaxially prestretched and fixed to a rigid frame [95], by 488% with

a membrane subject to biaxial dead loads [58], and by 1692% with a membrane mounted on a chamber of air [70]. It has been shown that prestretch is needed to eliminate the pull-in instability [74] (such that the elastomer thins down drastically, leading to electric breakdown rather than actuation), and to improve electric breakdown strength [73].

Since DE can achieve very large strains with a highly non-linear behaviour, their constitutive equation needs to be modelled with a *hyperelastic* formulation. Hyperelastic models can be classified into *phenomenological* or *micro-mechanical*. The latter are derived from statistical mechanics arguments on networks of idealised chain molecules. Examples for micro-mechanical models are the 3-chain, 4-chain, 8-chain models as well as the unit sphere (21-chain) model which have all been shown to be appropriate for moderate to large elastic deformations of rubber-like materials [5]. On the other hand, a phenomenological formulation of a hyperelastic material is based on the scalar quantity *strain energy function*, which depends either on the invariants of the right (or left) Cauchy-Green strain tensor or on the principal stretches, i.e. the eigenvalues of the Cauchy-Green tensor. The relations between invariants (I_i) and principal stretches (λ_i) are the following

$$
\begin{aligned}
&I_1(\boldsymbol{C}) = I_1(\boldsymbol{B}) = \mathrm{tr}(\boldsymbol{C}) = \lambda_1^2 + \lambda_2^2 + \lambda_3^2, \\
&I_2(\boldsymbol{C}) = I_2(\boldsymbol{B}) = \tfrac{1}{2}\left[\mathrm{tr}^2(\boldsymbol{C}) - \mathrm{tr}\left(\boldsymbol{C}^2\right)\right] = \lambda_1^2\lambda_2^2 + \lambda_2^2\lambda_3^2 + \lambda_1^2\lambda_3^2, \\
&I_3(\boldsymbol{C}) = I_3(\boldsymbol{B}) = \det(\boldsymbol{C}) = \lambda_1^2\lambda_2^2\lambda_3^2,
\end{aligned}
$$

where $\boldsymbol{C} = \boldsymbol{F}^T\boldsymbol{F}$ (or $\boldsymbol{B} = \boldsymbol{F}\boldsymbol{F}^T$) is the right (or left) Cauchy-Green tensor with $\boldsymbol{F} = \partial\boldsymbol{x}/\partial\boldsymbol{X}$ being the deformation gradient (i.e. the derivative of each component of the deformed $\boldsymbol{x}$ vector with respect to each component of the reference $\boldsymbol{X}$ vector). Among the numerous phenomenological approches, the Odgen model [92] is very flexible in modelling rubber-like materials, especially due to its modular polynomial formulation in terms of principal stretches which additionally makes it manageable with mathematical analysis. Also widely used and of earlier origin are models of Mooney-Rivlin type [88, 102], which are formulated in strain invariants.

Its simplest realisation, called neo-Hookean model, is closely related to micro-mechanical approaches since it coincides with a 3-chain model using Gaussian chain statistics.

The main challenge in designing invariant-based models is to choose an appropriate (sub)set of invariants and to include sufficiently high orders of them into the strain energy function. As pointed out by Yeoh [150], cubic terms of I_1 are able to reproduce the highly nonlinear, S-shaped uniaxial behaviour of rubber, also at very large strains.

A higher order elasticity model, composed of a neo-Hookean-like compressible and a generalised Mooney-type incompressible component, has been proposed by Attard and Hunt [7] and was proven to perform excellently on experimental data of uniaxial and (equi)biaxial tension by Vangerko and Treloar [136] and pure shear by Penn [97]. In particular, it is pointed out that this formulation is capable of reproducing the Valanis–Landel hypothesis [134], which states that interactions of principal stresses are governed only by compressive deformation parts whereas the incompressible strain energy density is represented by a superposition of terms dependent on the principal stretches.

When a numerical simulation of a DE is performed, good agreement with experimental data is achieved using a neo-Hookean formulation [124]. As a prestretch is needed for the electroactuation, a stretch-stiffening behaviour of the membrane might occur. In an elastomer, each individual polymer chain has a finite contour length. When the elastomer is subject to no loads, the polymer chains are wound, allowing a large number of conformations. Subject to loads, the polymer chains extend. As the loads increase, each polymer chain approaches its maximum unwinded length, and the elastomer approaches a limiting stretch. On approaching the limiting stretch, the elastomer stiffens steeply. To take into account this effect, a small modification to the neo-Hookean model can be made introducing a material constant related to the limiting stretch [80].

1.5 Aim of the project

The design of an electroactive membrane wing for micro air vehicle applications is a very complex process. Experiments are required in order to have a useful insight of the flow physics involved in the fluid-structure coupling as well as to understand the potential and the limitations of dealing with dielectric elastomers operating at high voltages. At the same time a high fidelity computational model is essential in this kind of problems not only because it allows to measure field variables (e.g. pressure and velocity for the fluid, stress and strains for the structure), detect vortical structures, separation and reattachment points in a non-intrusive way, but also because it can provide a valuable tool for the system identification which can be used for the control system design of an actuated membrane wing. Moreover, a numerical model allows freedom of choice on the boundary conditions to be applied. In fact it is possible to evaluate the effect on the system performance of perfectly-rigid supports or find the ideal material properties (stiffness, constitutive equation) which leads to optimal flight characteristics.

To the author's knowledge the numerical studies conducted so far have focused mainly on passive membrane wings and the main effort has been done mostly on the flow solver fidelity and little effort has been done on the structural and control side. However for a bio-inspired membrane, large stretch capabilities need to be addressed with an accurate hyperelastic constitutive law as well as the possibility to control the membrane's stiffness in response to the unsteadiness of the flow. In this context the effort of the present work is to lay the basis for the design of a multiphysics framework where the fluid-structure coupling as well as the electromechanical coupling can be predicted in a fully integrated simulation environment. For this purpose the whole code development in this thesis has been done with the OpenFOAM toolbox. OpenFOAM is an open-source collection of libraries and applications written in C++ specifically designed to solve partial differential equation with the finite volume method using a relatively easy code syntax. It is nowadays widely used by

the scientific community in the academia and in the industry not only because it has proven itself to produce the same performance and accuracy of commercial CFD software, but especially because it offers the freedom of implementing custom solvers and modules which can be efficiently combined together. The physics modules developed during this thesis will be made available to the OpenFOAM community.

Chapter 2

Governing Equations

This chapter presents the equations used throughout the thesis to characterize the physics of the flow and the structure as well as the way the membrane is controlled. The Navier-Stokes equations for a laminar incompressible flow are derived in Section 2.1. The kinematics and equation of motion of the membrane are presented in Section 2.2 as well as the derivation of a Neo-Hookean constitutive law in its incremental form. The electrostriction effects on the membrane's stiffness are described in Section 2.3. Finally the fundamental principles of the control theory are given in Section 2.4.

2.1 Fluid dynamics

The governing equations for a viscous fluid flow, known as the *Navier-Stokes equations*, are a coupled set of non-linear partial differential equations [3]. They can be derived from conservation of mass, momentum and energy within an infinitesimally small spatial control volume.

For mass conservation, the following continuity equation is obtained:

$$\frac{\partial \rho_f}{\partial t} + \boldsymbol{\nabla} \cdot (\rho_f \boldsymbol{U}) = 0, \tag{2.1}$$

where ρ_f $\left[\mathrm{kg/m^3}\right]$ is the fluid density, $\boldsymbol{U}$ $[\mathrm{m/s}]$ is the flow velocity vec-

tor and the differential operator divergence, $\boldsymbol{\nabla}\cdot$, operating on the velocity vector field $\boldsymbol{U}$ produces a scalar defined as

$$\boldsymbol{\nabla}\cdot\boldsymbol{U} = \frac{\partial U_x}{\partial x} + \frac{\partial U_y}{\partial y} + \frac{\partial U_z}{\partial z}.$$

For momentum conservation the following expression can be derived from Newton's second law (neglecting gravity and additional body forces):

$$\frac{\partial\left(\rho_f \boldsymbol{U}\right)}{\partial t} + \boldsymbol{\nabla}\cdot\left(\rho_f \boldsymbol{U}\otimes\boldsymbol{U}\right) = \boldsymbol{\nabla}\cdot\sigma, \tag{2.2}$$

where σ $\left[\mathrm{N/m^2}\right]$ is the Cauchy stress tensor, which express the relationship between stress and strain for a viscous fluid element. The outer product, $\otimes$, operating on the vector $\boldsymbol{U}$, generates a symmetric tensor whose components are evaluated as

$$\boldsymbol{U}\otimes\boldsymbol{U} = U_i U_j = \begin{pmatrix} U_1^2 & U_1U_2 & U_1U_3 \\ U_1U_2 & U_2^2 & U_2U_3 \\ U_1U_3 & U_2U_3 & U_3^2 \end{pmatrix}.$$

Here the divergence operator applied to second rank tensor fields (i.e. $\boldsymbol{U}\otimes\boldsymbol{U}$ and σ) produces a vector, e.g.

$$\boldsymbol{\nabla}\cdot\boldsymbol{\sigma} = \partial_i\sigma_{ij} = \begin{pmatrix} \partial\sigma_{11}/\partial x_1 + \partial\sigma_{21}/\partial x_2 + \partial\sigma_{31}/\partial x_3 \\ \partial\sigma_{12}/\partial x_1 + \partial\sigma_{22}/\partial x_2 + \partial\sigma_{32}/\partial x_3 \\ \partial\sigma_{13}/\partial x_1 + \partial\sigma_{23}/\partial x_2 + \partial\sigma_{33}/\partial x_3 \end{pmatrix},$$

hence the momentum equation needs to be solved for each of the 3 velocity components (U_x, U_y, U_z).

In the range of operation of a membrane wing the flow can be considered incompressible and the viscosity constant. With these assumptions the energy equation is decoupled from the mass and momentum conservation equation [3] and therefore has been neglected.

In order to close the system of four equations (2.1) and (2.2), constitu-

tive relations are needed. For a Newtonian[1] fluid and incompressible flow, the Cauchy stress tensor, $\boldsymbol{\sigma}$, is defined as

$$\boldsymbol{\sigma} = -p\boldsymbol{I} + \eta\left(\boldsymbol{\nabla u} + \boldsymbol{\nabla u}^{\mathrm{T}}\right),$$

where $\boldsymbol{I}$ represents the identity tensor, $p\,[\mathrm{N/m^2}]$ is the pressure, $\eta\ \left[\mathrm{N\,s/m^2}\right]$ is the dynamic viscosity and the differential operator gradient, $\boldsymbol{\nabla}$, applied to a vector produces a second rank tensor, namely in index notation $\boldsymbol{\nabla u} = \partial_i U_j$.

The equations (2.1) and (2.2) can be simplified for the incompressible case to the following expressions

$$\boldsymbol{\nabla} \cdot \boldsymbol{u} = 0$$

$$\frac{\partial \boldsymbol{u}}{\partial t} + \boldsymbol{\nabla} \cdot (\boldsymbol{u} \otimes \boldsymbol{u}) = -\boldsymbol{\nabla}\frac{p}{\rho_f} + \nu\boldsymbol{\nabla}^2\boldsymbol{u},$$

where $\nu = \eta/\rho_f\ \left[\mathrm{m^2/s}\right]$ is the kinematic viscosity.

Micro Air Vehicles operate at Reynolds numbers ranging between $Re = 2500 - 20000$. The Reynolds number is defined for a flow as the ratio between inertial and viscous forces. In particular insects such butterflies or small mammals like bats set the operation range of membrane wings in the lower boundary of the foramended range. In fact in these regimes the viscous forces have a significant role in the flow evolution which is characterised by unsteady large coherent structures. At such low Reynolds numbers the Navier-Stokes equations can be solved directly without any turbulence modeling [3].

[1]The Newtonian model of fluid response is based on the assumption that in a fluid particle the shear stress is proportional to the rate of shear strain.

2.2 Structural dynamics

2.2.1 Kinematics

In finite deformation analysis, there are different definitions of deformation and strain. All of them are expressed in terms of the deformation gradient tensor, $\boldsymbol{F}$, which is defined as the derivative of each component of the deformed $\boldsymbol{x}$ vector (current position) with respect to each component of the reference $\boldsymbol{X}$ vector (initial position) [55]

$$\boldsymbol{F} = \frac{\partial \boldsymbol{x}}{\partial \boldsymbol{X}} = \frac{\partial x_i}{\partial X_j} = \begin{bmatrix} \frac{\partial x_1}{\partial X_1} & \frac{\partial x_1}{\partial X_2} & \frac{\partial x_1}{\partial X_3} \\ \frac{\partial x_2}{\partial X_1} & \frac{\partial x_2}{\partial X_2} & \frac{\partial x_2}{\partial X_3} \\ \frac{\partial x_3}{\partial X_1} & \frac{\partial x_3}{\partial X_2} & \frac{\partial x_3}{\partial X_3} \end{bmatrix}.$$

It is more convenient to express the deformation gradient in terms of the *displacement* vector $\boldsymbol{u} = \boldsymbol{x} - \boldsymbol{X}$ (Fig. 2.1a):

$$\boldsymbol{F} = \frac{\partial (\boldsymbol{X} + \boldsymbol{u})}{\partial \boldsymbol{X}} = \boldsymbol{I} + \frac{\partial \boldsymbol{u}}{\partial \boldsymbol{X}} = \boldsymbol{I} + \nabla \boldsymbol{u}.$$

For realistic deformation not all the off-diagonal components of the deformation gradient are non-zero [81] and therefore the determinant is always given by $\det(\boldsymbol{F}) = \frac{\mathrm{d}x_1}{\mathrm{d}X_1}\frac{\mathrm{d}x_2}{\mathrm{d}X_2}\frac{\mathrm{d}x_3}{\mathrm{d}X_3}$. It can be noted that this is the volume ratio between the current and initial configuration $\frac{\mathrm{d}x_1}{\mathrm{d}X_1}\frac{\mathrm{d}x_2}{\mathrm{d}X_2}\frac{\mathrm{d}x_3}{\mathrm{d}X_3} = \frac{dV_c}{dV_0}$. Therefore, for realistic deformation, the Jacobian must satisfy the condition

$$J = \det(\boldsymbol{F}) > 0.$$

The deformation gradient $\boldsymbol{F}$ can be decomposed in a pure rotation matrix $\boldsymbol{R}$, and in the right (or left) stretch tensor $\boldsymbol{U}$ (or $\boldsymbol{V}$), the latter being symmetric by definition (Fig. 2.1b)

$$\boldsymbol{F} = \boldsymbol{R} \cdot \boldsymbol{U} = \boldsymbol{V} \cdot \boldsymbol{R},$$

where the rotation matrix, $\boldsymbol{R}$, is a particular matrix such that its transpose

is equal to its inverse

$$\boldsymbol{R}^T = \boldsymbol{R}^{-1} \text{ or } \boldsymbol{R} \cdot \boldsymbol{R}^T = 1.$$

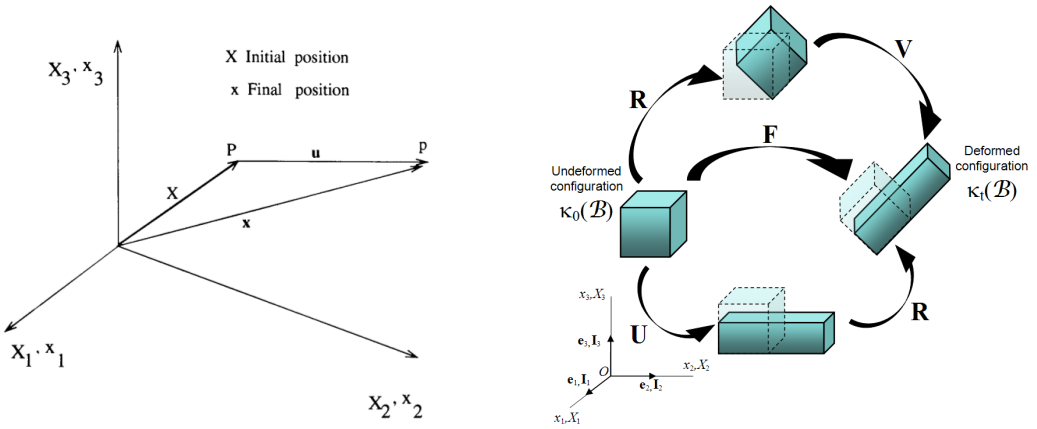

(a)

(b) Polar decomposition of the deformation gradient $\boldsymbol{F}$

Figure 2.1: Motion of a deformable body

Since a pure rotation does not induce any stress in a deformable solid, it is often convenient to use rotation-independent measures of deformation. The Right Cauchy-Green deformation tensor, $\boldsymbol{C}$, is rotation-independent and is defined as

$$\boldsymbol{C} = \boldsymbol{F}^T \cdot \boldsymbol{F} = (\boldsymbol{R} \cdot \boldsymbol{U})^T \cdot (\boldsymbol{R} \cdot \boldsymbol{U}) = \boldsymbol{U}^T \cdot \boldsymbol{R}^T \cdot \boldsymbol{R} \cdot \boldsymbol{U} = \boldsymbol{U}^T \cdot \boldsymbol{U} = \boldsymbol{U}^2$$

and similarly the Left Cauchy-Green deformation tensor, $\boldsymbol{B}$

$$\boldsymbol{B} = \boldsymbol{F} \cdot \boldsymbol{F}^T = (\boldsymbol{V} \cdot \boldsymbol{R}) \cdot (\boldsymbol{V} \cdot \boldsymbol{R})^T = \boldsymbol{V} \cdot \boldsymbol{R} \cdot \boldsymbol{R}^T \cdot \boldsymbol{V}^T = \boldsymbol{V} \cdot \boldsymbol{V}^T = \boldsymbol{V}^2.$$

By definition $\boldsymbol{C}$ and $\boldsymbol{B}$ are symmetric tensors and share the same invari-

ants which are:

$$I_1 := \mathrm{tr}\left(\mathbf{C}\right), \tag{2.3}$$

$$I_2 := \tfrac{1}{2}\left[\mathrm{tr}\left(\mathbf{C}\right)^2 - \mathrm{tr}\left(\mathbf{C}^2\right)\right], \tag{2.4}$$

$$I_3 := \det\left(\mathbf{C}\right) = J^2. \tag{2.5}$$

As measure of strain, the Green-Lagrange strain tensor, $\boldsymbol{E}$ will be used for the purpose of this work. It is defined as

$$\boldsymbol{E} = \frac{1}{2}\left(\boldsymbol{C} - \boldsymbol{I}\right) = \frac{1}{2}\left(\boldsymbol{F}^T \cdot \boldsymbol{F} - \boldsymbol{I}\right) = \frac{1}{2}\left[\nabla \boldsymbol{u}^T + \nabla \boldsymbol{u} + \nabla \boldsymbol{u}^T \nabla \boldsymbol{u}\right].$$

When large strains are considered, the definition of stress can be significantly affected by the configuration chosen as reference [81]. The following definitions of stress are considered:

Cauchy stress, σ, expresses the force per unit *deformed* area acting on surfaces on the *deformed* body (i.e. the true stress) (symmetric $\boldsymbol{\sigma} = \boldsymbol{\sigma}^T$),

1st Piola-Kirchhoff stress, $\boldsymbol{P}$, the force per unit *undeformed* area acting on surfaces on the *deformed* body (not symmetric),

2nd Piola-Kirchhoff stress, $\boldsymbol{S}$, the force per unit *undeformed* area acting on surfaces on the *undeformed* body (symmetric $\boldsymbol{S} = \boldsymbol{S}^T$).

The following relationships occur between the different definitions of stress:

$$\begin{aligned}
\boldsymbol{P} &= J\boldsymbol{F}^{-1} \cdot \boldsymbol{\sigma} = J\boldsymbol{\sigma} \cdot \boldsymbol{F}^{-T} = \boldsymbol{F} \cdot \boldsymbol{S} = \boldsymbol{S} \cdot \boldsymbol{F}^T, \\
\boldsymbol{S} &= \boldsymbol{P} \cdot \boldsymbol{F}^{-T} = \boldsymbol{F}^{-1} \cdot \boldsymbol{P} = J\boldsymbol{F}^{-1} \cdot \boldsymbol{\sigma} \cdot \boldsymbol{F}^{-T}, \\
\boldsymbol{\sigma} &= \tfrac{1}{J}\boldsymbol{F} \cdot \boldsymbol{S} \cdot \boldsymbol{F}^T = \tfrac{1}{J}\boldsymbol{P} \cdot \boldsymbol{F}^T.
\end{aligned} \tag{2.6}$$

Although the 2nd Piola-Kirchhoff stress tensor, $\boldsymbol{S}$, is difficult to use for a physical interpretation, it is useful for the mathematical material model and numerical calculations because

1. it is a symmetric tensor,

2. it is energy conjugate to the Green-Lagrange strain tensor, $\boldsymbol{E}$. The internal energy $\boldsymbol{\mathcal{E}}(t)$ of a deformable body at any time is defined as

$$\boldsymbol{\mathcal{E}}(t) = \int_{\partial B} e\rho_0 dV$$

where e is the internal energy density of the body. Also, for isothermal processes the stress power is defined as the weighted rate of the specific internal energy or $\rho_0\dot{e}$. The internal energy is special in the sense that it is a state function, that is, it is independent of the process by which a body goes from one state to another. In fact, it is a function of the material property of the body. The equation for the stress power can be derived from the kinetic energy balance of a solid body as

$$\rho_0\dot{e} = \boldsymbol{P} : \dot{\boldsymbol{F}}$$

that is, the double contraption of the 1st Piola-Kirchhoff stress tensor and the rate of deformation gradient [101]. This condition is known as energy conjugation of the stress tensor and the rate of the deformation gradient, $\dot{\boldsymbol{F}}$. This definition can be used to determine the deformation measure whose rate is the energy conjugate with the 2nd Piola-Kirchhoff stress tensor or

$$\rho_0\dot{e} = \boldsymbol{P} : \dot{\boldsymbol{F}} = \boldsymbol{S} : \dot{\boldsymbol{E}}.$$

The complete derivation can be found on the book by Debabrata Ray [101]

3. it is parameterized by material coordinates (initial configuration) only, that is, it is a material (initial) tensor field, in the same way as the Cauchy stress is a spatial (current) tensor field.

It is important to note that at small strains, the differences between various measures of stresses and strains are negligible.

2.2.2 Momentum equation

The motion of an isothermal solid in an arbitrary volume V, bounded by a surface S, is governed by the Newton's second law, which in Eulerian description reads

$$\frac{\mathrm{D}}{\mathrm{D}t}\int_V \rho_s \boldsymbol{v}\mathrm{d}V = \oint_S \boldsymbol{n}\cdot\boldsymbol{\sigma}\mathrm{d}S + \int_V \rho_s \boldsymbol{f}_b \mathrm{d}V, \tag{2.7}$$

where ρ_s is the solid density, $\boldsymbol{n}$ is the outward pointing unit normal to the surface S, $\boldsymbol{v}$ is the velocity of the solid, $\boldsymbol{\sigma}$ is the Cauchy stress tensor and $\boldsymbol{f}_b$ is the resulting body force and the operator $\frac{\mathrm{D}}{\mathrm{D}t}$ denotes material or substantial derivative. The relationship between the rate of change of the volume V and the motion of its surrounding surface is given by the space conservation law

$$\frac{\mathrm{d}}{\mathrm{d}t}\int_V \mathrm{d}V + \oint_S \boldsymbol{n}\cdot\boldsymbol{v}\mathrm{d}S = 0.$$

Writing the linear momentum conservation equation (eqn. 2.7) with respect to the initial undeformed configuration (Lagrangian formulation) requires to express the stresses with the 1st Piola-Kirchhoff stress tensor, $\boldsymbol{P} = \boldsymbol{S}\cdot\boldsymbol{F}^T$. Thus, in a *total Lagrangian* description, equation 2.7 can be written as

$$\int_{V_0}\rho_0\frac{\partial \boldsymbol{v}}{\partial t}\mathrm{d}V_0 = \oint_{S_0}\boldsymbol{n}_0\cdot\left(\boldsymbol{S}\cdot\boldsymbol{F}^T\right)\mathrm{d}S_0 + \int_{V_0}\rho_0\boldsymbol{f}_b\mathrm{d}V_0$$

where the subscripts 0 represent the quantities related to the initial configuration. When dealing with large displacements, the incremental form can be expressed as

$$\int_{V_0}\rho_0\frac{\partial \delta\boldsymbol{v}}{\partial t}\mathrm{d}V_0 = \oint_{S_0}\boldsymbol{n}_0\cdot\left(\delta\boldsymbol{S}\cdot\boldsymbol{F}^T + \boldsymbol{S}\cdot\delta\boldsymbol{F}^T + \delta\boldsymbol{S}\cdot\delta\boldsymbol{F}^T\right)\mathrm{d}S_0 + \int_{V_0}\rho_0\delta\boldsymbol{f}_b\mathrm{d}V_0$$

where δ refers to the increment of the corresponding variable, the deformation gradient tensor *increment* reads $\delta\boldsymbol{F} = (\nabla\delta\boldsymbol{u})$, and $\boldsymbol{S}$ and $\boldsymbol{F}$ are respectively the 2nd Piola-Kirchhoff stress tensor and the deformation gra-

dient at the beginning of the current time increment.

The incremental form is also used in the *updated Lagrangian* formulation, where the last calculated configuration is used as the reference configuration. One advantage of using the updated Lagrangian formulation is that we can introduce the identity $\boldsymbol{F} = \boldsymbol{I}$ and the linear momentum equation can be simplified as

$$\int_{V_u} \rho_u \frac{\partial \delta \boldsymbol{v}}{\partial t} \mathrm{d}V_u = \oint_{S_u} \boldsymbol{n}_u \cdot \left(\delta \boldsymbol{S} + \boldsymbol{S} \cdot \delta \boldsymbol{F}^T + \delta \boldsymbol{S} \cdot \delta \boldsymbol{F}^T \right) \mathrm{d}S_u + \int_{V_u} \rho_u \delta \boldsymbol{f}_b \mathrm{d}V_u, \tag{2.8}$$

where now the subscripts u represent quantities related to the updated configuration. After updating the configuration, the accumulated 2nd Piola-Kirchhoff stress, $\boldsymbol{S}_u + \delta \boldsymbol{S}_u$ needs to be transformed for the new configuration. Such tensorial transformation is equivalent to the transformation of the 2nd Piola-Kirchhoff stress tensor into the Cauchy stress tensor for the time increment prior to the configuration update.

Given the equation of motion, the way a specific material behaves under a given load will depend on its constitutive equation, i.e. the relationship between stress and strain. For example, for a Saint Venant-Kirchhoff material the 2nd Piola-Kirchhoff and its incremental form are given by

$$\begin{aligned} \boldsymbol{S} &= 2\mu \boldsymbol{E} + \lambda \mathrm{tr}\left(\boldsymbol{E}\right) \boldsymbol{I} \\ \delta \boldsymbol{S} &= 2\mu \delta \boldsymbol{E} + \lambda \mathrm{tr}\left(\delta \boldsymbol{E}\right) \boldsymbol{I}, \end{aligned} \tag{2.9}$$

where μ and λ are the Lamé coefficients which are functions of the Young modulus, E, and the Poisson's ratio, ν_p, given by

$$\mu = \frac{E}{2\left(1+\nu_p\right)}; \qquad \lambda = \frac{E\nu_p}{\left(1+\nu_p\right)\left(1-2\nu_p\right)}. \tag{2.10}$$

The incremental form of the Green-Lagrange strain tensor, $\delta \boldsymbol{E}$,

$$\delta \boldsymbol{E} = \frac{1}{2}\left[\nabla \delta \boldsymbol{u} + \left(\nabla \delta \boldsymbol{u}\right)^T + \nabla \delta \boldsymbol{u} \cdot \left(\nabla \boldsymbol{u}\right)^T + \nabla \boldsymbol{u} \cdot \left(\nabla \delta \boldsymbol{u}\right)^T + \nabla \delta \boldsymbol{u} \cdot \left(\nabla \delta \boldsymbol{u}\right)^T \right]$$

can be simplified in the updated Lagrangian formulation by noting that

$\nabla \boldsymbol{u} = 0$:

$$\delta \boldsymbol{E} = \frac{1}{2}\left[\nabla \delta \boldsymbol{u} + (\nabla \delta \boldsymbol{u})^T + \nabla \delta \boldsymbol{u} \cdot (\nabla \delta \boldsymbol{u})^T\right]. \tag{2.11}$$

Substituting equation (2.11) into equation (2.9) leads to the final form of the incremental constitutive equation for a Saint Venant-Kirchhoff material in an updated Lagrangian formulation

$$\begin{aligned} \delta \boldsymbol{S} \;\; = \;\; & \mu\left[\nabla \delta \boldsymbol{u} + (\nabla \delta \boldsymbol{u})^T + \nabla \delta \boldsymbol{u} \cdot (\nabla \delta \boldsymbol{u})^T\right] \\ & + \lambda \mathrm{tr}\left(\nabla \delta \boldsymbol{u}\right) \boldsymbol{I} + \frac{1}{2}\lambda \left(\nabla \delta \boldsymbol{u} : \nabla \delta \boldsymbol{u}\right) \boldsymbol{I}, \end{aligned} \tag{2.12}$$

where the double inner product of two second-rank tensors, $\nabla \delta \boldsymbol{u} : \nabla \delta \boldsymbol{u}$, produces a scalar, s, being the sum of the 9 products of the tensor component

$$s = \nabla \delta u_{ij} \nabla \delta u_{ij}.$$

Introducing the constitutive equation (2.12) into equation (2.8), makes it possible to obtain a formulation where only the displacement vector increment $\delta \boldsymbol{u}$ appears as primitive variable [132].

2.2.3 Neo-Hookean hyperelastic model

The Saint Venant-Kirchhoff model is the simplest hyperelastic formulation as it represents just an extension of the linear elastic material model to the nonlinear regime. However it presents some limitations as it does not treat change in volume appropriately. Moreover it performs well for large deformations and small strains, but it produces unphysical results (infinite stresses) for large strains [55]. Therefore a more accurate model such as the Neo-Hookean one is going to be presented in this section and used to characterize the membrane.

The starting point of a hyperelastic formulation is the definition of a stored strain energy function, W, as a function of $\boldsymbol{C}$ and its invariants

$$W = W\left(I_1, I_2, I_3\right).$$

From the strain energy function the 1st and 2nd Piola-Kirchhoff can be derived as

$$\boldsymbol{P} = \frac{\partial W}{\partial \boldsymbol{F}},$$
$$\boldsymbol{S} = 2\frac{\partial W}{\partial \boldsymbol{C}} = \frac{\partial W}{\partial \boldsymbol{E}}.$$

When dealing with a compressible or nearly incompressible material, the best way to handle the different behaviour of materials in bulk and shear is to decompose the strain energy function in its isochoric (volume-preserving) and volumetric (volume-changing) components

$$W = W_{iso}\left(\overline{\boldsymbol{C}}\right) + W_{vol}\left(J\right),$$

where the volumetric contribution is a function only of $J = \det\left(\boldsymbol{F}\right)$ as it represents the volume ratio between current and initial configuration (see Section 2.2.1), and the isochoric component is defined in terms of the modified right Cauchy-Green, $\overline{\boldsymbol{C}}$, defined as

$$\overline{\boldsymbol{C}} = J^{-2/3}\boldsymbol{C},$$

whose relative invariants are

$$I_1\left(\overline{\boldsymbol{C}}\right) = \mathrm{tr}\left(\overline{\boldsymbol{C}}\right),$$
$$I_2\left(\overline{\boldsymbol{C}}\right) = \left[\mathrm{tr}^2\left(\overline{\boldsymbol{C}}\right) - \mathrm{tr}\left(\overline{\boldsymbol{C}}^2\right)\right],$$
$$I_3\left(\overline{\boldsymbol{C}}\right) = \det\left(\overline{\boldsymbol{C}}\right).$$

The strain energy density for *a compressible* Neo-Hookean material is defined as

$$W = \frac{\mu}{2}\left(\bar{I}_1 - 3\right) + \frac{\kappa}{2}\left(J-1\right)^2,$$

where μ is the shear modulus or Lamé second parameter and κ is the bulk modulus. These two parameters can be expressed in terms of the Young

modulus, E, and the Poisson's ratio, ν_p, as

$$\mu = \frac{E}{2\left(1+\nu_p\right)},$$
$$\kappa = \frac{E}{3\left(1-2\nu_p\right)}.$$

The 1st and 2nd Piola-Kirchhoff stress tensors can be derived from the strain energy function as follow [91]:

$$\begin{aligned} \boldsymbol{P}\left(\boldsymbol{F}\right) = \frac{\partial W}{\partial \boldsymbol{F}} = 2\boldsymbol{F}\frac{\partial W}{\partial \boldsymbol{C}} = \; & \frac{\mu}{2}J^{-2/3}\left(\boldsymbol{F} - \frac{1}{3}\mathrm{tr}\left(\boldsymbol{F}\cdot\boldsymbol{F}^T\right)\boldsymbol{F}^{-T}\right) \\ & + \frac{\kappa}{2}\left(J-1\right)J\boldsymbol{F}^{-T}, \\ \boldsymbol{S}\left(\boldsymbol{C}\right) = 2\frac{\partial W}{\partial \boldsymbol{C}} = \; & \frac{\mu}{2}J^{-2/3}\left(\boldsymbol{I} - \frac{1}{3}\mathrm{tr}\left(\boldsymbol{C}\right)\boldsymbol{C}^{-1}\right) \\ & + \frac{\kappa}{2}\left(J-1\right)J\boldsymbol{C}^{-1}. \end{aligned} \tag{2.13}$$

In OpenFOAM the structural momentum equation is solved in an updated Lagrangian formulation. In order to plug the Neo-Hookean constitutive law in the linear momentum equation solved by OpenFOAM (eqn. 2.8) the 2nd Piola-Kirchhoff stress tensor needs to be expressed in its incremental form. This can be done by means of the finite difference technique. This derivation has been an original work of this thesis and can be found in the Appendix A. We report here the final result

$$\begin{aligned} \delta\boldsymbol{S} \; = \; & \frac{\mu}{6}\left(\nabla\delta\boldsymbol{u} + \left(\nabla\delta\boldsymbol{u}\right)^T + \left(\nabla\delta\boldsymbol{u}\right)^T\cdot\nabla\delta\boldsymbol{u}\right) \\ & + \left[\left(\frac{\kappa}{2} - \frac{10\mu}{18}\right)\mathrm{tr}\left(\nabla\delta\boldsymbol{u}\right) - \frac{\mu}{6}\mathrm{tr}\left(\left(\nabla\delta\boldsymbol{u}\right)^T\cdot\nabla\delta\boldsymbol{u}\right)\right]\boldsymbol{I}. \end{aligned}$$

2.3 Electrostatics

Electroactive polymers are here modelled as compliant capacitors. Generally a charged capacitor made of parallel plates have a uniform electric field between them. This is true within the main body of the plates. How-

ever since the electric charges tend to accumulate to the sharp edges of the plates here the uniformity is disrupted due to *edge effects*. For the purpose of this thesis these effects of the electric field are neglected, as the area of the electrodes is much bigger than the thickness of the dielectric [147]. Also, the electrodes are assumed to remain parallel during deformation and the dielectric is assumed to have a constant value of the relative dielectric permittivity, ε_R.

By definition the electric field in a point in space is equal to the negative gradient of the scalar field voltage, ϕ (electric potential) in that point[52]

$$\mathbf{E} = -\nabla\phi.$$

The measure of the electric flux through a closed surface can be calculated with the Gauss law

$$\nabla \cdot \mathbf{E} = \frac{\rho_c}{\varepsilon_0 \varepsilon_R},$$

where ρ_c is the charge density and ε_0 is the electric permittivity of vacuum. Since the charge is conserved, the relative continuity equation must be satisfied

$$\frac{\partial \rho_c}{\partial t} + \nabla \cdot \boldsymbol{J} = 0.$$

Here $\boldsymbol{J}$ is the current density, i.e. the electric current per unit area. The current density is commonly approximated by the electrical conductivity, k, times the electric field:

$$\boldsymbol{J} = k\mathbf{E}.$$

According to the Lorentz force law, the presence of the electric field generates a force between the two electrodes which eventually induces a state of stress in the dielectric, known as Maxwell stress tensor. Neglecting the magnetic contribution, the Maxwell stress tensor is given by

$$\boldsymbol{\sigma}_m = \varepsilon_0 \varepsilon_R \left(\mathbf{E} \otimes \mathbf{E} - \frac{1}{2} (\mathbf{E} \cdot \mathbf{E}) \cdot \boldsymbol{I} \right). \tag{2.14}$$

This expression is general and it does not require any assumption on the behavior of the material. Therefore it can be used for every dielectric with

isotropic electric properties and the total stress tensor, σ_{tot}, will be given by the sum of the elastic, σ_e, and the Maxwell, σ_m, stress tensors as they can be considered completely decoupled [122]:

$$\sigma_{tot} = \sigma_e + \sigma_m.$$

Furthermore, the evolution of the electrostatic forces is assumed to be instantaneous since its time scale is several orders of magnitude faster than the mechanical one.

2.4 PID control theory

PID (Proportional-Integral-Derivative) control is the most common control algorithm used in industry because of its robustness and functional simplicity. The purpose of a PID controller is to feed a process with an actuator input in order to have control of an output variable [72]. In a typical control system, a sensor is used to read the process output (y) that is going to be controlled. Then an error, $e(t)$, is calculated as the difference between the actual output and the desired one, usually referred as *set point* (y_{sp}),

$$e(t) = y - y_{sp}.$$

The PID controller is in charge to compute the actuator input, $u(t)$, as a function of the error, with the purpose of eventually driving the error to zero. Reading the sensor, evaluating the error and feed a control input to the system is done continuously during the process, therefore this is known as *closed-loop* control [135]. As the name suggests the actuator input, $u(t)$, can be split into 3 contributions which are independent from each other: a term proportional to the instantaneous error, $e(t)$, a term which takes into account the history of the error (integral term) and a term which is proportional to the rate of change of the error (derivative term),

$$u(t) = \mu_p e(t) + \mu_i \int_0^t e(\tau) d\tau + \mu_d \frac{de(t)}{dt}.$$

The weight of these three terms is given by multiplying each of them by a constant (*gain*). How these constants are tuned depends on the case and it is ultimately the objective of designing an efficient control law for a specific process.

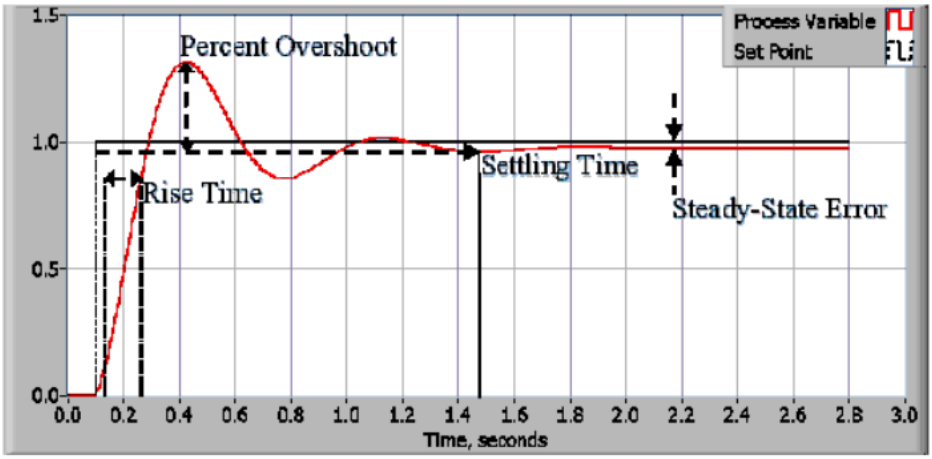

Figure 2.2: Response of a typical PID closed loop system [17].

In a standard process the control system performance is usually evaluated by applying a step function on the set point and measuring the output variable. With reference to Fig. 2.2, the following quantities are defined:

rise time is the time the system takes to go from 10% to 90% of the steady-state value,

percent overshoot is how much the output variable overshoot the final value, expressed as percentage of the final value,

settling time is the time required for the output variable to have an error less than 5%,

steady-state error is the final difference between the output variable and the set point.

Generally the proportional, integral and derivative term affect these parameters differently. In a P-only control, increasing the proportional gain, μ_p, has the effect of reducing the rise time and the steady-state error but

in some cases also increasing the percent overshoot. However if the proportional gain is too high the ouput variable will start oscillating and the system can eventually become unstable. As the integral component sums over time, even a small error will cause the integral component to raise slowly and therefore drive the steady-state error to zero. At the same time the integral term increases the overshoot, however in some occasions some amount of overshoot might be useful for a fast system so that it could respond to changes immediatly. Adding a derivative term will cause the control system to react more strongly to error variations and will increase the overall speed of the control system. However as the derivative response is highly sensitive to noise it might make the control system unstable.

The process of finding the optimal values of the gains for μ_p, μ_i and μ_d to get an ideal response from the control system is called tuning. For simple systems the most common methods are the empirical "guess and check" method and the semi-empirical Ziegler-Nichols method [152]. In both methods μ_i and μ_d are set to zero first and the proportional gain is increased until the output of the loop oscillates. Once oscillations start, μ_i, μ_d are then adjusted empirically in the first method to stop the oscillations, achieve a minimal steady state error and to reduce overshoot. In the Ziegler-Nichols method μ_i, μ_d are functions of the critical proportional gain μ_c and the relative period of oscillations. The unsteady nature of the Fluid-Structure coupling of the membrane at high angles of attack makes these methods not really applicable as the system is already oscillating without control, therefore the initial choice of the gains has been made in a heuristic way.

Chapter 3

Numerical Methods

Since the Navier-Stokes equations will be solved numerically, an appropriate method of discretization needs to be chosen. Generally there are three different methods: the finite difference, finite element and finite volume method. Another important aspect, concerning a Computational Fluid Dynamics (CFD) simulation, is how the computational domain is divided into a finite amount of control volumes (the numerical grid). Generally grids can be divided into two families: structured and unstructured. When using structured grids, the cell ordering is fairly straight-forward such that the flow solver uses this fact to solve the system in a more efficient way. Unfortunately, structured grids become more difficult to generate when the geometry to discretize is complex (common in engineering problems). This can be more easily done with unstructured grids, although their algorithmic cost becomes higher.

3.1 Properties of numerical solution methods

A numerical solution is obtained as result of the discrete description of the solution domain and the governing equations. Its accuracy is determined by the relation between the exact and numerical solution. Since in most of the applications of interest the exact solution is not available, it is useful to know what kind of errors affect a numerical solution. Generally they are

divided in three main groups [78]:

Modelling errors are defined as the difference between the actual flow and the exact solution from the partial differential equations chosen to describe the flow. In case of a laminar flow the Navier-Stokes equations represent with good accuracy the flow behaviour. However for turbulent flows the additional models might not always describe the underlying physical process with good accuracy.

Discretization errors are defined as the difference between the exact solution of the linear system of algebraic equations obtained by discretising the governing equations on a discretized solution domain and the exact solution of the partial differential equations, the latter being usually unknown. These errors depend on the accuracy of the method used to discretize the governing equations as well as the discretization of the solution domain. The difference between the discretised and the exact solution represents the *truncation error*. For a numerical solution to be consistent the solution of the discretised system of equations should tend to the exact solution of the governing partial differential equations as the mesh spacing and the time step tend to zero. Commonly this is proved with an empirical approach where the same computation is repeated on subsequently refined meshes until the solution converges to a grid-independent solution.

Iterative convergence errors represent the difference (also referred to as residuals) between the approximate solution calculated using iterative methods and the exact solution of the linear system of algebraic equations. For the numerical process to be stable these errors should not be amplified when performing the iterations.

Moreover, since the Navier-Stokes equations express the conservation of mass, momentum and energy also the discretized equations should guar-

antee conservation. In a finite volume formulation the governing equations are written in their conservative form and this property is intrinsically respected by the discretised equations. This is one of the advantages of the finite volume approach since the conservation is guaranteed for every small Control Volume (CV) and, therefore, for the whole computational domain.

3.2 Finite Volume Method

As the FV is the method used in OpenFOAM, an explanation of its strategy applied to the discretization of a general transport equation will be quickly reviewed here for clarity. In general a transport equation in conservative form[1] for a generic variable ϕ inside a control volume V can be written as

$$\int_{V_P} \underbrace{\frac{\partial \rho \phi}{\partial t} dV}_{\text{temporal derivative}} + \int_{V_P} \underbrace{\nabla \cdot (\rho \boldsymbol{U} \phi)\, dV}_{\text{convective term}} + \\ - \int_{V_P} \underbrace{\nabla \cdot \left(\rho \Gamma_\phi \nabla \phi\right) dV}_{\text{diffusion term}} = \int_{V_P} \underbrace{S_\phi\left(\phi\right) dV}_{\text{source term}}, \tag{3.1}$$

where ρ is the density, $\boldsymbol{U}$ the velocity and Γ_ϕ is a generic diffusivity constant. This equation needs to be solved in a given domain, with given boundary conditions and initial conditions. For good accuracy, it is necessary for the order of the discretisation to be equal to or higher than the order of the equation that is being discretised [65]. As consequence of this requirement, all dependent variables are assumed to vary linearly around

[1] conservative and nonconservative are equivalent forms of the conservation equations, which differ by the use of the partial or total derivative ($\frac{d\phi}{dt} = \frac{\partial \phi}{\partial t} + \boldsymbol{U} \cdot \boldsymbol{\nabla}\left(\phi\right)$). The conservative form (Eulerian formulation) states the conservation laws through a control volume fixed in space and the convective term is calculated as $\boldsymbol{\nabla}\left(\boldsymbol{U}\phi\right)$; the nonconservative form (Lagrangian formulation) enforces the conservation laws in a control volume as it moves with the fluid and the convective term has the form $\boldsymbol{U} \cdot \boldsymbol{\nabla}\left(\phi\right)$[137].

a point P in space and instant t in time

$$\begin{aligned} \phi(\boldsymbol{x}) &= \phi_P + (\boldsymbol{x} - \boldsymbol{x}_P) \cdot (\nabla\phi)_P \\ \phi(t + \delta t) &= \phi^t + \delta t \left(\frac{\partial\phi}{\partial t}\right)^t, \end{aligned}$$

where $\phi_P = \phi(\boldsymbol{x}_P)$ and $\phi^t = \phi(t)$.

The whole computational domain is divided into arbitrary control volumes as represented in Fig. 3.1. The control volume V_P has a volume V and is constructed around its centroid, P. $\boldsymbol{d}$ is the vector from the centroid P to the centroid of the neighbour cell, N. $\boldsymbol{S}_f$ is the face area vector of the face f, pointing outwards. It is located at the face centroid, is normal to the face and has a magnitude equal to the area of the face. In the FV method we assume that the values of all variables are computed and stored in the centroid P, this is known as *collocated grid arrangement* [137].

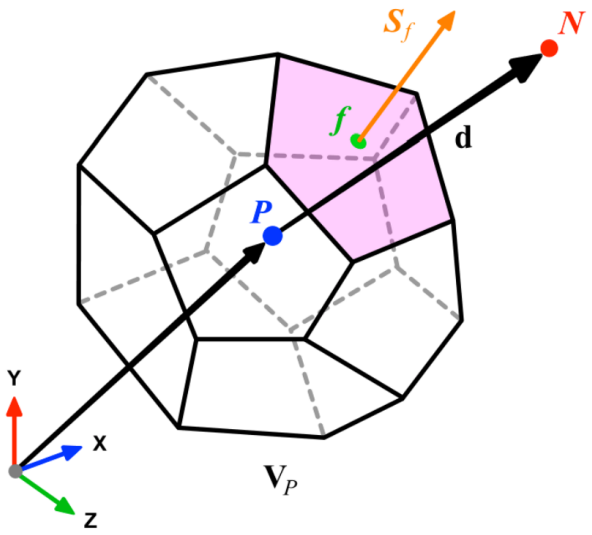

Figure 3.1: Control Volume (from Jasak [65])

The application of Gauss' theorem for the FV method is particularly convenient in dealing with volume integrals of the divergence of a given vector, as they represent the flux of that vector through the surrounding

surface of the volume. Gauss' theorem states

$$\int_{V_P} \nabla \cdot \boldsymbol{a} dV = \oint_{\partial V_P} d\boldsymbol{S} \cdot \boldsymbol{a},$$

where ∂V_p is a closed surface bounding the control volume V_P and $d\boldsymbol{S} = \boldsymbol{n}dS$ represents the infinitesimal area vector pointing outward of the surface ∂V_P. Thus, using Gauss' theorem to convert volume integrals into surface integrals and assuming that the control volumes do not change in time, equation 3.1 can be written as

$$\frac{\partial}{\partial t}\int_{V_P} (\rho\phi)\, dV + \oint_{\partial V_P} \underbrace{d\boldsymbol{S} \cdot (\rho \boldsymbol{U}\phi)}_{\text{convective flux}} - \oint_{\partial V_P} \underbrace{d\boldsymbol{S} \cdot \left(\rho\Gamma_\phi \nabla\phi\right)}_{\text{diffusive flux}} = \int_{V_P} S_\phi\,(\phi)\, dV. \tag{3.2}$$

The surface integrals can be easily discretized as follows

Convective term

$$\begin{aligned} \oint_{\partial V_P} \underbrace{d\boldsymbol{S} \cdot (\rho \boldsymbol{U}\phi)}_{\text{convective flux}} &= \sum_f \int_f d\boldsymbol{S} \cdot (\rho\phi \boldsymbol{U}) \\ &\approx \sum_f \boldsymbol{S}_f \cdot \left(\overline{\rho\phi \boldsymbol{U}}\right)_f = \sum_f \boldsymbol{S}_f \cdot (\rho \boldsymbol{U}\phi)_f . \end{aligned}$$

Diffusive (Laplacian) term

$$\begin{aligned} \oint_{\partial V_P} \underbrace{d\boldsymbol{S} \cdot \left(\rho\Gamma_\phi \nabla\phi\right)}_{\text{diffusive flux}} &= \sum_f \int d\boldsymbol{S} \cdot \left(\rho\Gamma_f \nabla\phi\right)_f \\ &\approx \sum_f \boldsymbol{S}_f \cdot \left(\overline{\rho\Gamma_f \nabla\phi}\right)_f = \sum_f \boldsymbol{S}_f \cdot \left(\rho\Gamma_f \nabla\phi\right)_f . \end{aligned} \tag{3.3}$$

In the convective and diffusive terms the integrands have been approximated using the values at the midpoint of the faces. This corresponds to numerical integration by means of the midpoint method, which is second-order accurate (with respect to the face length) [106].

Source term

$$\int_{V_P} S_\phi(\phi)\, dV = \left(S_c + S_p \phi_P\right) V_P.$$

All the terms that can not be written as convection, diffusion or temporal terms are treated as sources. The source term, $S_\phi(\phi)$ is a general function of ϕ and it has been linearized. Therefore its approximation is exact if S_ϕ is either constant or varies linearly within the CV; otherwise it is second order accurate [30]. Here S_c is the constant part of the source term and S_p is the non-linear part.

Gradient term

$$(\nabla\phi)_P = \frac{1}{V_P} \sum_f \left(\boldsymbol{S}_f \phi_f\right).$$

Here the centroid gradient has been approximated using Gauss' theorem. This method is second-order accurate as it is equivalent to a central differencing scheme.

Since all the variables are computed and stored at the centroid of the control volumes, the values at the faces have to be evaluated by some sort of interpolation for both sides of face f. The face values appearing in the *convective* flux can be computed as follows:

Linear interpolation (Fig. 3.2a)

$$\begin{aligned} \phi_f &= f_x \phi_P + (1 - f_x)\, \phi_N \\ \text{with} \qquad f_x &= \frac{fN}{PN} = \frac{\left|\boldsymbol{x}_f - \boldsymbol{x}_N\right|}{|\boldsymbol{d}|}. \end{aligned}$$

This method is equivalent to a central differencing scheme and it is second-order accurate, but it might generate oscillatory solutions (unbounded solutions).

Upwind differencing (Fig. 3.2b)

$$\phi_f = \begin{cases} \phi_f = \phi_P & \text{for } \overset{\circ}{F} \geq 0, \\ \phi_f = \phi_N & \text{for } \overset{\circ}{F} < 0. \end{cases}$$

where $\overset{\circ}{F}$ is the mass flux through the face, $\overset{\circ}{F} = \boldsymbol{S} \cdot (\rho \boldsymbol{U})_f$ and therefore the value for an internal face is the same of the cell upstream. This type of interpolation does not generate oscillatory solutions (bounded), but is first order accurate and adds numerical diffusion to the solution.

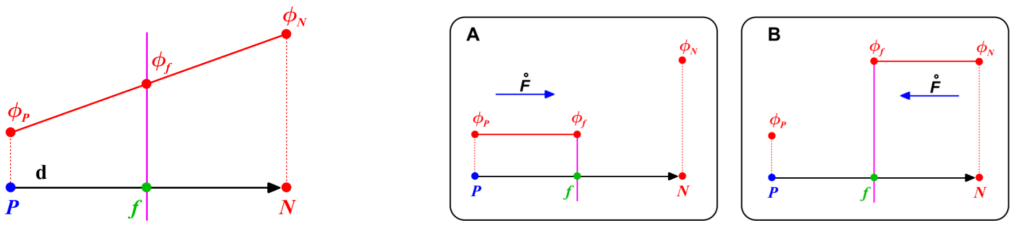

(a) Linear interpolation. (b) Upwind differencing.

Figure 3.2: Face interpolation [65].

For the *diffusive* flux the quality of the mesh can induce errors in calculating the gradient at the face. In particular *non-orthogonality* and *skewness* are significant contributors to error. Referring to Figs. 3.3a and 3.3b, non-orthogonality measures the misalignment between the face normal vector, $\boldsymbol{S}$, and the vector connecting adjacent cell centers, $\boldsymbol{d}$, while skewness, Δ_i (Figs. 3.3c and 3.3d), measures the distance between the location of the face center, f, and the vector connecting adjacent cell centers, $\boldsymbol{d}$.

For meshes of different quality the diffusive flux can be calculated as follows:

Orthogonal mesh (Fig. 3.3a)

$$\boldsymbol{S} \cdot (\nabla \phi)_f = |\boldsymbol{S}| \frac{\phi_N - \phi_P}{|\boldsymbol{d}|}.$$

This is a central difference approximation of the first order derivative and is second order accurate,

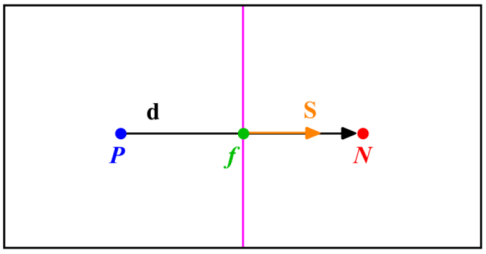

(a) Orthogonal and non-skewed mesh.

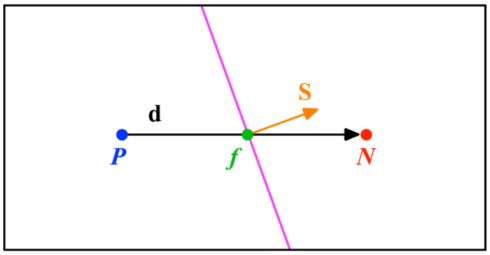

(b) Non-orthogonal and non-skewed mesh.

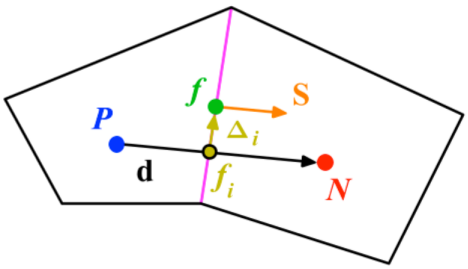

(c) Orthogonal and skewed mesh.

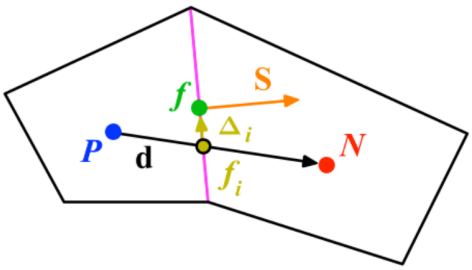

(d) Non-orthogonal and skewed mesh.

Figure 3.3: Mesh non-orthogonality and skewness [65].

Non-orthogonal mesh (Fig. 3.4)

$$\boldsymbol{S} \cdot (\nabla \phi)_f = |\Delta_\perp| \underbrace{\frac{\phi_N - \phi_P}{|\boldsymbol{d}|}}_{\text{orthogonal contribution}} + \underbrace{\boldsymbol{k} \cdot (\nabla \phi)_f}_{\text{non-orthogonal contribution}} .$$

The orthogonal part of the face vector, $\Delta_\perp$, can be calculated with a minimum correction approach ($\Delta_\perp = \frac{\boldsymbol{d}\cdot\boldsymbol{S}}{\boldsymbol{d}\cdot\boldsymbol{d}}\boldsymbol{d}$, Fig. 3.4a) or with an over-relaxed approach ($\Delta_\perp = \frac{\boldsymbol{d}}{\boldsymbol{d}\cdot\boldsymbol{S}}|\boldsymbol{S}|^2$, Fig. 3.4b), and the non-orthogonal contribution is evaluated by using linear interpolation from the gradient of the control volumes centroid, computed using the Gauss theorem.

Skewed mesh (Fig. 3.3c and 3.3d) in order to maintain second-order accuracy and avoid unboundedness a correction must be introduced.

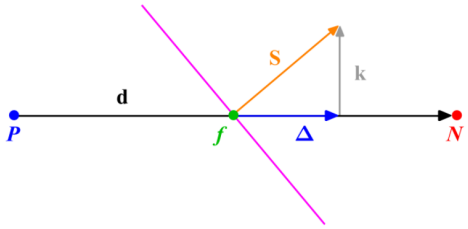

(a) Minimum correction approach.

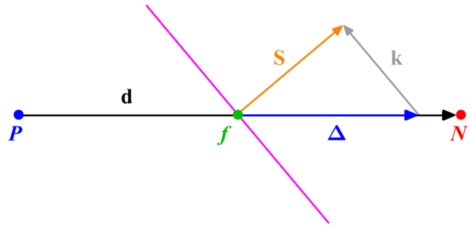

(b) Over-relaxed approach.

Figure 3.4: Non-orthogonal contribution [65].

The gradient can be evaluated as

$$(\nabla\phi)_P = \frac{1}{V_P}\sum_f \boldsymbol{S}_f\phi_f = \frac{1}{V_P}\sum_f \boldsymbol{S}_f\left[\phi_{f_i} + \Delta_i \cdot (\nabla\phi)_{f_i}\right],$$

where f_i refers to the intersection between the vector $\boldsymbol{d}$ and the face f, which for a skewed mesh does not correspond to the face center.

In OpenFOAM the method of lines (MOL) is used for solving the governing equations. The MOL is a solving technique of a partial differential equation (PDE) where the first step is to replace the spatial derivatives with algebraic approximations. Once this is done, the spatial derivatives are no longer stated explicitly in terms of the spatial independent variables. Thus, effectively only the time derivative remains and the starting equation can be solved as an ordinary differential equation (ODE). In other words we have a system of ODEs which approximates the original PDE [107]. Using the technique of the MOL, the temporal discretization is made after the spatial discretization. The main advantage of the MOL technique is that different numerical approximations can be selected for the spatial

and temporal terms. Each term can be treated differently to yield different accuracies. At this stage any temporal discretization scheme can be used, e.g. Crank-Nicolson, Euler implicit, forward Euler, backward differencing.

3.2.1 Solution of the structural momentum equation

The finite volume discretization procedure explained above is general and in this work has been applied to the structural momentum equation as well. In absence of body forces the discretized form of the linear momentum equation in an Updated Lagrangian formulation (Eqn. 2.8) can be written using the Gauss' theorem as

$$\rho_{Pu} V_{Pu} \frac{\partial \delta \boldsymbol{v}}{\partial t} = \sum_f \boldsymbol{n}_{fu} S_{fu} \cdot \left(\delta \boldsymbol{S} + \boldsymbol{S} \cdot \delta \boldsymbol{F}^T + \delta \boldsymbol{S} \cdot \delta \boldsymbol{F}^T \right)_f , \tag{3.4}$$

where the subscript u indicates that the value are calculated for the updated configuration and the subscripts P and f represent the cell and the face value. $\boldsymbol{n}_{fu} S_{fu}$ is the face area vector, $\boldsymbol{S}$ and $\delta \boldsymbol{S}$ are the total and increcemntal 2nd Piola-Kirchhoff stress tensor respectively and $\delta \boldsymbol{F}$ is the incremental deformation tensor. The face values of all dependent variables are calculated by linear interpolation of the neighbouring cell values. The total and incremental 2nd Piola-Kirchhoff stress tensors, $\boldsymbol{S}$ and $\delta \boldsymbol{S}$, and the incremental deformation tensor, $\delta \boldsymbol{F}$ are functions of the gradient of the incremental displacement, $\nabla \delta \boldsymbol{u}$ (see Section 2.2.2). Therefore equation 3.4 is solved iteratively for $\delta \boldsymbol{u}$ updating $\nabla \delta \boldsymbol{u}$ at the end of every iteration until the solution changes less than some pre-defined tolerance. This is done for every time step of the transient simulation [132].

At the end of each time step, the total displacement vector and the total 2nd Piola- Kirchhoff stress tensor are updated as follows:

$$\begin{aligned} \boldsymbol{u}^n &= \boldsymbol{u}^o + \delta \boldsymbol{u}^n, \\ \boldsymbol{S}^n &= \boldsymbol{S}^o + \delta \boldsymbol{S}^n, \end{aligned}$$

where the superscripts n and o refer to the new and old time step respec-

tively. The 2nd Piola-Kirchhoff stress tensor increment $\delta \boldsymbol{S}^n$ is calculated using the newly calculated displacement vector increment $\delta \boldsymbol{u}^n$. When the mesh is moved at the beginning of the new time step by using the displacement increment from the previous time step, the 2nd Piola-Kirchhoff stress tensor related to the old updated configuration must be transformed to the new updated configuration as it effectively represents the Cauchy stress tensor:

$$\boldsymbol{S}^o = \boldsymbol{\sigma} = \frac{1}{J}\boldsymbol{F} \cdot \boldsymbol{S} \cdot \boldsymbol{F}^T = \frac{1}{\det \boldsymbol{F}^o}\boldsymbol{F}^o \cdot \boldsymbol{S}^o \cdot \boldsymbol{F}^{oT}.$$

3.2.2 SIMPLE, PISO and PIMPLE algorithms

A further note should be made on the solution strategy adopted by OpenFOAM to solve the incompressible Navier-Stokes equations. Two issues require special attention: non-linearity of the momentum equation and the pressure-velocity coupling.

The non-linear term in the momentum equation is $\nabla \cdot (\boldsymbol{U} \otimes \boldsymbol{U})$, i.e. the "trasport of velocity by itself". The discretized for of this expression would be quadratic in velocity and the resulting system of algebraic equations would be non-linear. OpenFOAM takes care of this problem linearising the convection term

$$\begin{aligned} \nabla \cdot (\boldsymbol{U} \otimes \boldsymbol{U}) &= \sum_f \boldsymbol{S} \cdot (\boldsymbol{U})_f (\boldsymbol{U})_f = \sum_f \overset{\circ}{F} (\boldsymbol{U})_f \\ &= a_p \boldsymbol{U}_p + \sum_N a_N \boldsymbol{U}_N \end{aligned}$$

where $\overset{\circ}{F}$ is the mass flux through the face f, and a_p , a_N are coefficients function of $\boldsymbol{U}$ respectively at the centroid P and at the neighbours centroids N and represent the diagonal and off-diagonal terms of the sparse system of equations, respectively. Linearization of the convection term implies that an existing flux field that satisfies the continuity equation will be used to calculate a_p and a_n [65].

In a steady-state calculation the linearization does not affect the final

result because the fact that the non-linear term has been lagged is not significant. However in transient flows since the flux needs to be updated at each time step a different approach can be adopted: either introduce subiterations for each time step to update the fluxes or neglect the lagged non-linearity effects. If the time step is sufficiently small the change between consecutive solutions will also be small and it is therefore possible to lag the non-linearity effect without any significant effect. However, if the time step is large it is necessary to iterate over the non-linear term. Iterations can significantly increase the computational time but the advantage is that the non-linear system is fully resolved for every time step whose size limitation comes only from the temporal accuracy requirements.

For transient simulations the pressure implicit with splitting of operator (PISO) algorithm [62] is used for the pressure-velocity coupling whereas for steady-state calculations the semi-implicit method for pressure-linked equations (SIMPLE) [30] is adopted. In both methods a semi-discretised form of the momentum equation calculated at the each centroid P is used

$$a_P \boldsymbol{U}_P = \boldsymbol{H}(\boldsymbol{U}) - \nabla p. \tag{3.5}$$

Equation 3.5 is obtained from the integral form of the momentum equation using the discretization procedure described previously. At this stage the pressure has not been discretized yet. The $\boldsymbol{H}(\boldsymbol{U})$ term consists of the "transport part" including the matrix coefficients for all neighbours multiplied by corresponding velocities and the "source part" including the souce part of the transient term and all other sources terms apart from the pressure gradient:

$$\boldsymbol{H}(\boldsymbol{U}) = -\sum_N a_N \boldsymbol{U}_N + \frac{\boldsymbol{U}^o}{\Delta t}.$$

Here $\boldsymbol{U}$ is the velocity at time $t + \Delta t$ whereas $\boldsymbol{U}^o$ is the velocity at the time t. The discretized form of the continuity equation reads

$$\nabla \cdot \boldsymbol{U} = \sum_f \boldsymbol{S} \cdot \boldsymbol{U}_f = 0. \tag{3.6}$$

Velocities on the cell face are expressed as the face interpolate of equation 3.5

$$\boldsymbol{U}_f = \left(\frac{\boldsymbol{H}(\boldsymbol{U})}{a_P}\right)_f - \left(\frac{1}{a_P}\right)_f (\nabla p)_f . \tag{3.7}$$

Substituting equation 3.7 into equation 3.6 the following form of the pressure equation is obtained

$$\nabla \cdot \left(\frac{1}{a_P}\nabla p\right) = \nabla \cdot \left(\frac{\boldsymbol{H}(\boldsymbol{U})}{a_P}\right) = \sum_f \boldsymbol{S} \cdot \left(\frac{\boldsymbol{H}(\boldsymbol{U})}{a_P}\right)_f \tag{3.8}$$

where the Laplacian of the pressure on the left hand side is discretised as previously described in equation 3.3.

The final form of the discretised incompressible Navier-Stokes equations is

$$\text{conservation of momentum} \quad a_P \boldsymbol{U}_P = \boldsymbol{H}(\boldsymbol{U}) - \sum_f \boldsymbol{S}(p)_f ,$$

$$\text{continuity} \quad \sum_f \boldsymbol{S} \cdot \left[\left(\frac{1}{a_p}\right)_f (\nabla p)_f\right] = \sum_f \boldsymbol{S} \cdot \left(\frac{\boldsymbol{H}(\boldsymbol{U})}{a_P}\right)_f .$$

The face flux $\overset{\circ}{F}$ is calculated using equation 3.7

$$\overset{\circ}{F} = \boldsymbol{S} \cdot \boldsymbol{U}_f = \boldsymbol{S} \cdot \left[\left(\frac{\boldsymbol{H}(\boldsymbol{U})}{a_P}\right)_f - \left(\frac{1}{a_P}\right)_f (\nabla p)_f\right] . \tag{3.9}$$

When equation 3.8 is satisfied, the face fluxes are guaranteed to be conservative.

Starting from the discretised Navier-Stokes equations the PISO algorithm can be described with the following steps:

moment predictor: the momentum equation is solved using the pressure field from the previous time step, giving an approximation of the new velocity field.

pressure solution: using the predicted velocities, the $\boldsymbol{H}(\boldsymbol{U})$ operator is as-

sembled and the pressure equation (continuity) gives the first estimation of the new pressure field.

explicit velocity correction: in order to have a set of conservative fluxes (eqn. 3.9) consistent with the pressure field, the velocity field needs to be corrected. This is done explicitly using the momentum equation.

So far during the velocity correction only the new pressure gradient has been updated in the momentum equation. However also the term $\boldsymbol{H}(\boldsymbol{U})$ which appears in the momentum equation needs to be corrected in order to reflect the new velocity field. Therefore a loop of pressure solutions with the new value of $\boldsymbol{H}(\boldsymbol{U})$ and the correspondent velocity corrections are performed until a pre-determined tolerance is reached before proceding to the new time step.

In the case of a steady-state problem solved iteratively the changes between consecutive solutions might not be as small as the ones between small consecutive time steps of a transient problem. Therefore the SIMPLE algorithm uses under-relaxation to avoid numerical instabilities. In particular, the steps of the SIMPLE algorithm are:

- The under-relaxed momentum equation is solved using the velocity under-relaxation factor α_U and the pressure field from the previous iteration.
- The pressure equation is solved in order to obtain the new pressure distribution, p^p.
- A new set of conservative fluxes is calculated using equation 3.7. In the SIMPLE scheme rather than solving again the momentum equation like in the PISO algorithm, the velocity part of the error is taken into account relaxing the pressure solution with

$$p^{new} = p^{old} + \alpha_p \left(p^p - p^{old} \right)$$

where

- p^{new} is the approximation of the pressure field that will be used in the next momentum predictor,
- p^{old} is the pressure field used in the momentum predictor,
- p^{p} is the solution of the pressure equation,
- α_p is the pressure under-relaxation factor ($0 < \alpha_p \leq 1$).

Generally the SIMPLE algorithm is developed to reach the steady-state conditions very quickly but does not contain the time derivative and therefore no time information. On the contrary the PISO scheme which is designed for transient simulations relies on a small time step to be stable. The Courant-Friedrichs-Lewy (CFL) number, defined as $CFL = \frac{\Delta t}{\Delta x} U$, needs to be smaller than unity in the PISO algorithm in order to avoid the pressure-velocity coupling errors to be amplified. This means that it is very expensive to solve a complex problem for a long physical time. For this reason a merged PISO - SIMPLE algorithm (PIMPLE) has been developed to take advantage from both schemes and avoid the limitations on the CFL [56]. In fact, using under-relaxation for each time step would allow to use a larger CFL ($CFL \gg 1$). The CFL number can be seen as the ratio between the velocity of the partial differential equation, U and the velocity at which the information travels across the mesh, $\frac{\Delta x}{\Delta t}$. Therefore a $CFL < 1$ guarantees not only the stability of an explicit numerical scheme [137] but also the accuracy of a transient simulation in such a way that at each time step the information about the flow velocity has traveled less than a mesh size length. However the CFL is a field variable and for a fixed time step it depends on the local value of the fluid velocity and the mesh size. Therefore it might happen that once the time step has been accurately chosen to have a good time resolution of the physics, the CFL could have a local value larger than unity in small areas such as the leading edge where the flow accelerates and the mesh size is smaller than in the rest of the grid. Here local values of $CFL > 1$ can cause a PISO scheme to diverge even if the time step is already small enough to sample accurately the relevant frequencies of the system. On the contrary the PIMPLE algorithm can handle localized peaks of $CFL > 1$ much more safely because of the additional outer

corrections. For each outer correction the pressure and velocity fields are under-relaxed and the inner correctors of the PISO scheme are performed. In order to increase the stability more corrector steps (outer and inner) are needed requiring more computational time per time step. However the computational gain is still very large when compared with decreasing the time step and use the PISO algorithm.

For this reason the PIMPLE algorithm has been included as original work of this thesis in the FSI solver and the code is reported in Appendix B. In particular, with the PIMPLE algorithm the FSI solver could handle local $CFL \approx 5$ without losing resolution of the most relevant time scales using generally 3 outer corrections and 2 inner corrections.

3.2.3 Boundary conditions

In order to obtain a single solution of the discretised governing equations, boundary conditions must be specified at the boundaries of the computational domain. The boundary conditions, which are used to close the system are:

zero-gradient: the normal gradient of the solution is zero at the boundary. This condition is known as a Neumann-type condition, $\partial\phi/\partial n = 0$,

fixed-value: the value of the solution is specified at the boundary. This is a Dirichlet-type condition, $\phi = b$,

symmetry: treats the conserved variables as if the boundary was a mirror plane. This condition defines that the component of the solution gradient normal to this plane should be fixed to zero. The parallel components are extrapolated from the interior cells,

moving-wall-velocity: it is used on a moving boundary in order to have zero flux, using the Arbitrary Lagrangian Eulerian (ALE) approach as explained in Section 3.2.4.

For external flow simulations, such as those of membrane wings, a distinction has to be made between the outer and the inner boundaries. The latter correspond to the deforming membrane. In case of forward flight, two domain boundaries are defined as inlet and outlet, respectively. At the inlet boundary the velocity is defined as fixed-value and the pressure as zero-gradient. On the other hand, at the outlet boundary, the pressure has to be fixed-value and the velocity zero-gradient [144]. On a stationary wall the no-slip condition needs to be guaranteed, therefore a fixed-value ($\boldsymbol{U} = 0$) is specified for the velocity in combination with a zero-gradient for the pressure. If the boundary of the wall moves, then the proper boundary condition is the moving-wall-velocity which introduces an extra velocity in order to maintain the no-slip condition and ensures a zero flux through the moving boundary.

3.2.4 Arbitrary Lagrangian-Eulerian formulation

The governing equations of the fluid dynamics are generally discretised using the Eulerian description, where the fluid moves through a fixed control volume (i.e. fixed grid). On the contrary, in the Lagrangian formulation the grid is attached to the fluid (or the solid) and follows its movement and deformation. In fluid dynamics when the domain moves or deforms in time due to a moving boundary, a fixed mesh becomes inconvenient, because it requires the explicit tracking of the domain boundary. Therefore, the arbitrary Lagrangian-Eulerian (ALE) formulation is used to discretise the flow equations on moving and deforming meshes. This method blends both Lagrangian and Eulerian frameworks. The Lagrangian contribution allows the mesh to move and deform according to the boundary motion, whereas the Eulerian part takes care of the fluid flow through the mesh.

In general, the transport equation (3.2) for a scalar field ϕ can be modified for a moving mesh as

$$\frac{\partial}{\partial t}\int_{V_P}(\rho\phi)\,dV + \oint_{\partial V_P} d\boldsymbol{S}\cdot(\rho\phi\,(\boldsymbol{U}-\boldsymbol{w})) \;=$$
$$= \oint_{\partial V_P} d\boldsymbol{S}\cdot(\rho\Gamma_\phi\nabla\phi) + \int_{V_P} S_\phi\,(\phi)\,dV,$$

where $\boldsymbol{w}$ is the relative velocity of the mesh. The relationship between the rate of change of the volume V_P and the mesh velocity, $\boldsymbol{w}$ is defined by the so-called Space Conservation Law (SCL) [34]

$$\frac{\partial}{\partial t}\int_{V_P} dV - \oint_{\partial V_P} d\boldsymbol{S}\cdot\boldsymbol{w} = 0.$$

The rate of change of the volume is handled automatically in OpenFOAM [63], whereas the mesh motion flux correction needs to be accounted for and it is calculated as

$$\sum_f \boldsymbol{S}_f\cdot\rho\phi_f\,(\boldsymbol{U}_f-\boldsymbol{w}_f)\,.$$

Given the displacement of the membrane interface calculated from the structural solver, the mesh velocity, $\boldsymbol{w}$, is calculated solving a Laplace smoothing equation for every cell center

$$\nabla\cdot(\gamma\nabla\boldsymbol{w}) = 0, \tag{3.10}$$

where γ is the diffusivity. The updated position of the mesh points at the new time step is given by

$$\boldsymbol{x}_{new} = \boldsymbol{x}_{old} + \Delta t\boldsymbol{w}.$$

Equation 3.10 can be compared with the diffusion term of the Navier-Stokes equations where the diffusivity γ is equivalent to the molecular viscosity. However, when the diffusion equation is solved for the mesh points displacement the *mesh viscosity* does not have a physical meaning and its value is chosen only to preserve the final mesh quality and avoid

numerical instabilities. For this reason the diffusivity can be treated as a field value and calculated with many different methods. In this way it is possible to control the local deformation of the cells in such a way the higher the value of the diffusivity the more rigid the cells is and more resistence opposes to distortion. In OpenFOAM two main approaches are available [63]:

Distance-based, where the diffusion field is a function of the cell centre distance, l, to the nearest selected boundary:

- Linear: $\gamma = \frac{1}{l}$,
- Quadratic: $\gamma = \frac{1}{l^2}$,
- Exponential: $\gamma = e^{-l}$.

Quality-based, where the diffusion field is a function of the local mesh quality measure:

- Mean cell non-orthogonality,
- Mean cell skewness,
- Combination of non-orthogonality and skewness.

The main argument of the distance-based approach is that the mesh quality is preserved in proximity of the selected boundary and most of the internal mesh deformation happens in the far field where the mesh grid is coarser and can absorb more easily the deformation without worsen the mesh quality. However in this work the mesh motion is solved not in the whole domain but only in a small subset around the membrane as will be explained in Section 4.4. In this condition a distance-based diffusivity field did not prove to be more efficient or generate a better quality mesh than a uniform field, therefore a constant value of $\gamma = 1$ has been adopted in the small domain around the membrane where the mesh motion is solved.

Figure 3.5 shows a particular of the mesh in proximity of the 2D membrane in its most deformed configuration using a uniform diffusivity. It is

possible to see how the deformation of the cells is mainly a shearing deformation and therefore the error induced by the skewness is negligible. In fact if we consider the face between two quadrilateral cells, its face centre correspondes with the intersection on that face between the line that connects the two cell centres (see Fig. 3.3d). On the contrary the non-orthogonality increases when the membrane moves. However the maximum non-orthogonality value experienced in all the simulations of this work has always been smaller than 30° and in has been taken into account performing 2 additional non-orthogonal corrections in the PIMPLE loop (see Sec. 3.2 on page 60).

An other note must be done on Fig. 3.5 where a gap at the interface between the solid and fluid mesh is visible. Generally the solid and the fluid meshes are not conformal as they do not share the same points and faces. The displacements are calculated from the structural equations on the solid mesh (yellow) and need to be interpolated to the membrane interface on the fluid mesh (gray). At each time step subiterations are performed in order to avoid the lag between the displacement solution from the solid solver and the pressure solution from the fluid solver. For the solution to be considered converged at a certain time step, a dynamic equilibrium at the membrane interface must be satisfied. This means that the difference between the fluid and solid mesh at the membrane interface needs to be smaller than a threshold value in order for the pressure distribution to be consistent with the true shape of the membrane. The averaged magnitude of the displacement difference at each face of the fluid

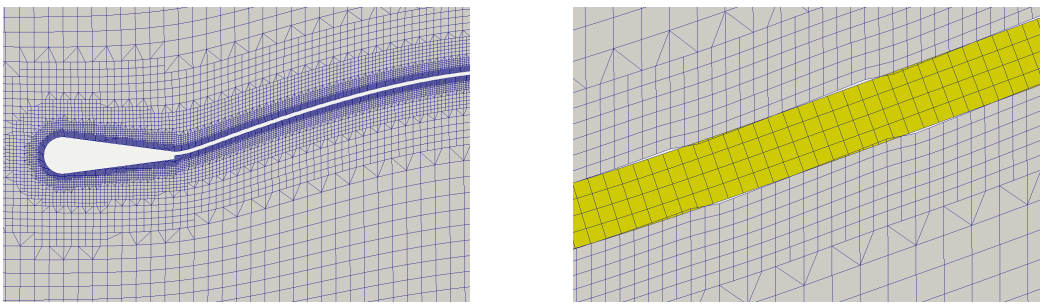

Figure 3.5: Particular of deformed mesh (grey: fluid, yellow: solid).

mesh is defined as the FSI residual and is used to judge when the FSI solution is converged for each time step. In particular when the FSI residual is smaller than 1/1000 of the membrane thickness the solution is considered converged. Therefore the gap between the solid and the fluid in Fig. 3.5 is considered to be smaller in average than the threshold value and the error given by that difference negligible. A more detailed explanation of the FSI algorithm is given in the next section.

3.3 Fluid-Structure interaction algorithm

In problems involving strong deformations, such as a membrane wing, a partitioned strong coupling algorithm (1.2) is the most suitable in order to avoid numerical instabilities due to the artificial added mass effect. Strong coupling enforces continuity of velocity and stress at the fluid/solid interface through fixed-point iterations at each time step. In such an algorithm the following tasks are looped at each time step until convergence:

1. Set pressure from the previous iteration (or previous time step at the first iteration) on the solid patch by interpolating the fluid pressure on the fluid side of the boundary and update the traction forces on the solid boundary accordingly.

2. Solve solid equation with the external pressure calculated previously as boundary condition.

3. Move the fluid mesh in accordance with the previously calculated solid deformations.

4. Solve the fluid motion on the updated geometry and mesh.

In case of strong interaction, the pressure solution (point 1) and the displacement solution (point 3) might have strong gradients especially at the first iteration and they eventually need to be under-relaxed in order to avoid instabilities. Because of under-relaxation the convergence might be

very slow and computationally expensive due to the large number of iterations. Hence, Mok et al. [87] introduced a dynamic relaxation factor based on the Aitken method for enhanced robustness and stability which is briefly introduced below.

A generic solution g_k^n (displacement or pressure) at time n and iteration k is under-relaxed with

$$\tilde{g}_k^n = \lambda_k \tilde{g}_{k-1}^n + (1 - \lambda_k)\, g_k^n, \tag{3.11}$$

where $\tilde{}$ denotes the relaxed solution and λ_k is the relaxation factor. With the Aitken method, the relaxation factor is calculated at each iteration as

$$\lambda_k = \lambda_{k-1} + (\lambda_{k-1} - 1)\, \frac{(\boldsymbol{Q}_{k-1} - \boldsymbol{Q}_k) \cdot \boldsymbol{Q}_k}{\|\boldsymbol{Q}_{k-1} - \boldsymbol{Q}_k\|^2}. \tag{3.12}$$

where $\boldsymbol{Q}_k = \tilde{g}_{k-1}^n - g_k^n$ is the difference between the relaxed solution at the previous iteration and the original numerical solution at the current iteration. The calculated λ_k is set to be in a range $[\lambda_{min}, \lambda_{max}]$ which depends on the specific application, but usually set to $[0, 1]$.

Figure (3.6) better explains how an under-relaxed solution leads to convergence at each time step. The red line represents the normalized FSI residual (values on the left), defined as the difference between the calculated solid displacement and the fluid mesh displacement at the interface fluid/solid, the latter being the under-relaxed solution of the solid displacement. As the number of iterations for each time step is variable, the x-axis shows the total number of iterations and the change in time step can be easily identified by the peaks of the quantities plotted. The FSI residual can be seen as a measure of the gaps between the solid mesh and the fluid mesh at the interface. The green and the blue line represent the mean incremental displacement of the solid patch and the fluid patch, respectively.

At the first iteration, from the displacement of the previous time step ①, the pressure distribution is calculated ④, and consequently the relative

incremental displacement of the membrane ②. The difference between ① and ② is the reference value for the normalization of the FSI residual, which therefore is equal to unity at the first iteration ③. At the second iteration, the fluid mesh interface is moved by an under-relaxed value of the structural displacement ⑥ (note ⑥≠②). The pressure distribution is calculated for this new configuration ⑤ and then a new structural displacement ⑦. Going ahead with this procedure the convergence is reached when the difference between the structural displacement and the fluid mesh interface ⑧ is smaller than a tolerance value ⑩ and consequently the pressure distribution is not changing anymore ⑨. This is a condition of *dynamic* equilibrium at each time step.

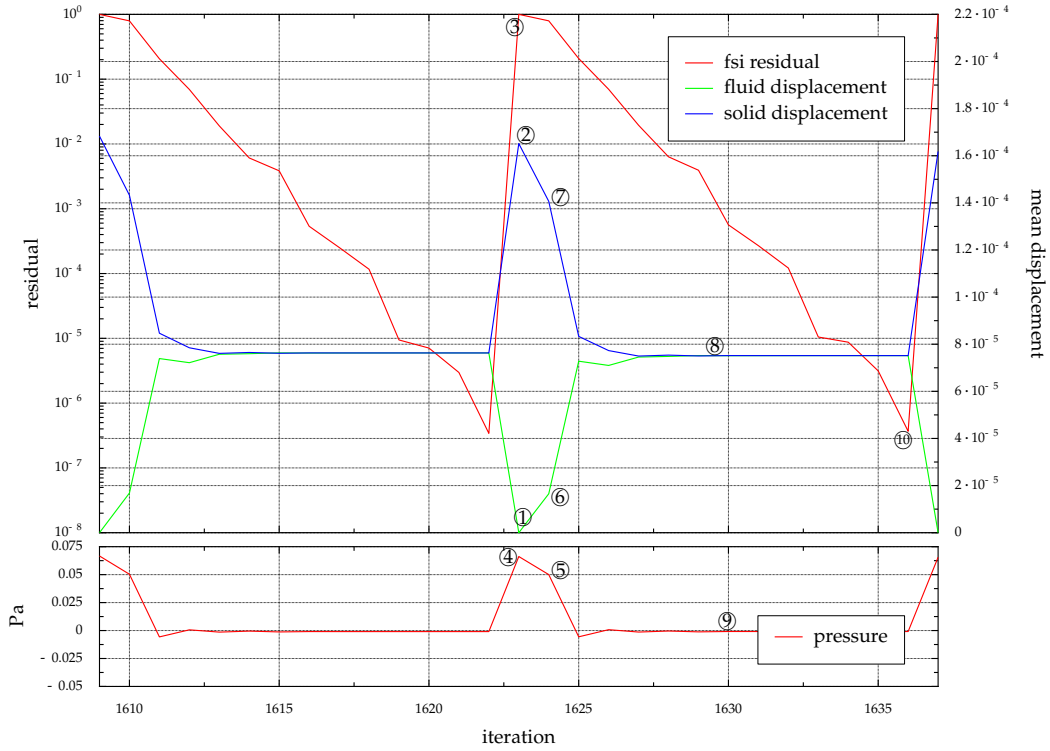

Figure 3.6: FSI Residuals

Chapter 4

Validation

This section deals with the validation and verification of the existing OpenFOAM solvers of the version 3-extend as well as the modified ones, that have been used throughout the current research. To validate the flow solver accuracy `simpleFoam` has been used for steady state simulations whereas unsteady cases have been simulated with `pimpleFoam`. For the validation of the structural and FSI code `elasticNonLinULSolidFoam` and `icoFSIelasticNonLinULSolidFoam` have been used, respectively. These solvers are the building blocks of the original solver developed as original work of this thesis, `pimpleFsiHyperElasticULSolidFoam` which will be presented in Chapter 5.1 and 6.

The accuracy of the OpenFOAM solvers has been evaluated simulating a 2D flow around the membrane wing geometry of Rojratsirikul et al. [103] (Fig. 4.1), and comparing the results (deflection and pressure distribution)

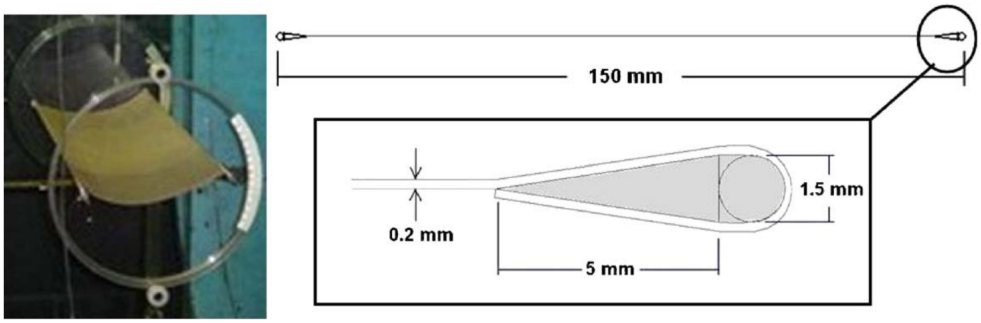

Figure 4.1: Membrane wing geometry of Rojratsirikul et al. [103].

Fluid ($Re = 2{,}500$)			
kinematic viscosity	$\nu =$	$1.44 \cdot 10^{-5}$	$[\mathrm{m}^2/\mathrm{s}]$
fluid density	$\rho_f =$	1.21	$[\mathrm{kg}/\mathrm{m}^3]$
freestream velocity	$U_\infty =$	0.24	$[\mathrm{m}/\mathrm{s}]$
Solid			
solid density	$\rho_s =$	534.5175	$[\mathrm{kg}/\mathrm{m}^3]$
Young's modulus	$E =$	2613.6	$[\mathrm{kg}/(\mathrm{m}\,\mathrm{s}^2)]$
Poisson's ratio	$\nu_p =$	0.45	$[-]$
Membrane geometry			
chord	$c =$	0.15	$[\mathrm{m}]$
thickness	$h =$	$2 \cdot 10^{-4}$	$[\mathrm{m}]$

Table 4.1: Dimensional parameters used for the simulations in OpenFOAM

with the reference data by Gordnier [51], based on numerical simulations on the same geometry with a high fidelity solver.

In Gordnier's work the fluid and solid equations are solved with a finite-difference approach with second-order temporal and sixth-order spatial accuracy. The setup (Fig. 4.1) consists of a 2D membrane 15 cm long with tear-shaped leading and trailing edges, at $Re = 2{,}500 - 10{,}000$ and with angle of attack varying between 4° and 20°. In Gordnier's work the governing equations have been solved in their nondimensional form. In particular, to characterize the solid part, its nondimensional modulus of elasticity, $\tilde{E}$, thickness, $\tilde{h}$, and mass ratio, $\tilde{\rho}$, have been assigned. These quantities have been nondimensionalized by the fluid density, ρ_f, dynamic pressure, $\rho_f U_\infty^2$, and chord length, c, as follows

$$\tilde{E} = \frac{E}{\rho_f U_\infty^2}\,, \qquad \tilde{h} = \frac{h}{c}\,, \qquad \tilde{\rho} = \frac{\rho_s}{\rho_f}\,. \tag{4.1}$$

Since Gordnier's computations assume a nondimensional mass ratio of $\tilde{\rho}\tilde{h} = 0.589$ and a nondimensional modulus of elasticity, $\tilde{E}\tilde{h} = 50$, given the fluid parameters all the dimensional values needed by an OpenFOAM simulation can be easily computed. They are reported in Table 4.1.

Before simulating the complete FSI case, a grid independence study has been performed separately on the fluid and on the structural domains,

respectively. A domain independence study has also been carried out for the fluid mesh in order to be sure that the solution does not depent on the size of the computational domain.

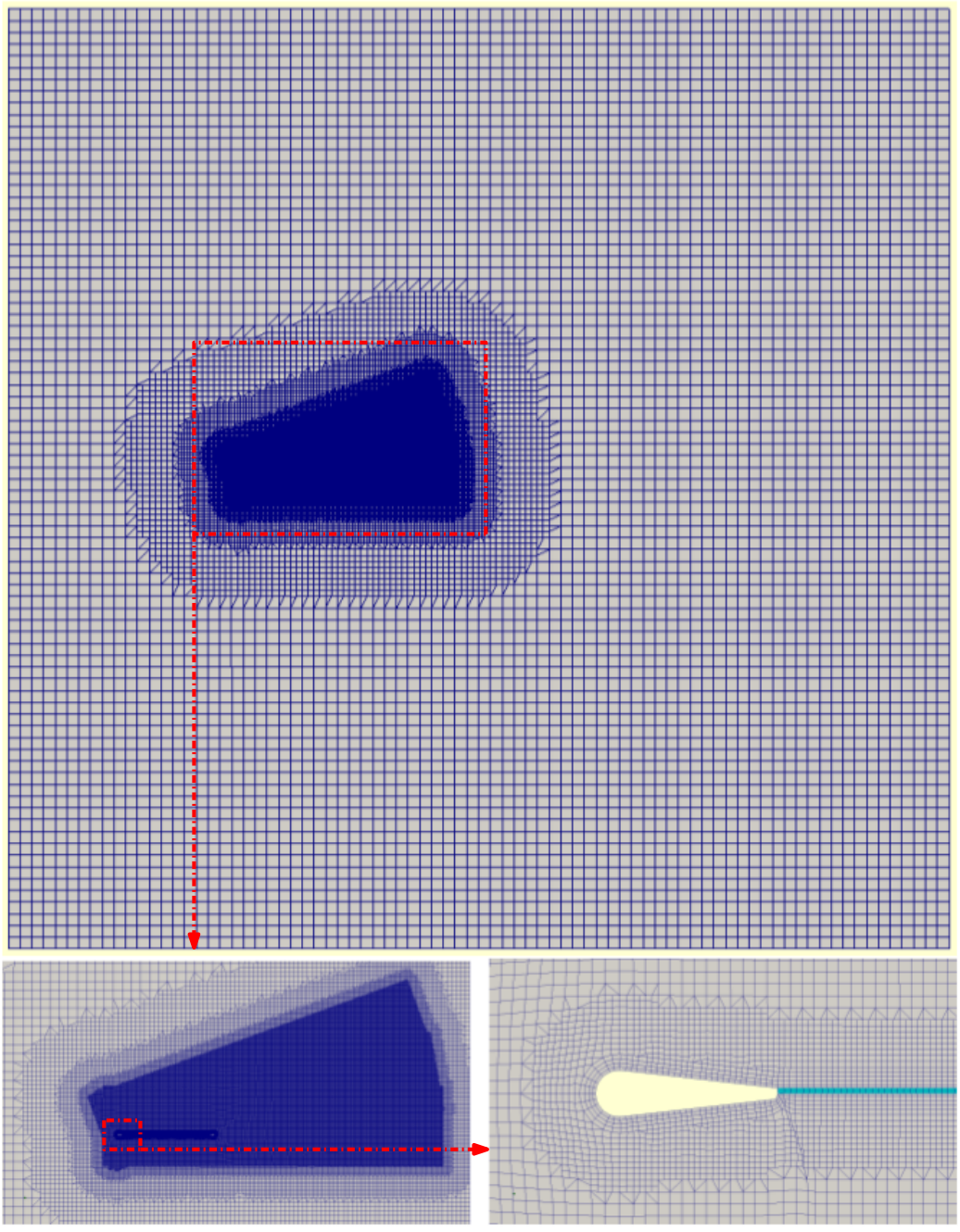

Figure 4.2: Fluid and solid mesh.

An unstructured mesh for the fluid domain has been generated with the OpenFOAM utility `snappyHexMesh`, with a finer grid resolution in proximity of the membrane, whilst `blockMesh` has been used to generate a structured mesh for the membrane (Fig. 4.2).

The bottom right of Fig. 4.2 shows the solid mesh for the membrane in light blue. Since the leading and trailing edges are fixed the origin of the membrane's reference system has been taken where the membrane attaches to the leading edge and its nondimensional length corresponds to the actual deformable length as shown in Fig. 4.3. The pressure distribution and the membrane displacement will be presented in this reference system.

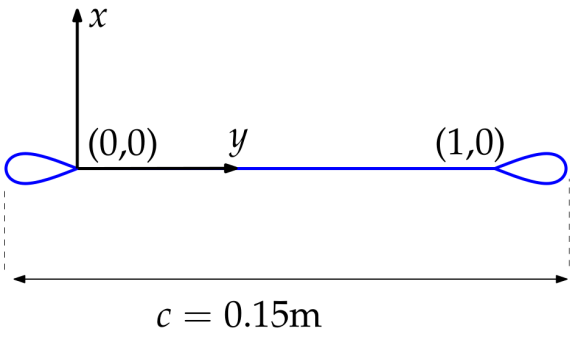

Figure 4.3: Membrane reference system.

4.1 Grid and Domain analysis

4.1.1 Fluid grid convergence study

The grid and domain independence study for the fluid part has been performed for a laminar and steady flow around the membrane, frozen at its initial condition (flat plate) and with the angle of attack varying from $\alpha = 0°$ to $\alpha = 3°$. The computational domain is squared and the membrane is equidistant from the top and the bottom and at 33% of the domain

length from the inlet. The quantities of interested measured are the lift and the drag coefficient defined as

$$C_l = \frac{L}{0.5\rho_f U_\infty^2} \qquad \text{and} \qquad C_d = \frac{D}{0.5\rho_f U_\infty^2},$$

where L and D are the lift and drag, respectively.

The values of the drag and lift coefficient at $Re = 2{,}500$ and $Re = 5{,}000$ and for a squared domain size of $36c$ are reported in Fig. 4.4. The cell counts of $1 \cdot 10^4$, $2.3 \cdot 10^4$, $3.4 \cdot 10^4$ and $2.3 \cdot 10^5$ have been tested and it has been found that the variation of the solution between domains with $3.4 \cdot 10^4$ and $2.3 \cdot 10^5$ cells is negligible.

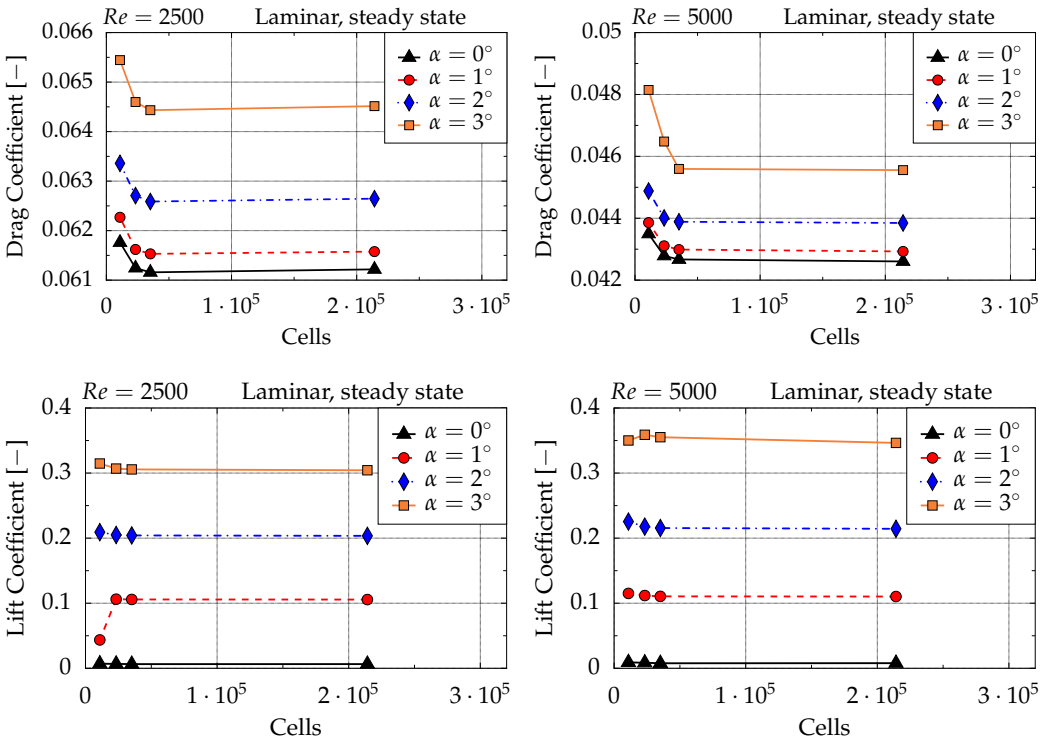

Figure 4.4: Grid refinement study.

Keeping the same density of cells around the membrane from the previous case with $3.4 \cdot 10^4$ cells, the domain size has been changed to examine when the solution can be considered independent of it. Six domain sizes have been tested in total and their characterisitcs are shown in Table 4.2

along with a sketch of one of the domains.

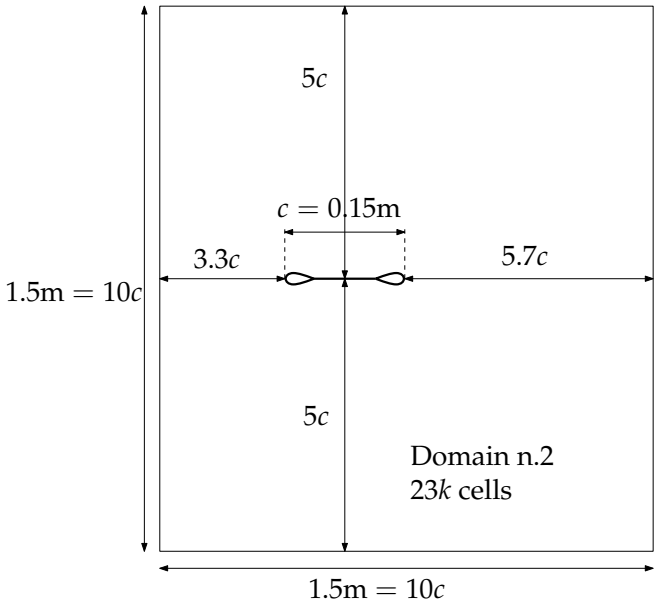

Domain n.	cells	nondim. domain length
1	22k	6c
2	23k	10c
3	27k	24c
4	34k	36c
5	40k	44c
6	92k	88c

Table 4.2: Different domain sizes.

Furthermore, different boundary conditions (Fig. 4.5) have been tested in order to check whether they might give different results (in particular the top and the bottom boundaries). In Fig. 4.5a the top and bottom boundaries are treated as inlet/outlet. With such boundary conditions, the membrane remains fixed at different angles of attack and the free-stream velocity, U_∞, is given at the inlet in terms of vertical and horizontal components to obtain the angle of attack needed. On the other hand, if slip or free stream boundary conditions are given at the top/bottom (Fig. 4.5b), U_∞ is always perpendicular to the inlet and a new mesh is generated for

each angle of attack since the membrane has to be rotated by the angle of attack needed.

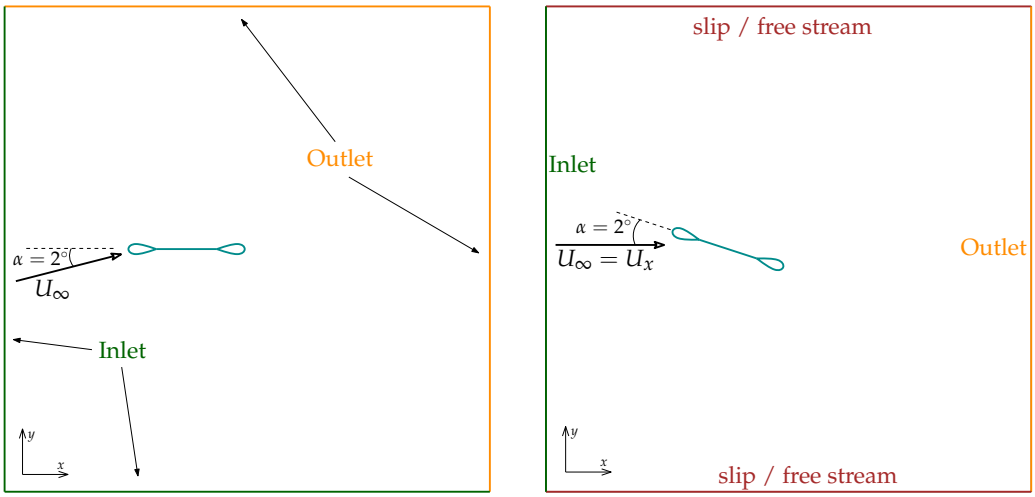

(a) (b)

Figure 4.5: Different boundary conditions tested for the domain study.

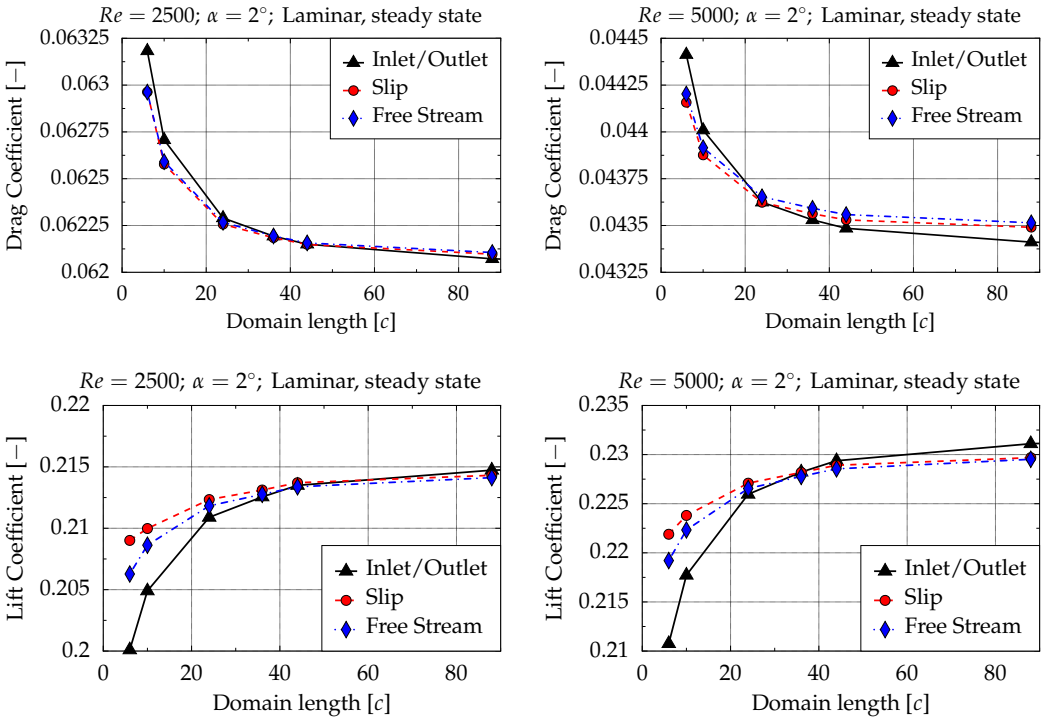

Figure 4.6: Computational domain study.

Figure 4.6 displays the values of C_l and C_d at $Re = 2{,}500$ and 5,000 for $\alpha = 2^\circ$ and for different domain sizes and for different boundary conditions. These results show that the solution converges faster with a slip boundary condition rather than with free-stream or inlet/outlet boundary condition. However when the domain is large enough ($> 80c$) the difference between solutions with different boundary conditions is less than 0.01%. Thus, the Inlet/Outlet boundary condition and a domain of $80c$ will be used for the following simulations because it will be computationally cheaper to change the angle of attack while the simulation is running and eventually assign a time-varying inlet boundary condition without moving the mesh.

4.1.2 Time step study for the unsteady fluid solver

Increasing the angle of attack the flow becomes unsteady and the influence of the time step needs to be analysed in order to accurately predict the vortex shedding frequency and the mean force coefficients. At $Re = 2{,}500$ and $\alpha = 8^\circ$ the flow detaches from the leading edge of the fixed membrane and vortices are shed. The force coefficients history of the last 5 seconds of simulation is shown in Fig. 4.7 for time steps going from $\Delta t = 0.02$ s

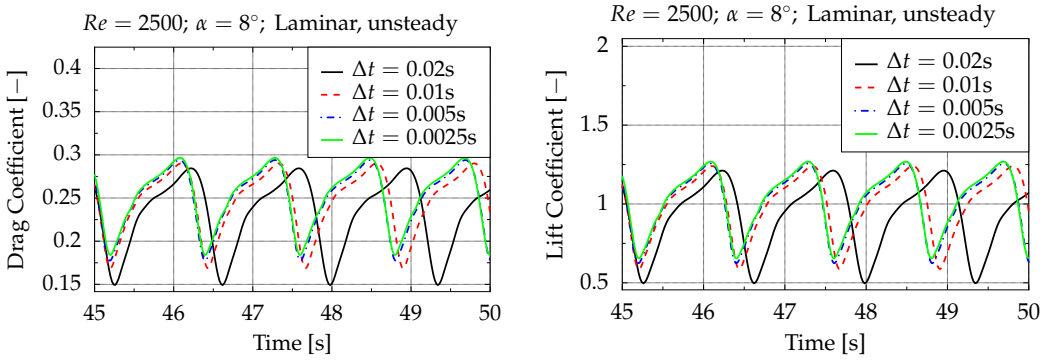

Figure 4.7: Comparison between unsteady simulations with different Δt.

to $\Delta t = 0.0025$ s. For $\Delta t = 0.02$ s the max CFL has been $CFL = 15$ in proximity of the leading edge whereas with $\Delta t = 0.0025$ s the max CFL was $CFL = 2$. Even though `pimpleFoam` can handle CFL numbers larger than unity, the lack of accuracy given by using very large Δt can be clearly seen in Fig. 4.7 and in Tab. 4.3 where the mean force coefficients and the Strouhal number are reported. The Strouhal number is the nondimensional frequency and it is defined as

$$St = \frac{f \cdot c}{U_\infty},$$

where f is the frequency in Hz, c is the chord length and U_∞ is the freestream velocity.

Δt [s]	$\bar{C}_l$	$\bar{C}_d$	St
0.02	0.942	0.234	0.547
0.01	0.987	0.244	0.641
0.005	1.002	0.249	0.657
0.0025	0.997	0.251	0.658

Table 4.3: Mean force coefficients for different Δt.

The time step convergence is achieved with $\Delta t = 0.005$ s as the mean force coefficients and the Strouhal number calculated with $\Delta t = 0.0025$ s and $\Delta t = 0.005$ s differ by less than 1%.

4.1.3 Solid grid convergence study

4.1.3.1 Steady solution

In order to evaluate the dependence of the solution on the solid grid, steady and unsteady simulations with the structural solver only have been performed. For the steady case the pressure distribution around the membrane in its initial undeformed state (flat plate) at $\alpha = 4^\circ$ and $Re = 2{,}500$ has been calculated and used as boundary condition for the solid solver. The pressure distribution of the flat plate at $\alpha = 4^\circ$ is shown in Fig. 4.8.

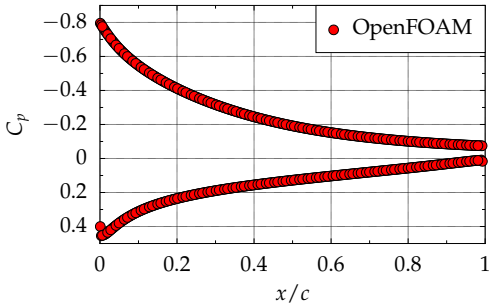

Figure 4.8: Pressure distribution around a flat membrane at $\alpha = 4°$.

Note that the jump in pressure at $x/c = 0$ and $x/c = 1$ is due to the origin of the membrane not corresponding with the membrane's leading edgebut right behind it where the membrane starts to displace (Fig. 4.3). As the fluid solver is frozen during these simulations the pressure distribution is fixed and acts as an external force while the membrane is reaching the equilibrium. The parameters of the solid mesh which have been analyzed are the cell aspect ratio (length-width ratio), ar, and the total number of cells. In this way it is possible to evaluate if varying the number of cells only streamwise (along the chord) or only widthwise (along the thickness) has an effect on the solution. For instance when the aspect ratio is kept constant, doubling the number of cells lengthwise implies doubling the number of cells widthwise, or also, two grids with the same total number of cells can have different aspect ratio (600×4 or $1{,}200 \times 2$). Different

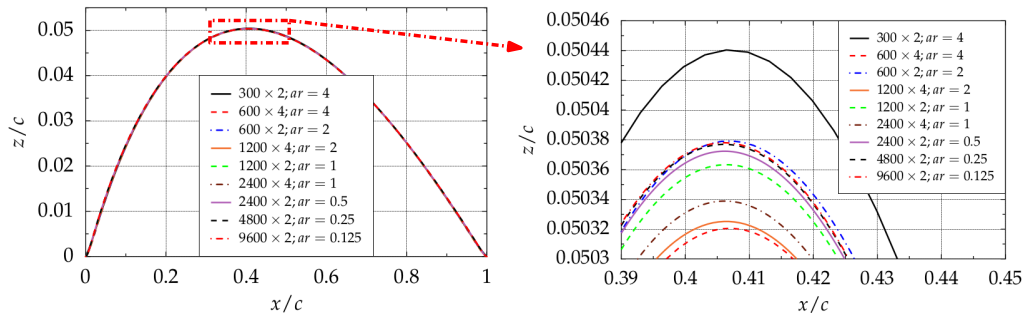

(a) Steady solution for pressure distribution at $\alpha = 4°$

(b) Maximum displacement

Figure 4.9: Solid grid convergence study

combinations have been simulated (Fig. 4.9), showing that the solution is not very sensitive to these parameters with the difference of the maximum displacement being less than 0.3% (Fig. 4.9b).

4.1.3.2 Unsteady solution

A dynamic test with the unsteady structural solver has been performed as well to verify the effect of different mesh resolution on the amplitude and frequency of the membrane's oscillations. In this case the OpenFOAM FSI solver `icoFSIelasticNonLinULSolidFoam` has been run at $\alpha = 8°$ and $Re = 2{,}500$ starting from a flat membrane in order to obtain the initial condition for the structural solver. When the membrane started oscillating around its equilibrium shape the fluid solver has been switched off. As the pressure distribution was not updating anymore at each time step it was possible to isolate the effect of the solid mesh resolution and time step of the structural solver on the dynamic behavior of the membrane. The shape of the membrane at the end of the FSI simulation used as initial condition for the structural solver simulations is shown in Fig. 4.10 along with the time history of the midpoint displacement calculated with the structural solver only, with a time step $\Delta t = 0.005$ s and a solid mesh of 600×2.

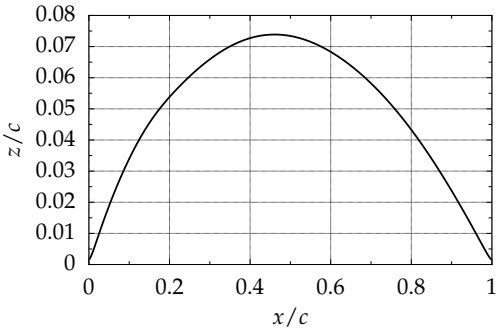

(a) Initial condition.

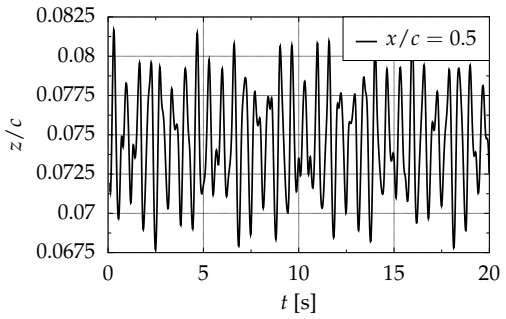

(b) Time history of the midpoint displacement.

Figure 4.10: Unsteady structural solver.

Figure 4.11 shows the spectra of the midpoint displacement for all the mesh resolution tested and a time step $\Delta t = 0.005$ s. All these simulations predict a main peak at 1.63 Hz and a smaller one at 2.2 Hz with the error in amplitude around the first peak being smaller than 0.1% of the mean displacement.

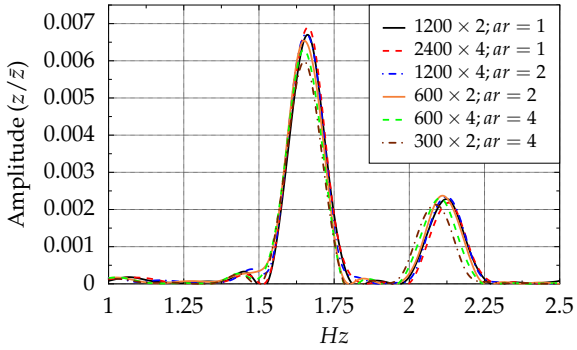

Figure 4.11: Spectrum of the midpoint displacement for different mesh resolutions and $\Delta t = 0.005$ s.

4.1.4 Time step study for the unsteady solid solver

The same test has been performed with different time steps using the mesh 600×2. The results are reported in Fig. 4.12 showing that all the time steps

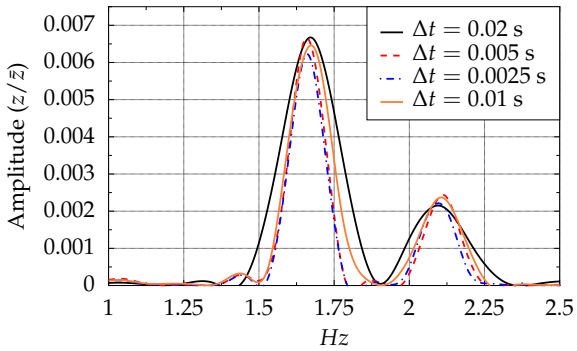

Figure 4.12: Spectrum of the midpoint displacement for different time steps and mesh resolution 600×2.

tested are small enough to capture the two frequencies at 1.63 Hz and 2.2 Hz. Since flow simulations were time resolved with a time step $\Delta t = 0.005$ s the same will be used for the FSI simulations as it is a good compromise between computational cost and accuracy.

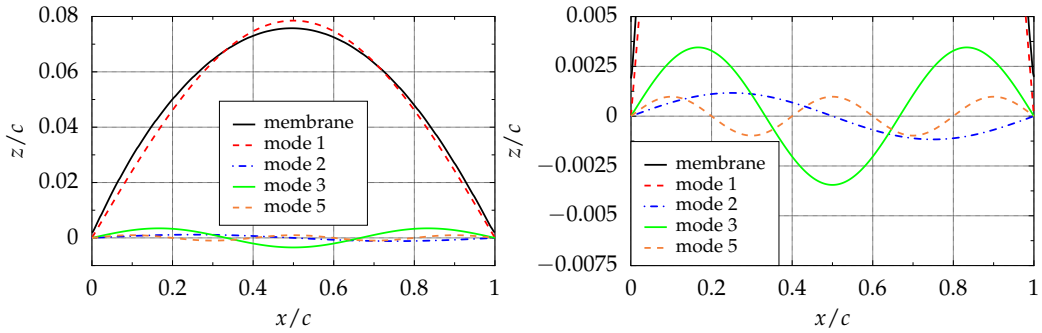

Figure 4.13: Shape of the spatial modes (zoom on the right).

An additional note can be made on the shape of the spatial modes. A Fourier analysis of the shape of the membrane shows that up to the fifth spatial mode has a contribution to the final shape (Fig. 4.13). The second spatial mode is responsible to the shift of the point of maximum displacement towards the leading edge. In particular the nondimensional amplitude of each mode is reported in the following table

mode	z/c
1	0.0785
2	0.0018
3	0.0034
5	0.0009

4.2 Fluid-structure interaction

The solver which has been used for the validation is `icoFsiElastic-NonLinULSolidFoam`, available in the OpenFOAM-extend version. It

solves the N-S equations for a laminar and incompressible flow using the PISO algorithm (Sec. 3.2.2), but also solves the Laplace smoothing equation to calculate the movement of the mesh for all the points of the mesh, which might become computationally very expensive for external flows where the moving boundary (the membrane) is several orders of magnitude smaller than the domain length. In fact, depending on the resolution of the mesh around the moving body, the displacement of the mesh points will be higher near the fluid-solid interface and virtually zero far away from it. In particular for the grid used in this study the displacement of a point whose location is further than 4-5c from the membrane is negligible. Solving the Laplace smoothing equation for the whole domain means that a big matrix containing the coordinates of all the points of the mesh is generated, stored and solved for each sub-iteration of the FSI algorithm (Sec. 3.3), even though the calculated displacement will be non-zero only for a small portion of the grid points. The computational resources requested (memory, I/O operations and computation) therefore become much larger than what is actually needed. This issue has been addressed in the current work by making it possible to specify only the region of the domain where the mesh motion is needed (Sec. 4.4).

The results of the validation simulations are in good agreement with the reference [51]. Figures 4.14 and 4.15 show the mean displacement and the mean pressure distribution at $Re = 2{,}500$ for angles of attack $\alpha = 4^\circ$

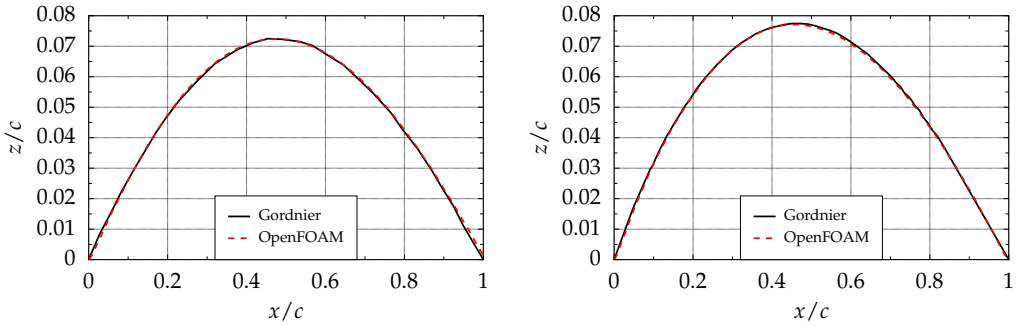

(a) $\alpha = 4^\circ$. (b) $\alpha = 8^\circ$.

Figure 4.14: Mean displacements for $Re = 2{,}500$, compared with Gordnier [51].

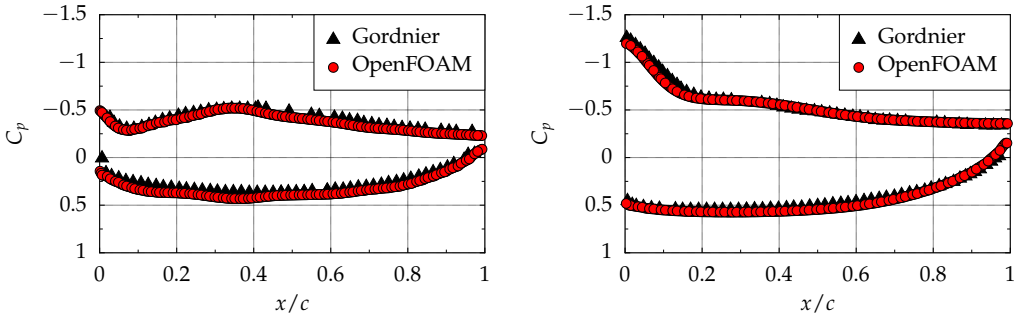

(a) $\alpha = 4°$ (b) $\alpha = 8°$

Figure 4.15: Mean pressure distribution for $Re = 2{,}500$.

and $\alpha = 8°$. At $\alpha = 4°$ the mean displacement and pressure distribution coincide with the equilibrium values since after a transient of 25 nondimensional time-units the membrane reaches a steady shape as shown in Fig. 4.16 by the time history of the displacement of the membrane midpoint.

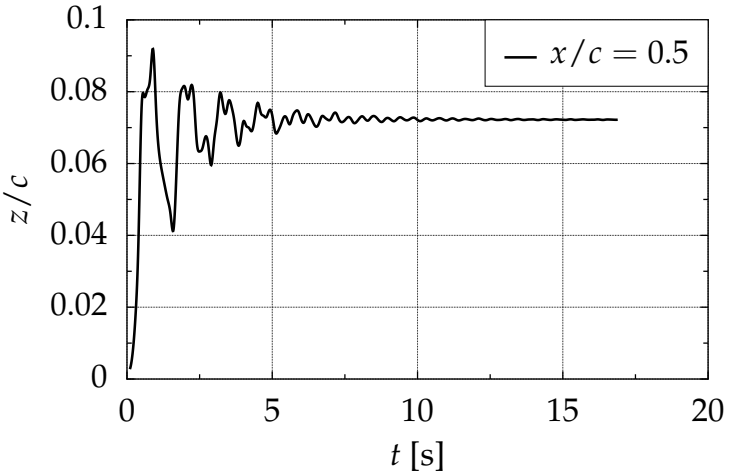

Figure 4.16: Displacement history of the membrane midpoint for $\alpha = 4°$, $Re = 2{,}500$.

The position and the value of the maximum displacemement of the membrane (Fig. 4.14) calculated with OpenFOAM match those of Gordnier, with only minor discrepancies on the sides of the membrane (error not larger than 0.8% at $\alpha = 4°$ at $x = 0.87c$). There is good agreement also

in the pressure distribution (Fig. 4.15): the maximum error ($\varepsilon = 4.8\%$) is for the case at $\alpha = 4^\circ$ where OpenFOAM overestimates the pressure on the bottom side of the membrane and underestimates the one on the back section of the suction side. However this discrepancy has a minor effect on the total lift generated by the membrane, and therefore on the final displacement, because the pressure difference between the top and bottom side of the membrane (Fig. 4.15a) obtained from the current case and the reference simulation are comparable ($\varepsilon < 0.4\%$). Even better agreement with the reference is obtained at $\alpha = 8^\circ$ (Fig. 4.15b).

At $\alpha = 8^\circ$ the interaction between fluid and structure becomes significant and the membrane starts to oscillate, developing a third mode standing wave response. This can easily be seen in a contour plot (Fig. 4.17[1]) where the perturbation around the mean displacement of each point of the membrane (x-axis) is reported for each time (y-axis).

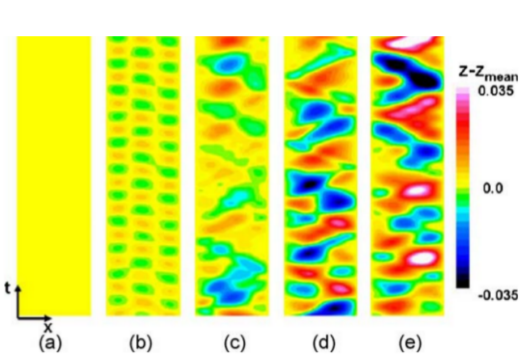

(a) Gordnier [51]: (a) $\alpha = 4^\circ$, (b) $\alpha = 8^\circ$, (c) $\alpha = 12^\circ$, (d) $\alpha = 16^\circ$, (e) $\alpha = 20^\circ$.

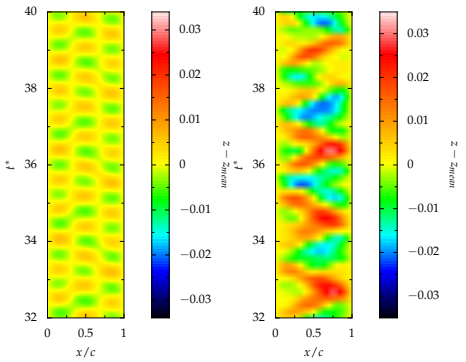

(b) OpenFOAM: $\alpha = 8^\circ$and $\alpha = 20^\circ$

Figure 4.17: Perturbation from the mean membrane deflection for various angles of attack.

The regular pattern for $\alpha = 8^\circ$ indicates that the membrane vibrates in its third structural mode around the mean shape, but as the angle of attack increases a large number of modes are excited and the behaviour appears more chaotic and with higher amplitudes of oscillation (darker colours).

[1]Note that Gordnier's plots did not report the time scale, therefore for the OpenFOAM plots time scale has been deducted from spectral analysis data

Also, the V-patterns at higher angles of attack (especially at $\alpha = 20°$) indicate that the maximum displacement travels back and forth between the leading and the trailing edge.

Whereas at $\alpha = 8°$ the amplitude and the frequency of the displacement calculated by OpenFOAM and Gordnier can be easily compared showing a good match (Fig. 4.18), at higher angles of attack the membrane exhibits a more complex behaviour and it is not possible to reproduce the exact results of Gordnier for the perturbation around the mean. At $\alpha = 20°$ although the vorticity field from OpenFOAM (Fig. 4.19) shows flow pat-

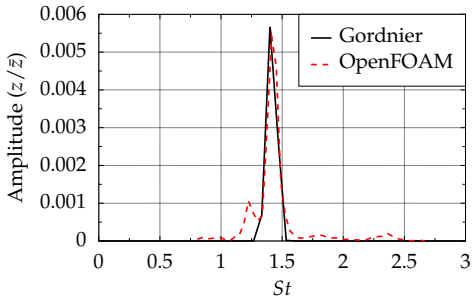

Figure 4.18: Spectral analysis of structural response for $\alpha = 8°$.

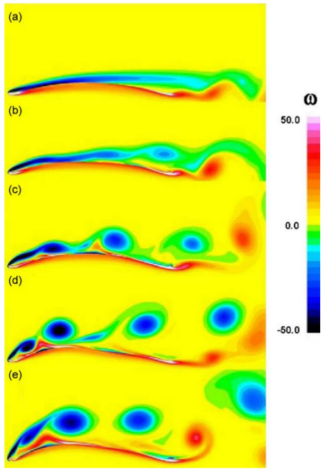

(a) Gordnier [51]: from top to bottom (a) $\alpha = 4°$, (b) $\alpha = 8°$, (c) $\alpha = 12°$, (d) $\alpha = 16°$, (e) $\alpha = 20°$.

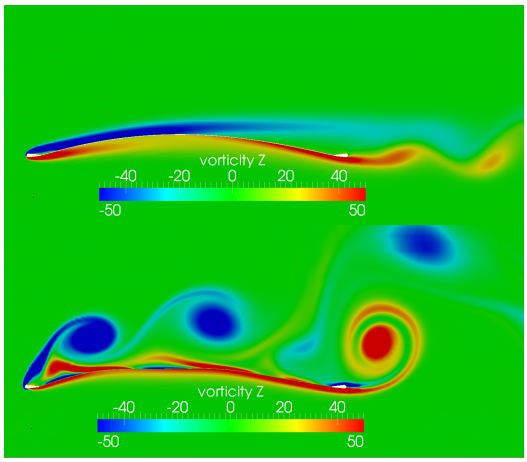

(b) OpenFOAM: top $\alpha = 4°$and bottom $\alpha = 20°$

Figure 4.19: Instantaneous vorticity contours for various angles of attack.

terns similar to Gordnier's simulations, it is quite difficult to compare the instantaneous displacement of the membrane. However if we consider statistical quantities we still obtain a good agreement in terms of mean displacement, amplitudes and frequencies of oscillations (Fig. 4.20). In particular at $\alpha = 20^\circ$ the Strouhal number of the structural response from both OpenFOAM and the reference are $St = 0.59\,, 1.09\,, 1.73$.

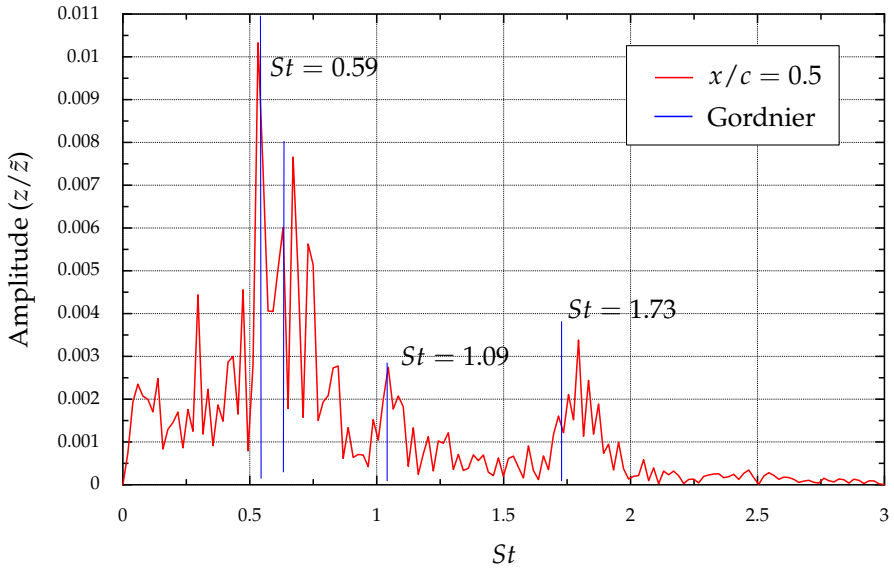

Figure 4.20: Spectral analysis of structural response for $\alpha = 20^\circ$, $Re = 2{,}500$.

Since `icoFsiElasticNonLinULSolidFoam` is a solver for strong coupled FSI problems (Sec. 1.2), the computational time is highly dependant on the number of sub-iterations performed at each time step. At each sub-iteration the fluid, the solid, and mesh motion equations are solved and therefore different time steps might require more clock time than others depending on the level of unsteadiness of the flow. In fact, the more the flow is unsteady the more the pressure fluctuations induce high displacements on the membrane. And since for stability reasons at each sub-iteration the mesh is moved by an under-relaxed value of the calculated solid displacement (Sec. 3.3) this means that more sub-iterations will be needed for each time step in order to minimize the fsi residual (i.e. nondimensional difference between the displacement of the membrane bound-

ary on the fluid and on the solid mesh). Generally high displacements are generated either at the beginning of a simulation when the membrane starts from its flat configuration (Fig. 4.16) or at high angles of attack ($\alpha \geq 12°$) when the flow is detached and therefore in these conditions a large number of sub-iterations are performed. For these simulations in the worst case ($\alpha = 20°$) up to 20 sub-iterations have been required for one time step and on average the wall-clock time for the simulation of one nondimensional time unit on a local machine (Intel® Core™ i7-2600 CPU @ 3.40GHz) using one processor has been around 2.5 hours. The solver also works in parallel however the maximum number of processors is limited by the number of subdomains the solid mesh can be decomposed into. In fact the OpenFOAM parallel libraries are written in such a way that each processor has to perform the same operations and therefore run the fluid, the solid and the mesh motion solver. Since for these particular simulations the solid mesh is far smaller than the fluid one, the benefits of a parallel simulation can only be obtained using up to 8 processors. In particular the average wall-clock time to simulate with 8 processors one nondimensional time unit (in the worst case described above) can decrease down to 30 minutes. More detailed values of number of sub-iterations for a typical simulation at different angles of attack are reported in Tab. 4.4 along with the minimum value of the fsi residual reached during subiterations.

α	sub-iter per Δt	fsi residual	cores	avg clock time per Δt
4°	5-10	1e-6	1	51
			4	17
			8	10
12°	10-15	1e-5	1	64
			4	23
			8	14
20°	10-20	5e-5	1	72
			4	26
			8	16

Table 4.4: Sub-iterations and clock time for simulations at different angles of attack.

It is worth noting that at $\alpha = 20^{\circ}$ more sub-iterations are needed to reach an fsi residual which is one order of magnitude larger than at 4°. This indicates that more computational effort is needed for the fluid interface to match a more complex shape of the membrane in order to calculate the accurate pressure distribution. For each time step is also reported the parallel scalability showing the average clock time per time step using 1, 4 or 8 cores.

4.3 Electrostriction

Further simulations have been performed to validate the electrostriction of a Neo-Hookean material in OpenFOAM. The reference case is an experiment conducted by Tagarielli [124] to investigate the electrostiction of rubbery polymers. For this experiment a rectangular specimen of the acrylic tape VHB4905 with an equi-biaxial prestrain (change in area of 300%) has been used and two compliant electrodes made of conductive grease have been applied on the top and bottom surfaces of the stretched polymer.

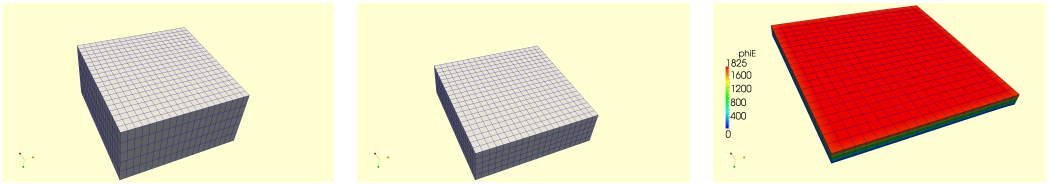

(a) Reference state. (b) Stretched state. (c) Effect of electrostriction.

Figure 4.21: Numerical simulation of electrostriction.

As explained in Section 1.4 a prestrain is needed to increase the electrical breakdown and to reduce the thickness of the polymer so a smaller voltage can be applied. Thus, the Maxwell stresses will be added to the mechanical stresses due to prestretch. The 3 stages of the simulation are shown in Fig. 4.21. Since only the in-plane strain (i.e. variation in area) due to electrostriction is measured from experiments, starting from the reference configuration (Fig. 4.21a), the stretched configuration is calculated

assuming symmetry boundary conditions on the sides so the area of the specimen remains constant while the thickness varies (Fig. 4.21b). The Cauchy stress tensor (eqn. 2.6) in the stretched configuration is calculated by transforming the 2nd Piola-Kirchhoff stress tensor (eqn. 2.13). From the stretched configuration, given a certain value of voltage, the electric stress is calculated with equation (2.14) and added to the mechanical stress due to prestretch. Now the final displacement (Fig. 4.21c), and therefore the in-plane strain is obtained by substituting the total 2nd Piola-Kirchhoff stress tensor (eqn. 2.13) into the momentum equation (eqn. 2.8) as shown in Sec. 2.2.2. The code which has been implemented in OpenFOAM to run these simulations is reported in the Appendix D. Figure 4.22 shows the non-linear response of the in-plane strain of the membrane.

The relative permittivity ε_R has been assumed to be constant whereas in reality it is sensitive to the load history, prestrain and frequency of electrical excitation. For values of relative permittivity varying between 2 and 5, the experimental curve can be matched in different sections. Lower values of ε_R give a more accurate prediction of the strain in the bottom part of the curve which is more suitable for an active control on the membrane's stiffness, i.e. $\phi < 1{,}500$ V. It would not be recommended to control the membrane at higher voltage, as for $\phi > 1{,}500$ V the strain is very sensitive to small variations of electric potential and an electric breakdown might eventually occur ($\phi \geq 2{,}000$ V).

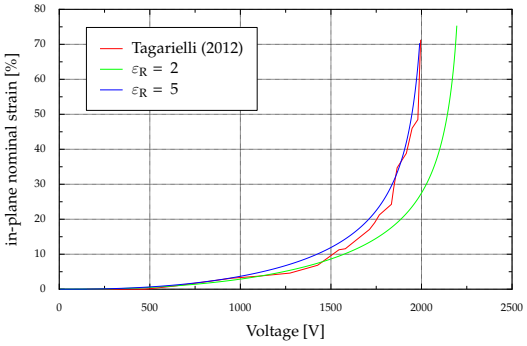

Figure 4.22: In-plane actuation strain with prestrain 300%.

4.4 FSI with electrostriction

Before including the effect of electrostriction in the FSI solver, the same cases as those described in Section 4.2 have been simulated with the Neo-Hookean model with and without prestrain. The values of μ and κ in equation (2.13) have been calculated with equation (2.10) using the same Young's modulus as that used earlier ($E = 2613.6$ Pa). It can be observed that without prestrain the Saint Venant-Kirchhoff and the Neo-Hookean formulation give the same results (Fig. 4.23) indicating that the strain induced by the flow on the membrane ($< 10\%$) is still in a range where the stress-strain curve shows a linear behaviour.

This simulation has proved that the Neo-Hookean formulation can be used to produce accurate results also for the cases simulated by Gordnier and therefore they can be extended to more complex physics where the Saint Venant-Kirkhoff formulation cannot be used due to its known limitiations [55, 81]. In particular the Saint Venant-Kirkhoff model fails in predicting the stress distribution when very large values of prestretch are applied. Moreover numerical simulations of a Saint Venant-Kirchoff material have shown a tendency to locally tangle the mesh when subject to strong compressive forces or kinematic constraints [35]. Therefore for realistic simulations of dielectric elastomers subject to large prestrain and compression loads due to electrostriction a Neo-Hookean formulation has been preferred.

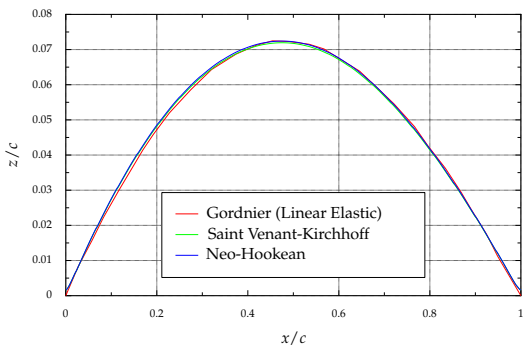

Figure 4.23: Membrane displacement for different constitutive laws at $\alpha = 4^\circ$, $Re = 2{,}500$.

The effect of electrostriction is now taken into account in the FSI simulations. A few modifications have been made to the solver `icoFsiElasticNonLinULSolidFoam` in order to make it more computationally efficient. The PIMPLE (merged PISO-SIMPLE) algorithm (Sec. 3.2.2) has been included in the solver in order to use a larger time step as the PIMPLE generally is more stable for $CFL > 1$, unlike the PISO algorithm. The PIMPLE algorithm in OpenFOAM also supports adaptive time stepping, i.e. it is possible to run simulations with a fixed value of CFL and the solver automatically adjusts the time step while the simulation is running. Further, the `subsetMotion` feature has been added so it is possible to select only the area near the membrane in which the mesh will be moving (green box in Fig. 4.24). Details of the code development of the `subsetMotion` are

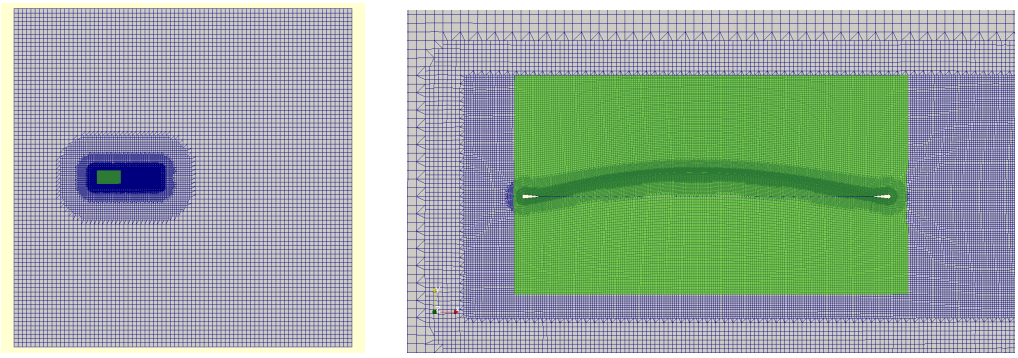

(a) Whole domain. (b) close-up of the moving mesh region.

Figure 4.24: subsetMotion mesh.

given in the Appendix C. Solving the Laplace smoothing equation only in a small region of the domain allows the solver to save computational time. It has been estimated that for each time step the reduction in time has been more than 40%. Also, in the previous simulations at each angle of attack the membrane started from its undeformed configuration (flat plate) and the transient to achieve periodical behaviour could last between 20 and 40 nondimensional time units. For these simulations a time-varying inlet boundary condition has been adopted, so it is now possible to assign a ramp-up input angle of attack and the membrane can smoothly adapt to

the flow conditions. In this way not only the physical transient has been reduced (up to 15%) but also the number of sub-iterations needed for each time step of the transient period.

Whereas the main effect of the Maxwell stresses is to stiffen the membrane in the thickness direction, they also induce an in-plane relaxation. This can easily be seen by writing the Maxwell stress tensor (eqn. 2.14) in matrix notation, neglecting edge effects and assuming that the potential ϕ varies only along the thickness h, i.e. $\boldsymbol{E} = -\nabla\phi \approx \left(0, 0, -\frac{\phi}{h}\right)$

$$\boldsymbol{\sigma}_m = \varepsilon_0\varepsilon_R \left[\underbrace{\begin{pmatrix} 0 & 0 & 0 \\ 0 & 0 & 0 \\ 0 & 0 & \left(\frac{\phi}{h}\right)^2 \end{pmatrix}}_{\boldsymbol{E}\otimes\boldsymbol{E}} - \frac{1}{2} \underbrace{\begin{pmatrix} \left(\frac{\phi}{h}\right)^2 & 0 & 0 \\ 0 & \left(\frac{\phi}{h}\right)^2 & 0 \\ 0 & 0 & \left(\frac{\phi}{h}\right)^2 \end{pmatrix}}_{(\boldsymbol{E}\cdot\boldsymbol{E})\cdot\boldsymbol{I}} \right]$$

$$= \varepsilon_0\varepsilon_R \begin{pmatrix} -\frac{1}{2}\left(\frac{\phi}{h}\right)^2 & 0 & 0 \\ 0 & -\frac{1}{2}\left(\frac{\phi}{h}\right)^2 & 0 \\ 0 & 0 & \frac{1}{2}\left(\frac{\phi}{h}\right)^2 \end{pmatrix}.$$

Then it is clear that the stress σ_{xx} and σ_{yy} have the same value of σ_{zz}, but with opposite sign. On the other hand, the stresses induced by an equibiaxial prestretch generally have the same absolute value for the x and y components but a different one for the z component of the stress tensor. Thus, for validation purposes, the value of the voltage ϕ which neutralizes the in-plane stresses induced by a given prestretch has been calculated and the results for this particular case have been compared with the case of the membrane without prestrain. By doing so, it is possible to find in which range of voltages the membrane can be controlled by modifying the stiffness. Such control of the stiffness translates to a control of the mean camber and consequently the aerodynamic performance of the membrane. The dimensional value of electric potential which creates the same in-plane stress of an equibiaxial prestrain of 300% ($\lambda_{pre} = 3$) is reported in Table 4.5 along with the other relevant parameters. Also, for the

purpose of this study the following assumptions have been made: (a) the material viscosity has been neglected, therefore hysteresis effects cannot be reproduced by these simulations; (b) the membrane thickness remains constant during prestretch and electric activation: since the membrane is already very thin, the effects of its variation on the flow field can be neglected; (c) electrostriction induces an instantaneous change in stiffness, as the electric time-scale is several orders of magnitude faster than the mechanical one.

Voltage	$\phi =$	1,390	$[\mathrm{V}]$
relative permittivity	$\varepsilon_R =$	1.66	$[-]$
shear modulus	$\mu =$	901.24	$[\mathrm{kg}/\left(\mathrm{m\,s^2}\right)]$
bulk modulus	$\kappa =$	8,712	$[\mathrm{kg}/\left(\mathrm{m\,s^2}\right)]$
Poisson's ratio	$\nu_p =$	0.45	$[-]$
in-plane stress for $\lambda_{pre} = 3$	$\sigma_{xx} = \sigma_{yy} =$	141.7	$[\mathrm{kg}/\left(\mathrm{m\,s^2}\right)]$

Table 4.5: Dimensional values for the FSI simulation with electrostriction.

4.5 Summary

In this chapter a study on the grid and time step resolution has been performed with the fluid and solid solvers available in OpenFOAM in order to find the best numerical setup for the FSI simulations of a membrane wing. It has been found that for the fluid solver a domain size of 88 chord length and 93k cells gives a mesh independent result whereas for the solid solver a mesh resolution 600×2 is enough to accurately predict the membrane displacement. For both fluid and solid solver a time step $\Delta t = 0.005$ s showed to give accurate results in the time domain.

These numerical settings have been used to validate the FSI solver against the results of Gordnier [51] of a passive membrane wing in a laminar flow at $Re = 2{,}500$. The OpenFOAM results showed good agreement with the reference. It is worth noting that the results from this validation have been obtained using a numerical approach which is quite different

from the one used in the reference. In fact, OpenFOAM uses a second-order finite volume approach for both the fluid and solid solver whereas Gordnier [51] solved the FSI problem of the membrane with a high-order finite-difference solver. Also the structural model is very different: in Gordnier a model for a one-dimensional membrane subjected to a normal force is adopted, whereas a Saint Venant-Kirchhoff constitutive equation is used in OpenFOAM. Therefore the good agreement of the results between the two approaches suggests that the level of accuracy of OpenFOAM in dealing with the FSI problem of a membrane in the range of parameters presented in this chapter can be considered more than satisfactory.

Moreover, a Neo-Hookean formulation for hyperelastic materials has been presented in order to simulate the effect of electrostriction of dielectric elastomers. This formulation coupled with the effects of the Maxwell stress tensor has been validated against the results of Tagarielli et al. [124] where the change in area due to electrostriction was measured for an acrylic tape specimen under equi-biaxial prestrain.

Finally the setup of the FSI simulations of a passive membrane and the setup of the electromechanical simulations of a Neo-Hookean hyperelastic dielectric elastomer have been joined together in order to predict the behaviour of an electroactive membrane wing. For validation purposes the structural characteristics of a hyperlastic electroactive membrane wing have been calculated in order to match the behaviour of the passive membrane simulated by Gordnier. This numerical setup will be used in the next chapters to study more in detail the behaviour of a fully and partially activated membrane wing.

Chapter 5

Electroactive membrane

The change in material properties due to electrostriction has been further simulated in this chapter in order to study its effect on the fluid-structure coupling. The whole surface of the membrane is activated in the simulations in Section 5.1 whereas the activation of only a portion along the chord has been considered in Section 5.2. In every case a prestrain $\lambda_{pre} = 3$ is applied before activating the membrane. The activation voltage (ϕ = 1,200 V) has been lowered by 15% compared to the previous simulation in order to simulate conditions where the sensitivity of the prestrain with respect to the voltage variation is smaller than 5% for a variation of 500 V. In fact for values of V $>$ 1,500 the gradient of the strain-voltage curve (Fig. 4.22) is too large meaning that the membrane is too sensitive to very small variations of voltage and therefore very difficult to control and not feasible for realistic applications.

5.1 Fully-activated membrane

The membrane displacement and the aerodynamic characteristics have been compared for angles of attack $\alpha = 12^\circ, 16^\circ, 20^\circ$ at Re = 2,500. When only the prestretch acts on the membrane, the midpoint displacement (red dashed lines in Fig. 5.1) is smaller than in the activated case. This is due to the effect of the Maxwell stresses which produce an in-plane relaxation. As

the membrane relaxes it opposes less resistance to the pressure difference generated by the flow resulting in an increased camber. Also, for a non-active membrane the amplitude of oscillations at different angles of attack remains of the same order of magnitude, whereas the activated membrane (black lines) exhibits an increasing amplitude of oscillations for increasing angles of attack.

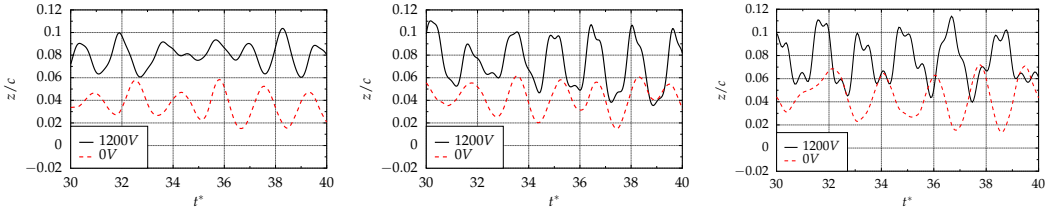

(a) $\alpha = 12°$. (b) $\alpha = 16°$. (c) $\alpha = 20°$.

Figure 5.1: Time history of the membrane midpoint displacement.

The flow patterns and the evolution of the vortices released at the trailing edge of the membrane are displayed for both cases and for each angle of attack in 4 snapshots of the vorticity field (Figs. 5.2, 5.3 and 5.4), starting from an arbitrary time $t = \bar{t}$ at intervals of 0.35 and 0.5 nondimensional time units t^*. These intervals allow to visually track the vortices that are shed from the leading and trailing edge.

When only the prestretch is applied the flow pattern at $\alpha = 12°$ (Fig. 5.2) reveals that the downwash angle is lower than the case with the membrane fully activated, i.e. the wake in the baseline case (Figs. 5.2.a2) points upward more than in the activated case (Figs. 5.2.a1). The downwash generated also gives us an indication about the lift generated by the membrane. In fact, according to the Kutta-Joukowski theorem the lift per unit span, L', is proportional to the air density, ρ, the free-stream velocity, U_∞, and the circulation, Γ, around the membrane

$$L' = \rho U_\infty \Gamma,$$

therefore the higher the downwash the more lift is produced by the membrane. This can be seen in Fig. 5.5 where the streamlines at $\alpha = 12°$ for

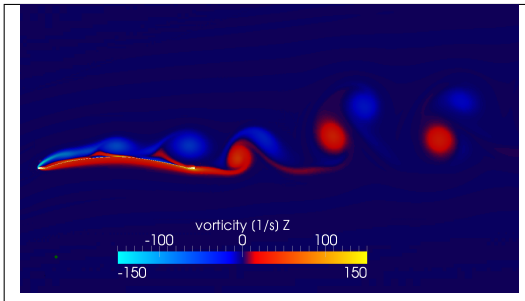

(a1) 1200 V

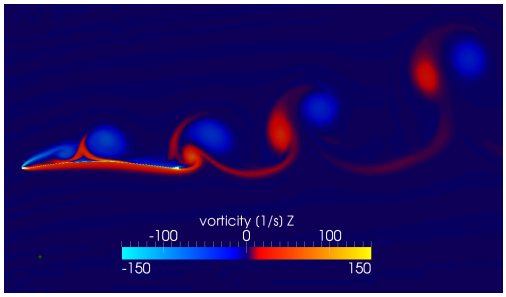

(a2) 0 V

(a) $t = \bar{t}$

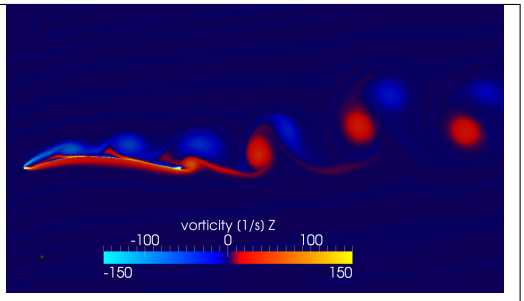

(b1) 1200 V

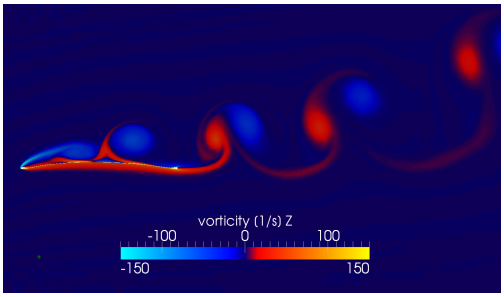

(b2) 0 V

(b) $t = \bar{t} + 0.35t^*$

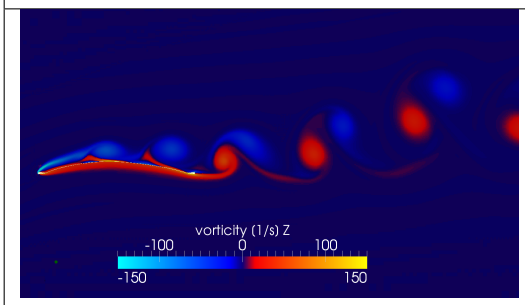

(c1) 1200 V

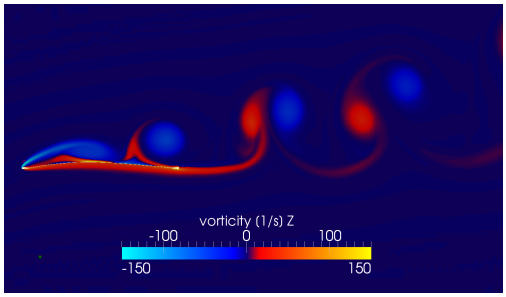

(c2) 0 V

(c) $t = \bar{t} + 0.7t^*$

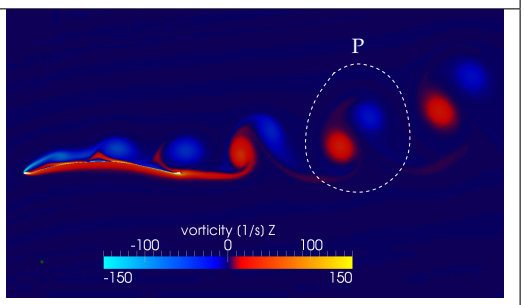

(d1) 1200 V

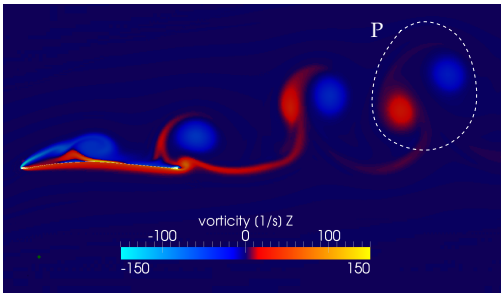

(d2) 0 V

(d) $t = \bar{t} + 1.05t^*$

Figure 5.2: Vorticity field at $\alpha = 12°$.

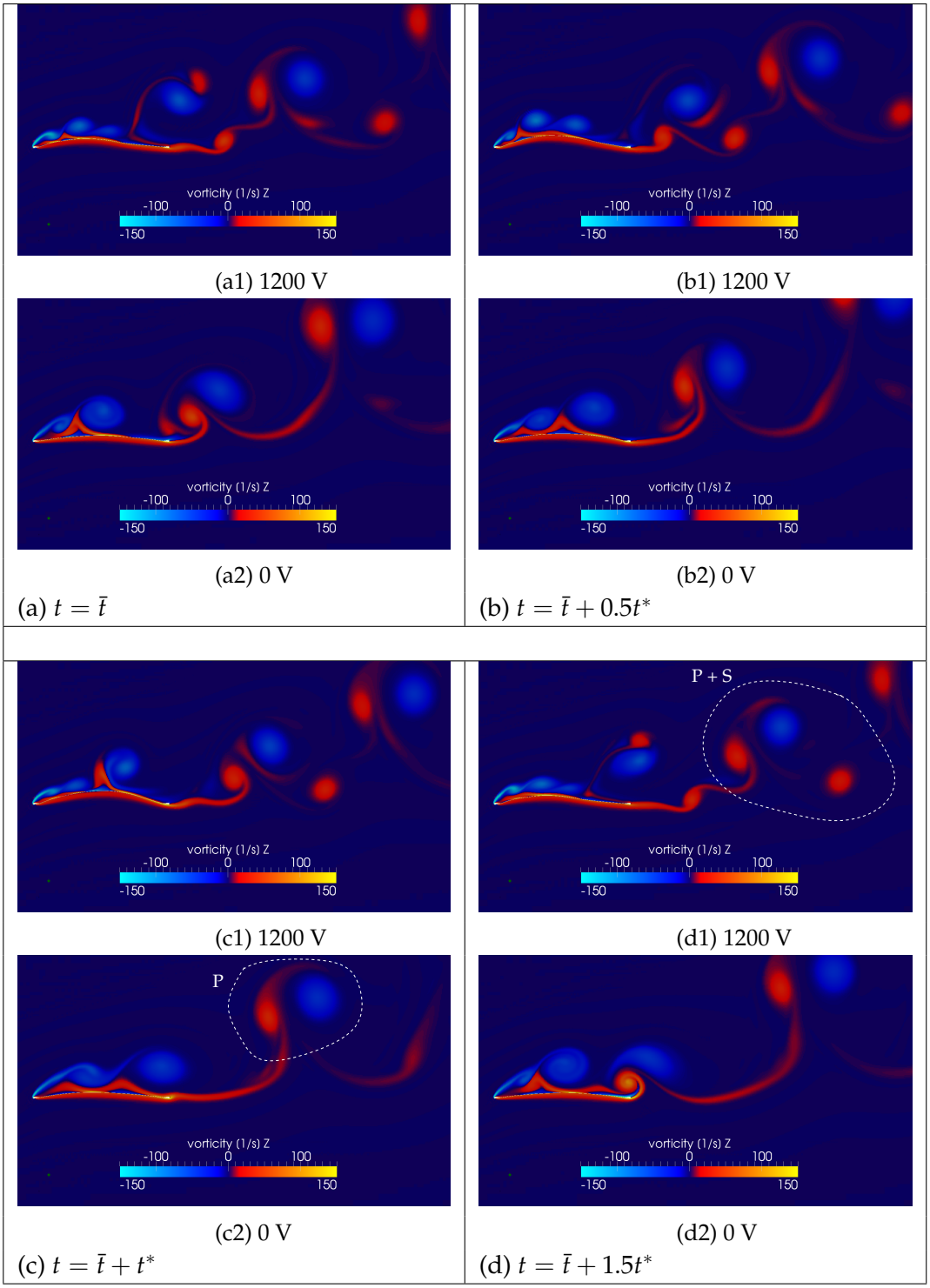

(a1) 1200 V

(b1) 1200 V

(a2) 0 V

(a) $t = \bar{t}$

(b2) 0 V

(b) $t = \bar{t} + 0.5t^*$

(c1) 1200 V

(d1) 1200 V

(c2) 0 V

(c) $t = \bar{t} + t^*$

(d2) 0 V

(d) $t = \bar{t} + 1.5t^*$

Figure 5.3: Vorticity field at $\alpha = 16°$.

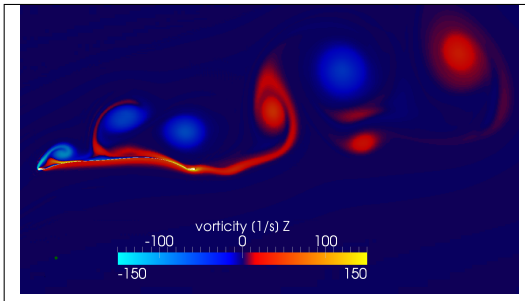

(a1) 1200 V

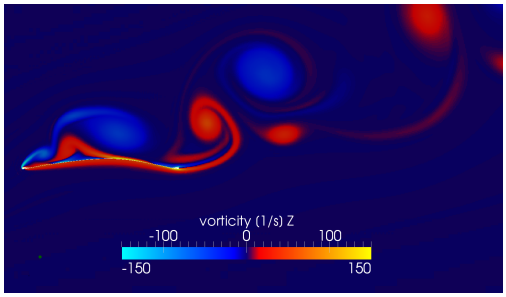

(a2) 0 V

(a) $t = \bar{t}$

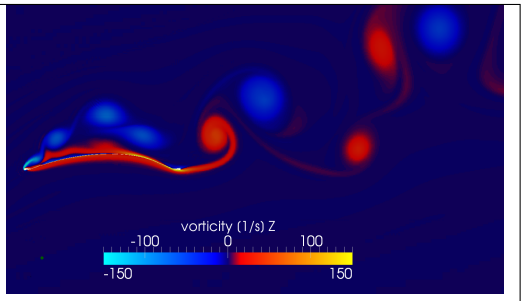

(b1) 1200 V

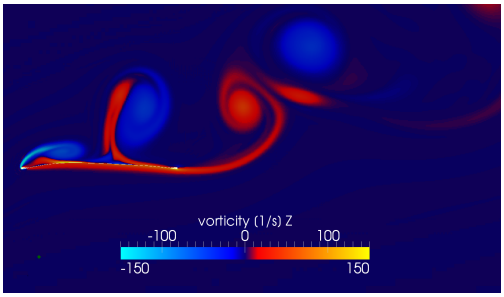

(b2) 0 V

(b) $t = \bar{t} + 0.5t^*$

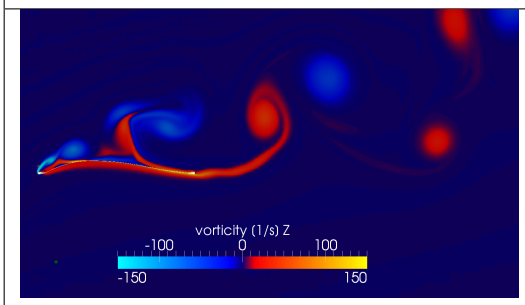

(c1) 1200 V

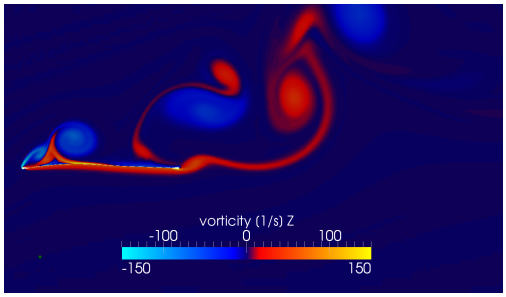

(c2) 0 V

(c) $t = \bar{t} + t^*$

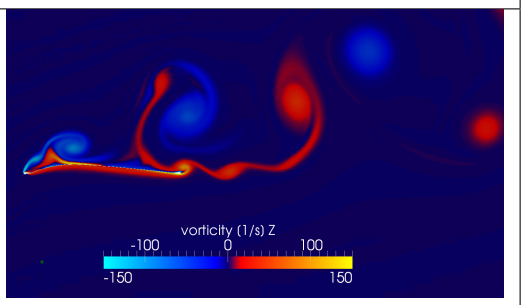

(d1) 1200 V

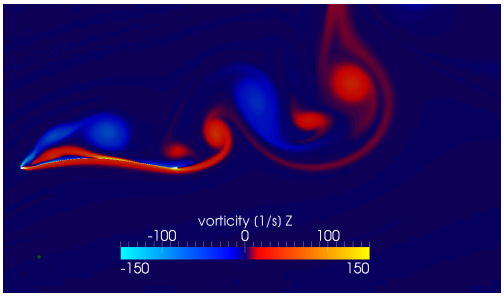

(d2) 0 V

(d) $t = \bar{t} + 1.5t^*$

Figure 5.4: Vorticity field at $\alpha = 20°$.

the fully activated membrane (1,200 V) and the non-activated one (0 V) are compared. The streamlines highlighted at the trailing edge of the membrane show the different angles of downwash generated by the two cases. The vertical component of velocity $\boldsymbol{u}_1$ at the trailing edge of the activated membrane is larger than the vertical component of the velocity $\boldsymbol{u}_2$ of the non-actived membrane. Therefore the circulation, defined as the line integral of the velocity on a closed curve around the membrane

$$\Gamma = \oint_C \boldsymbol{u} \cdot d\boldsymbol{l},$$

is larger for the activated membrane. According to the Kutta-Joukowski

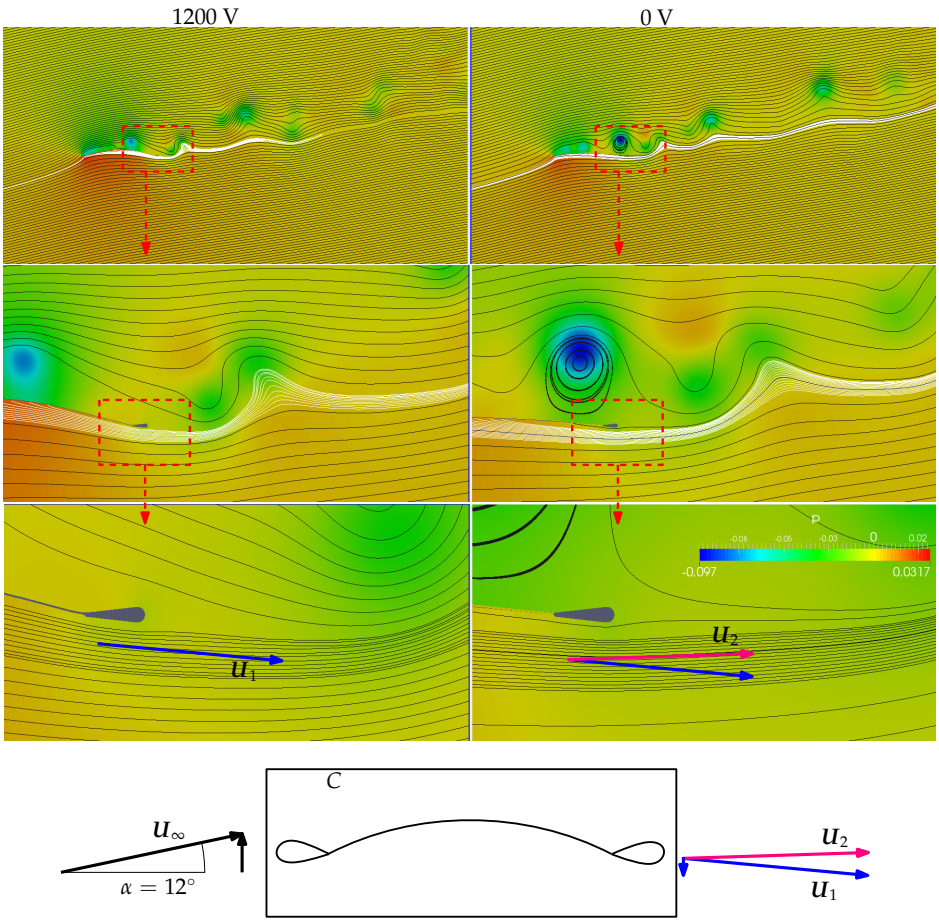

Figure 5.5: Streamlines comparison at $\alpha = 12°$.

theorem this is equivalent to a higher lift experienced by the activated membrane. In particular the increment in downwash is due to the increased camber of the membrane. In fact as the slope of the back part of the membrane increases, it forces the attached flow on the bottom of the trailing edge to point downwards (this is the same effect that a flap has on a fixed airfoil).

The higher camber of the activated case also helps keeping the flow at the leading edge to be more attached. At $\alpha = 16^\circ$ (Fig. 5.3) the increased camber of the activated case still keeps the flow attached to the membrane for longer even though the intensity of the leading edge vortices is bigger than in the case at $\alpha = 12^\circ$ (Figs. 5.2.a1 and 5.3.a1). At $\alpha = 16^\circ$ the leading edge vortices do not interact anymore with the ones generated at the trailing edge, unlike the non-active case (Figs. 5.3.a1 and 5.3.a2) and both the active and non-active case at $\alpha = 12^\circ$ (Figs. 5.2.a1 and 5.2.a2). The interaction between leading and trailing edge vortices leads to different vortex shedding patterns. Studies on oscillating cylinders by Williamson and Roshko [146] found a selection of vortex formation modes which were defined as "2S" indicating 2 single counter-rotating vortices shed per cycle, "2P" meaning 2 pairs of vortices per cycle, and the pattern comprising three vortices per cycle thus was termed "P+S" (Fig. 5.6).

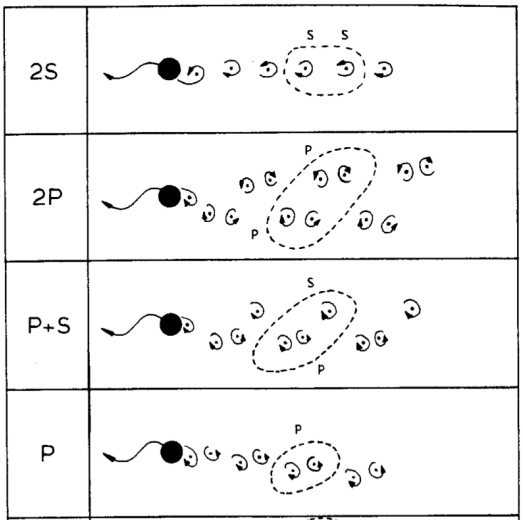

Figure 5.6: Vortex formation modes from Williamson and Roshko [146]

The same patterns are found here in the flow past the membrane. In particular at $\alpha = 12^\circ$ for the active and non-active membrane the vortices are shed in the "P" mode (Fig. 5.2), whereas at $\alpha = 16^\circ$ vortices are shed in the "P+S" mode for the active membrane and "P" mode for the non active (Fig. 5.3). At $\alpha = 20^\circ$ (Fig. 5.4) the high unsteadiness of the flow in both cases is mainly due to the detached eddies at the leading edge which do not follow the path of the trailing edge vortices, as it happened at lower angles of attack. In fact at $\alpha = 12^\circ$ the leading edge vortices travel downstream on top of the membrane and merge with the trailing edge vortices, whereas at $\alpha = 20^\circ$ the leading and trailing edge vortices do not merge.

The vortices released from the leading edge of a flexible membrane share some characteristics with those of oscillating rigid airfoils. In 1935 Theodorsen obtained the unsteady flow solution for small disturbances around a thin oscillating rigid airfoil in an inviscid and incompressible flow [129]. Because his theory was developed to handle purely sinusoidal maneuvres it is represented in the frequency domain. Theodorsen's model predicts the unsteady lift for a plunging and pitching airfoil as

$$C_L = \frac{\pi}{2}\left[\ddot{h} + \dot{\alpha} - \frac{a}{2}\ddot{\alpha}\right] + 2\pi\left[\alpha + \dot{h} + \frac{1}{2}\dot{\alpha}\left(\frac{1}{2} - a\right)\right] C(k),$$

where $\dot{h}$ and $\ddot{h}$ are the velocity and acceleration of the center of mass of the airfoil, respectively. α is the angle of attack, $\dot{\alpha}$ and $\ddot{\alpha}$ are the pitch velocity and acceleration, respectively. a is the pitch axis location with respect to the half chord and $C(k)$ is a transfer function relating sinusoidal input to their aerodynamic response. Even though in this thesis the membrane's simulations are at a fixed angle of attack and there is no plunging movement (i.e. the membrane's supports are fixed), the causes of the unsteady lift can be related with those of an oscillating rigid airfoil. In fact, the movement of the membrane induces a local change of incidence at the leading edge which could be compared to the the effect of $\dot{\alpha}$ and $\ddot{\alpha}$ for a rigid pitching airfoil. At the same time the change in camber is effectively a vertical movement of the center of mass of the membrane, $\dot{h}$. However,

Theodorsen's theory is valid only for small pitching and plunging movements. In fact, when the angular amplitudes are wide enough, the phenomenon of the dynamic stall occurs and there is no exact theory able to predict the aerodynamics [19]. Dynamic stall is a complicated aerodynamic phenomenon in which a vortex-like disturbance is shed by an airfoil at large angle of attack. The disturbance often originates near the leading edge and translates along the airfoil, resulting in a highly non-linear pressure disturbance. This nonlinearity causes the airloads to diverge significantly from those predicted by linear, thin-airfoil theory. There have been many semi-empirical models designed to quantify the effect of dynamic stall of fixed airfoils [85], whereas for flexible membranes the analysis of the dynamic stall can be made only by CFD and by experimental measurements.

Modifying the stiffness of the membrane via electrostriction is ultimately motivated by the possibility of evaluating how the aerodynamic characteristics can be improved. Therefore the lift and drag coefficients and lift-to-drag ratio have been analyzed for the same simulations. Their mean value, root mean square (RMS) and standards deviation (SD) are reported in Tab. 5.1. For every angle of attack the mean lift coefficient is higher for the activated membrane whereas the drag coefficient is lower. At $\alpha = 12^\circ$ lift and drag for the non-active membrane (red dashed line in Fig. 5.7) both oscillate with a larger amplitude and lower frequency compared with those of the activated case. Also, the difference between the

		Lift coefficient			Drag coefficient			Lift-to-drag ratio		
		mean	RMS	SD	mean	RMS	SD	mean	RMS	SD
$\alpha = 12^\circ$	1200 V	1.422	1.424	0.069	0.204	0.205	0.018	6.808	6.821	0.418
	0 V	1.287	1.345	0.388	0.247	0.259	0.075	5.216	5.240	0.504
$\alpha = 16^\circ$	1200 V	1.674	1.749	0.507	0.356	0.395	0.152	5.202	5.418	1.514
	0 V	1.516	1.568	0.397	0.399	0.415	0.111	3.816	3.823	0.221
$\alpha = 20^\circ$	1200 V	1.763	1.821	0.493	0.554	0.586	0.168	3.735	3.792	0.650
	0 V	1.703	1.772	0.458	0.570	0.594	0.155	2.989	3.01	0.228

Table 5.1: Force coefficients: mean, root mean square (RMS) and standard deviation (SD) at different angles of attack.

mean values of the force coefficients of the active and the non-active cases diminishes at higher angles of attack (Figs. 5.8 and 5.9).

At $\alpha = 16^\circ$ the standard deviation of the aerodynamic forces (Figs. 5.8a and 5.8b) in the activated case (black line) is 25% larger than in the non-activated one (red dashed line), whereas at $\alpha = 20^\circ$ (Figs. 5.9a and 5.9b) this difference decreases to less than 10%. However additional higher frequencies are present in the signal of the activated membrane (black line) at $\alpha = 20^\circ$ showing the effect of a highly unsteady flow.

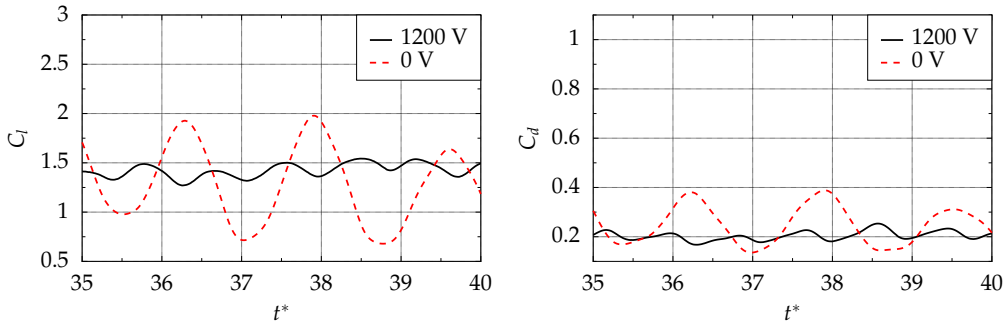

(a) Lift coefficient. (b) Drag coefficient.

Figure 5.7: Time history of the force coefficients at $\alpha = 12^\circ$.

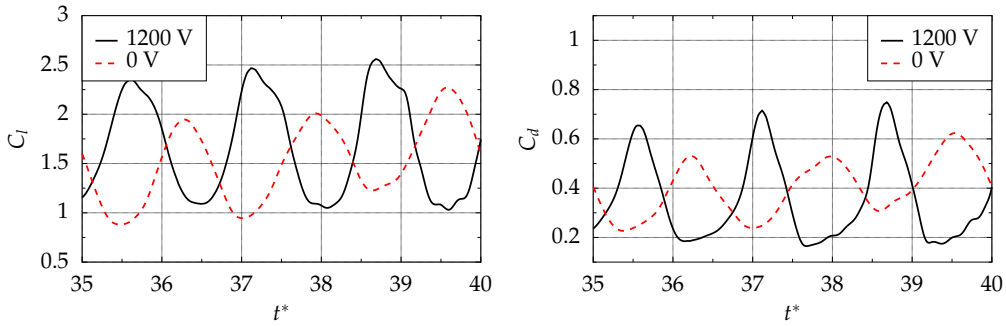

(a) Lift coefficient. (b) Drag coefficient.

Figure 5.8: Time history of the force coefficients at $\alpha = 16^\circ$.

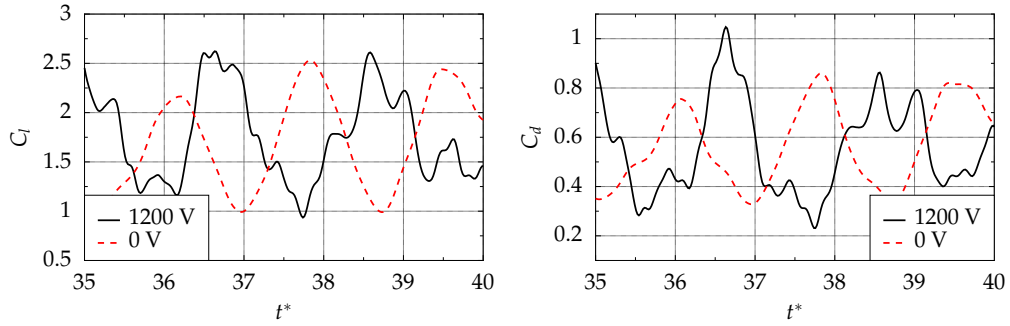

(a) Lift coefficient. (b) Drag coefficient.

Figure 5.9: Time history of the force coefficients at $\alpha = 20°$

If we now consider the lift-to-drag ratio C_l/C_d as indication of the aerodynamic efficiency of the membrane, we see that for every angle of attack (Tab. 5.1 and Fig. 5.10) the electroactive one (black line) performs better than the non-active (red dashed line). The mean value of the lift-to-drag ratio $\overline{C_l/C_d}$, decreases as the angle of attack increases. In particular, for the activated case (black line) it goes from $\overline{C_l/C_d} = 6.81$ at $\alpha = 12°$ down to $\overline{C_l/C_d} = 3.75$ at $\alpha = 20°$. Also, the improvement in the lift-to-drag ratio for the activated cases decreases as the angle of attack increases, i.e. the difference between $\overline{C_l/C_d}$ of the active and non-active case is higher at $\alpha = 12°$ ($\Delta\left(\overline{C_l/C_d}\right) = 1.4$) than at $\alpha = 20°$ ($\Delta\left(\overline{C_l/C_d}\right) = 0.74$).

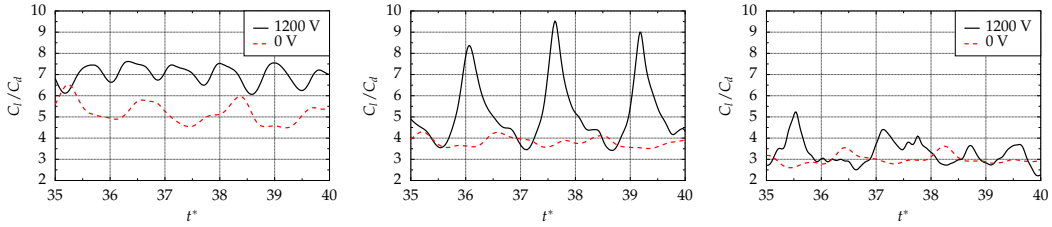

(a) $\alpha = 12°$. (b) $\alpha = 16°$. (c) $\alpha = 20°$.

Figure 5.10: Lift-to-drag ratio at different angles of attack.

On the one hand the electroactive membrane shows an improvement in the aerodynamic efficiency (the C_l/C_d peaks in the active case can even double the values of a non-active one) but on the other hand its oscillations would not be beneficial for the attitude control of a micro air vehicle

(MAV). Therefore some considerations on the dynamics of the interaction between the membrane and the flow can be useful to better understand how modifying the stiffness of the membrane via electrostriction might bring some aerodynamic benefits.

In order to do this, we analyse for the case at $\alpha = 20°$ the instantaneous

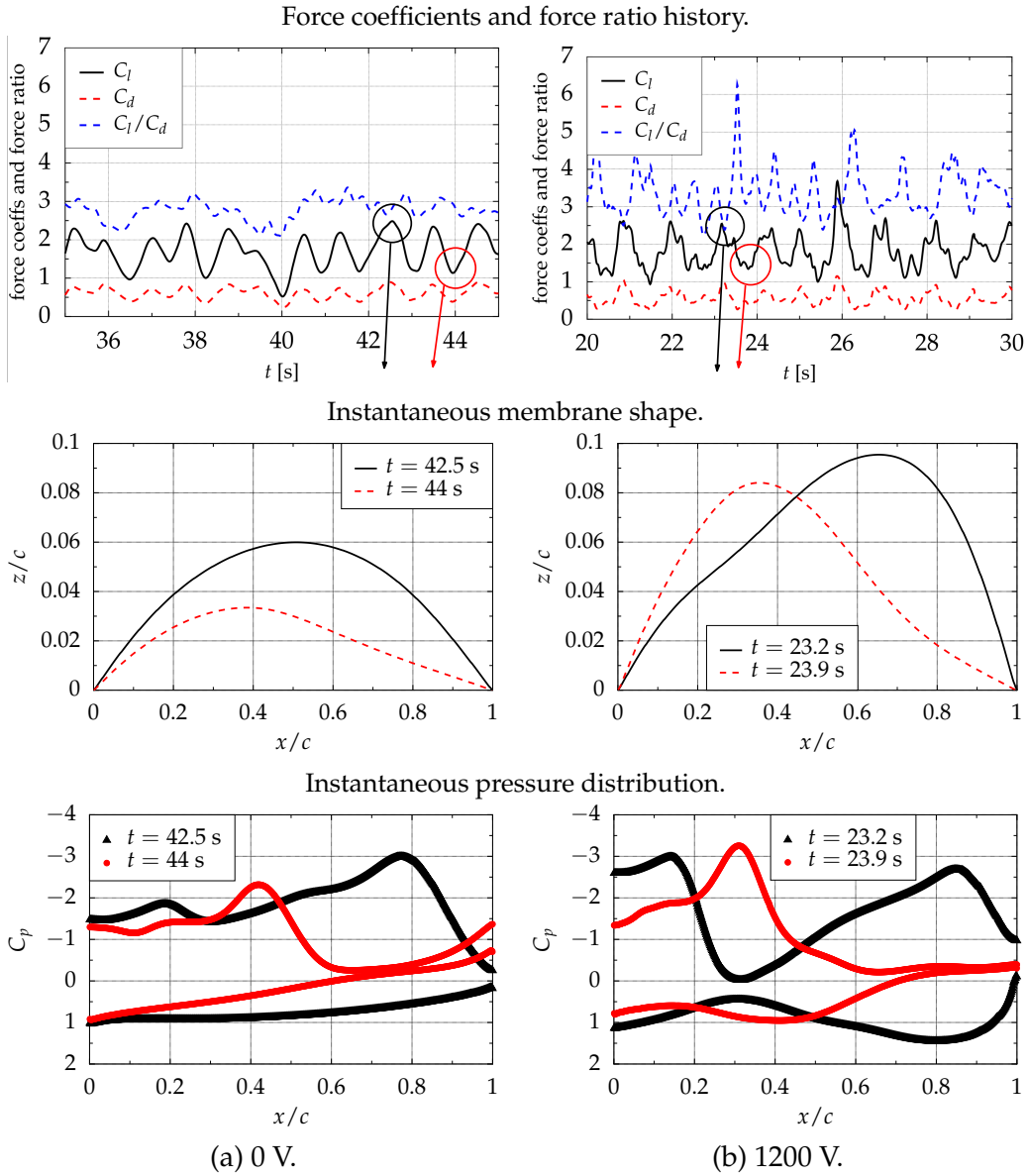

(a) 0 V. (b) 1200 V.

Figure 5.11: Correlation between membrane shape and local maximum/minimum peak in lift at $\alpha = 20°$.

shapes of the membrane and the associated pressure distribution when the lift coefficient reaches a local maximum and minimum, respectively. This is shown in Fig. 5.11 with the plots on the left and right columns relative to the non-activated membrane and the activated one, respectively. The instants which the shape of the membrane refers to are circled in the time history of the force coefficients in black for the local maximum in lift and red for the local minimum of lift. As expected the higher camber is associated with larger pressure difference across the whole length of the membrane and therefore higher lift. On the contrary when a local minimum of lift is reached, this is due mainly to the unload of the back portion of the membrane, i.e. the pressure difference between pressure and suction side of the membrane for $x/c > 0.6$ is negligible in both activated and non-activated case. The rise in camber and lift are strongly dependent on each other and the complex behaviour of the membrane is characterized by a continuous exchange of energy: the flow pressure exerts a force on the membrane which expands the camber of the membrane. As the membrane displaces it stores elastic potential energy until it reaches the maximum displacement. At this point there is a force unbalance between the pressure distribution and the elastic force of the membrane. This energy is released as membrane pushes against the flow and shrinks. As the pressure is constantly acting on the membrane while it oscillates, the lift opposes the motion of the membrane on its way down and stops it at its lowest camber.

The main difference between the activated and the non-activated case is given by the increased relaxation of the membrane due to electrostriction and for this reason not only the membrane reaches a higher camber but also a larger number of structural modes is excited, i.e. the shape of the membrane is wavier and so is the pressure distribution. The interaction with the flow is therefore more complex and this can be seen from the additional high frequencies present in the time history of the lift (top right graph in 5.11). However these modes are not excited at lower angles of attack ($\alpha \leq 16^\circ$, Figs. 5.7 and 5.8) and do not bring any benefit in terms of increasing the lift as in both cases (activated and non-activated)

C_l oscillates in the same range ($1 < C_l < 2.6$ in top graphs of Fig. 5.11).

It is also useful to understand in which conditions the maximum (and minimum) aerodynamic efficiency (C_l/C_d) can be obtained. Again, we analyse the shapes of the membrane when the lift-to-drag ratio reaches its local maximum and minimum, respectively. This is shown in Fig. 5.12 with

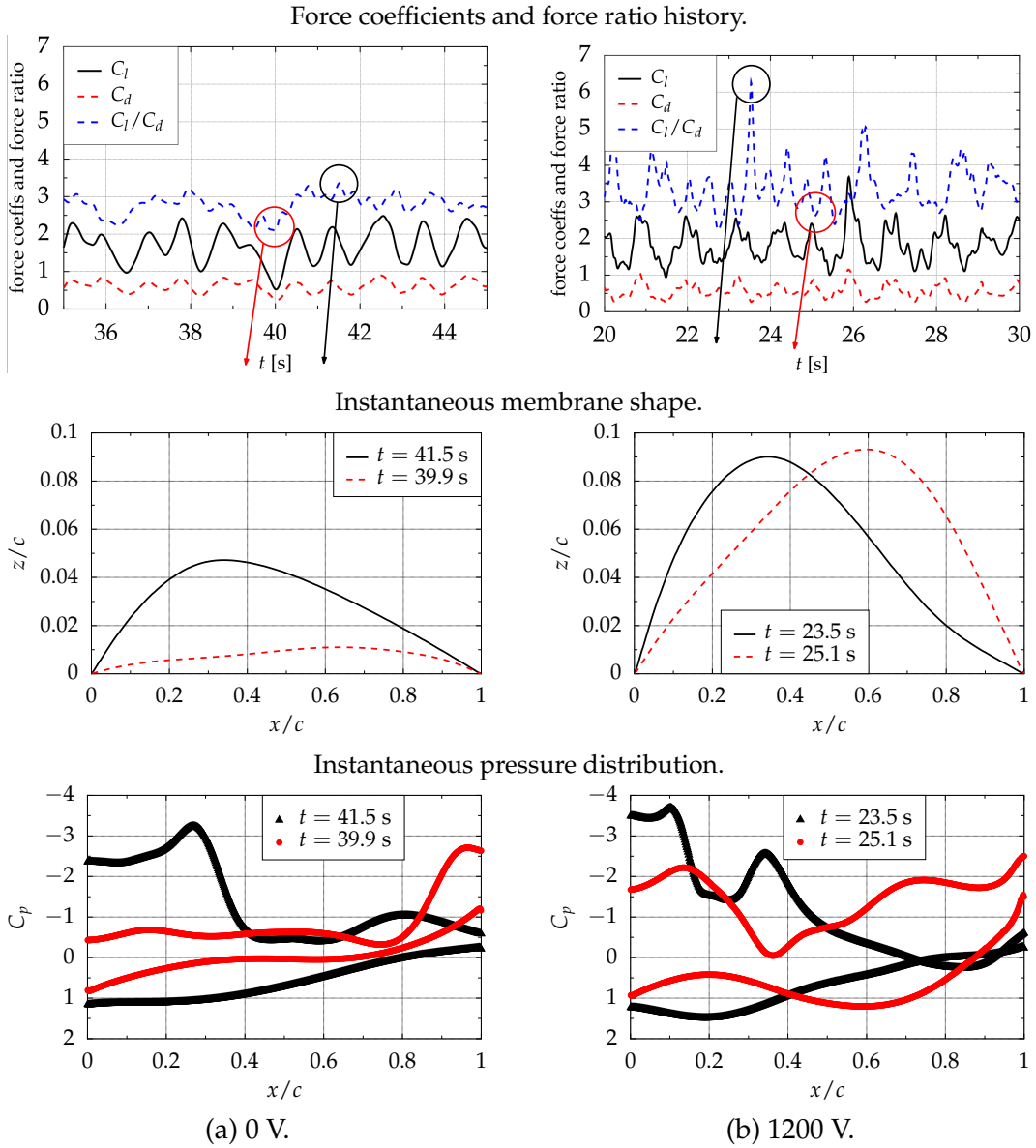

(a) 0 V. (b) 1200 V.

Figure 5.12: Correlation between membrane shape and local maximum/minimum peak in lift-to-drag ratio at $\alpha = 20°$.

the plots on the left and right columns corresponding to the non-activated membrane and the activated one, respectively. The instants which the shape of the membrane refers to are circled in the time history of the lift-to-drag ratio in black for the local maximum in lift-to-drag ratio and red for the local minimum of lift-to-drag ratio. In this case the feature associated with high (or low) lift-to-drag ratio is the position of the maximum displacement. In fact, for the activated and non-activated membrane the point of maximum displacement is at $x/c = 0.32$ whereas in condition of high lift it was further back ($x/c = 0.5$ for the non-activated membrane and $x/c = 0.68$ for the activated one). Since in the aerodynamic efficiency the information about the absolute value of lift and drag is lost, when C_l/C_d reaches its local maximum (or minimum) the lift and the drag will do not necessarily the same. When the point of maximum displacement is shifted towards the front (Fig. 5.12) there is also a higher pressure difference in the front part of the membrane. Here the component of pressure normal to the membrane points in the velocity direction and therefore the resultant force will have a component projected in the velocity direction as well which can be seen as a pressure contribution to the *thrust*. This explains the reduction in drag at this instant and therefore a higher value of C_l/C_d. The opposite happens when a higher pressure difference acts on the back of the membrane (red pressure distribution in Fig. 5.12).

As mentioned earlier there is not much difference in the maximum lift achievable by the activated and the non-activated one. In contrast, the maximum aerodynamic efficiency achievable by the membrane improves, going from $C_l/C_{d\max} = 3.4$ for the non-active one up to $C_l/C_{d\max} = 5-6$ for the active membrane. This effect can be better understood by comparing the shape of the membrane for the activated and the non-activated cases when they experience a high local peak in C_l/C_d (black membrane shapes in Fig. 5.12). We observe that the position of the maximum displacement is similar in both cases ($x/c = 0.32$). However, since the activated case has a higher camber, the pressure contribution to the thrust is enhanced not only by the larger pressure difference at the leading edge but also by two more factors:

1. the higher geometric slope of the membrane in the front section resulting in a higher projection of the resultant force in the velocity direction and

2. the larger area where the front pressure difference acts resulting in a higher absolute value of the resultant force.

It is worth mentioning that the opposite effect of decreasing C_l/C_d occurs when the point of maximum displacement is shifted backward is further reduced in the activated case. In fact, even if C_l/C_d for the active membrane varies in a larger range ($C_l/C_{d\max} - C_l/C_{d\min} = 2.5$ against $C_l/C_{d\max} - C_l/C_{d\min} = 1$ for the non-active case) this is mainly due to the enhancement of $C_l/C_{d\max}$ for the active case while the minimum value of C_l/C_d is never lower than the lowest one of the non-activated membrane (Fig. 5.10c). Again, this phenomenum can be explained by comparing the pressure distribution at a local minimum of C_l/C_d (red pressure distribution in Fig. 5.12): in the non-active case (Fig. 5.12a) the pressure difference in the back section of the membrane is higher than in the rest of the membrane and its projection in the velocity direction gives a higher contribution to the drag. On the contrary in the active case (Fig. 5.12a) a higher pressure difference is present also in the front section of the membrane canceling out the effect of the one in the back section.

These simulations have shown that the main benefit of a more relaxed membrane is the enhancement of the aerodynamic efficiency rather than the absolute value of the lift. The maximum efficiency depends on the membrane shape and it is achieved when the point of maximum displacement is shifted as much as possible towards the front. For this reason it would be useful also to investigate if activating only a section of the membrane can bring the same improvements or even more. This study is described in the next section.

5.2 Partially activated membrane

A voltage acting only on a portion of the membrane has also been simulated in order to test the solid solver's capability of dealing with boundary conditions for the electric potential on arbitrary locations of the membrane. More importantly it was intended to investigate whether the reduction in power consumption, obtained through the activation of a smaller part of the membrane, might still achieve the same improvements in aerodynamic performances and, if so, which activated part gives better results. Therefore the membrane's length has been divided arbitrarily into three equal parts and the same voltage of the case discussed in Section 5.1 (ϕ = 1,200 V) has been applied to the front, the middle and the back sections of the membrane, keeping the same solid characteristics of the previous simulations. The effect of the actuator applied to different parts of the membrane has been simulated in the same flow conditions as the previous simulations (Re = 2,500) and at high angles of attack ($\alpha = 8°, 12°, 20°$) for which the membrane develops an unsteady behaviour.

Shown in Fig. 5.13 is the comparison of the mean displacement for $\alpha = 8°, 20°$ where also an inactive membrane and an all active one have been included for reference. A membrane with actuation applied to the front (or back) section presents a shape whose maximum displacement point is shifted towards the front (or the back) because of the higher relaxation induced by the Maxwell stresses in the front (or in the back). When the

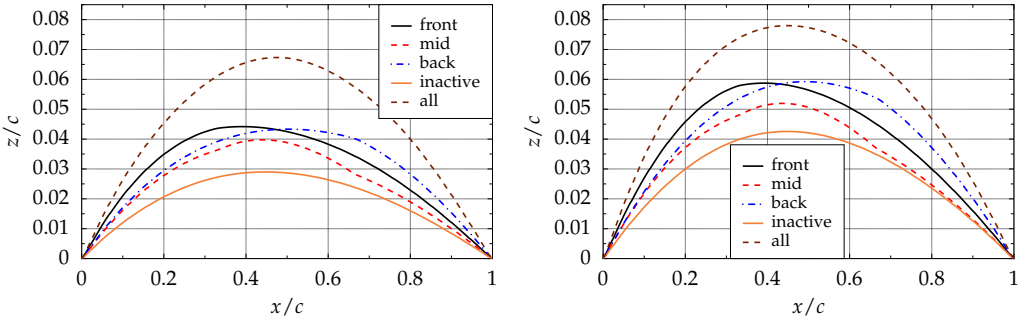

(a) $\alpha = 8°$. (b) $\alpha = 20°$.

Figure 5.13: Mean displacement.

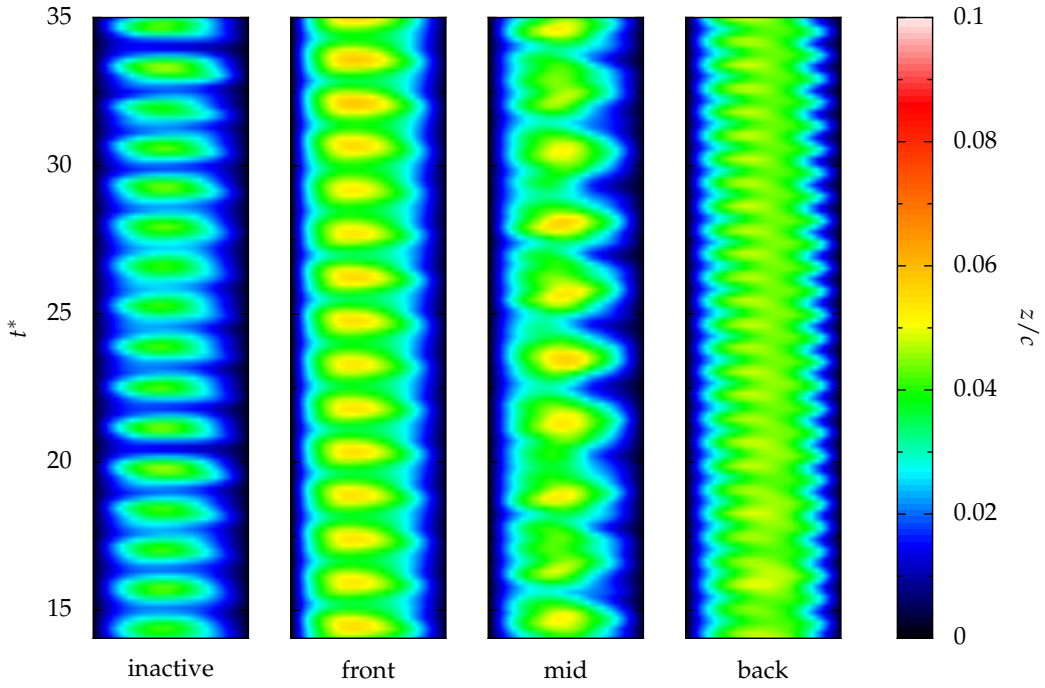

Figure 5.14: Displacement contours at $\alpha = 8°$.

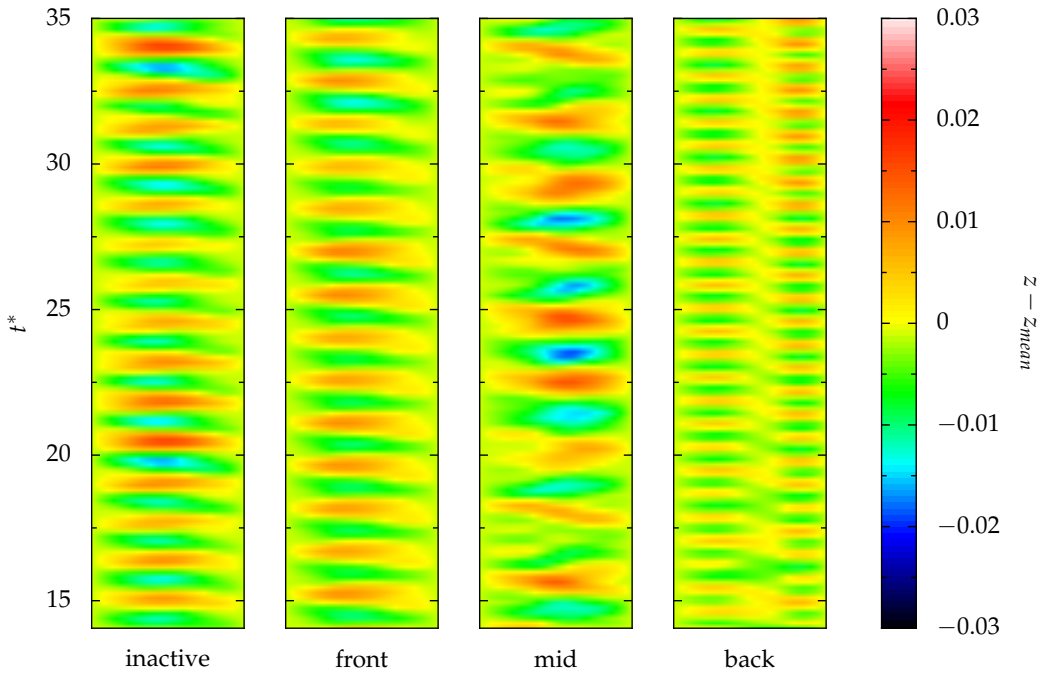

Figure 5.15: Perturbation around the mean displacement at $\alpha = 8°$.

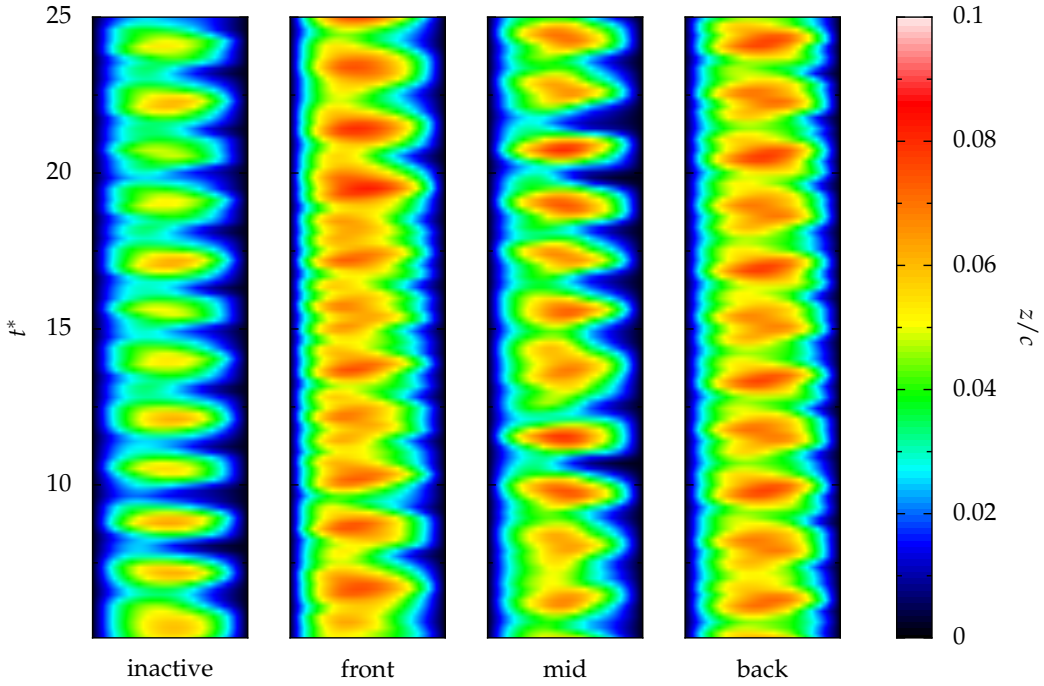

(a) $\alpha = 12°$

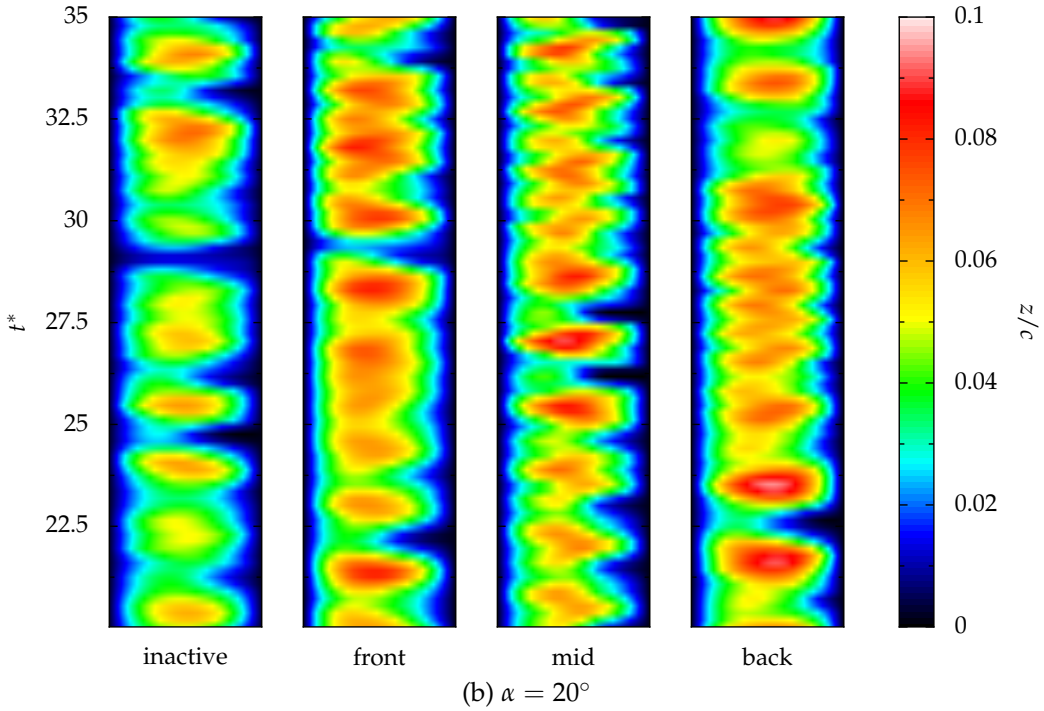

(b) $\alpha = 20°$

Figure 5.16: Displacement contours at high angles of attack.

middle section is actuated the membrane develops a bump in the central part and the maximum displacement is always smaller than in the cases with actuators in the front or back sections whose maximum displacements are similar.

The comparison between the contours of the displacement history of the membrane at $\alpha = 8°$ (Fig. 5.14) shows very different behaviours depending on the location of the actuator. The inactive membrane presents a first mode standing wave as does as the membrane with a front actuator. In the latter case the amplitude is larger and the maximum displacement point is shifted towards the front. When the actuator in is the middle section the membrane responds more irregularly to the flow and when it is in the back section the membrane develops a second mode standing wave which can be identified in the contours of the perturbation around the mean (Fig. 5.15). More unsteadiness is introduced into the system as the angle of attack increases. In fact for $\alpha \geq 12°$when the membrane is activa-

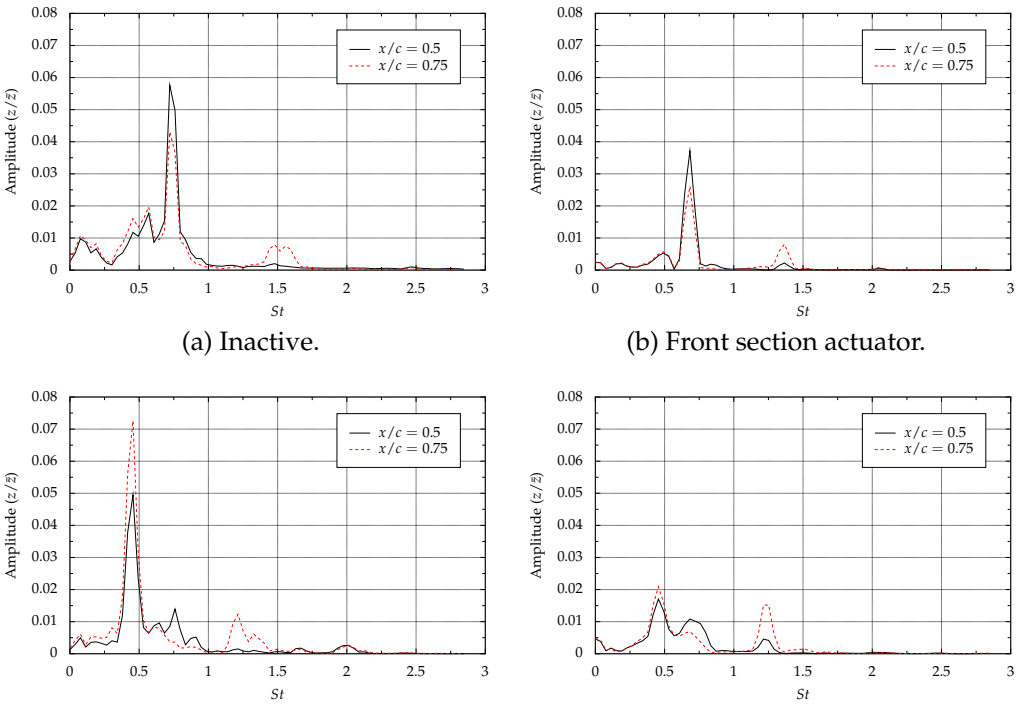

(a) Inactive.

(b) Front section actuator.

(c) Middle section actuator.

(d) Back section actuator.

Figure 5.17: Structural spectra of the displacement around the mean at $\alpha = 8°$.

ted on the back section, the second structural mode cannot be distinguished anymore (Fig. 5.16) and the differences between the behaviours of the three different cases are attenuated.

From the spectra of the perturbations around the mean obtained at two points along the membrane ($x = 0.5c$ and $x = 0.75c$) shown in Fig. 5.17, it is possible to see how the front and back section actuators damp the oscillation of the membrane (only for the back section actuator at $x = 0.75c$ the amplitude of the peak at high frequency is amplified because at that point the membrane is more relaxed). In contrast, the mid-section actuator tends to amplify the amplitude of oscillations of the membrane (Fig. 5.17c). On the one hand this behaviour is not be beneficial in a steady flight condition but on the other hand this strong response might be exploited to obtain more control authority in unsteady manouvers. At higher angles of attack the mid-section actuator again amplifies the unsteadiness of the membrane, unlike the front or back section actuators whose peaks are lo-

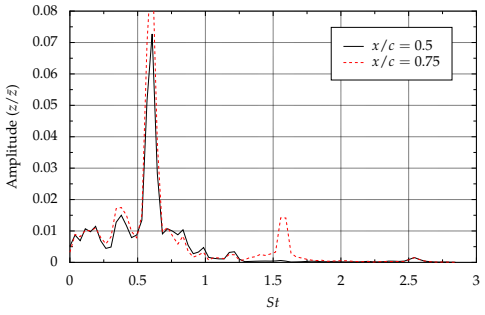

(a) Inactive.

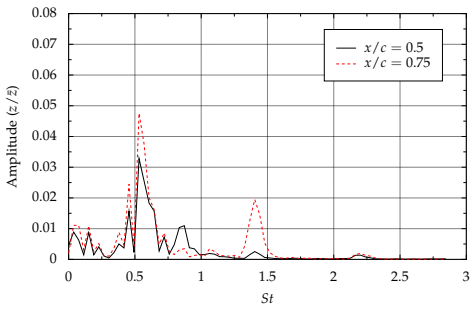

(b) Front section actuator.

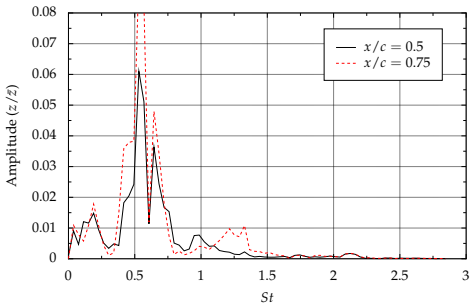

(c) Middle section actuator.

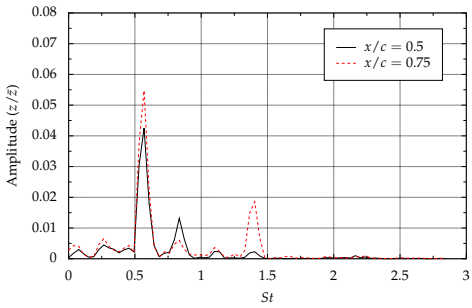

(d) Back section actuator.

Figure 5.18: Structural spectra of the displacement around the mean at $\alpha = 12°$.

wer or equal to the inactive case, as can be seen from the spectra of the structural response at $\alpha = 12°$ in Fig. 5.18 and at $\alpha = 20°$ in Fig. 5.19. Also, looking at the time history of the force coefficients at $\alpha = 8°$ (Fig. 5.20), the lift and the drag of the membrane with a mid-section actuator present high amplitudes of oscillations (black line), whereas the amplitude is smaller for a front and back section actuator. Furthermore, the aerodynamic efficiency (Fig. 5.20c) of a back actuated membrane has a mean value ($\overline{C_l/C_d} = 9.1$) slightly larger than the one of a front actuated membrane ($\overline{C_l/C_d} = 8.9$) but with higher amplitude of oscillation. Unlike the case at $\alpha = 8°$, the force coefficients at $\alpha = 12°$ (Fig. 5.21) for a mid-section actuated membrane have similar amplitude, frequency and mean value of a front or back section actuated one. Increasing the angle of attack to $\alpha = 20°$ the actuation on the back section allows to reach peak values of C_l 50% higher than activating the membrane in the middle or in the front (Fig. 5.22a). Presented in Tab. 5.2 are the mean force coefficients and lift-

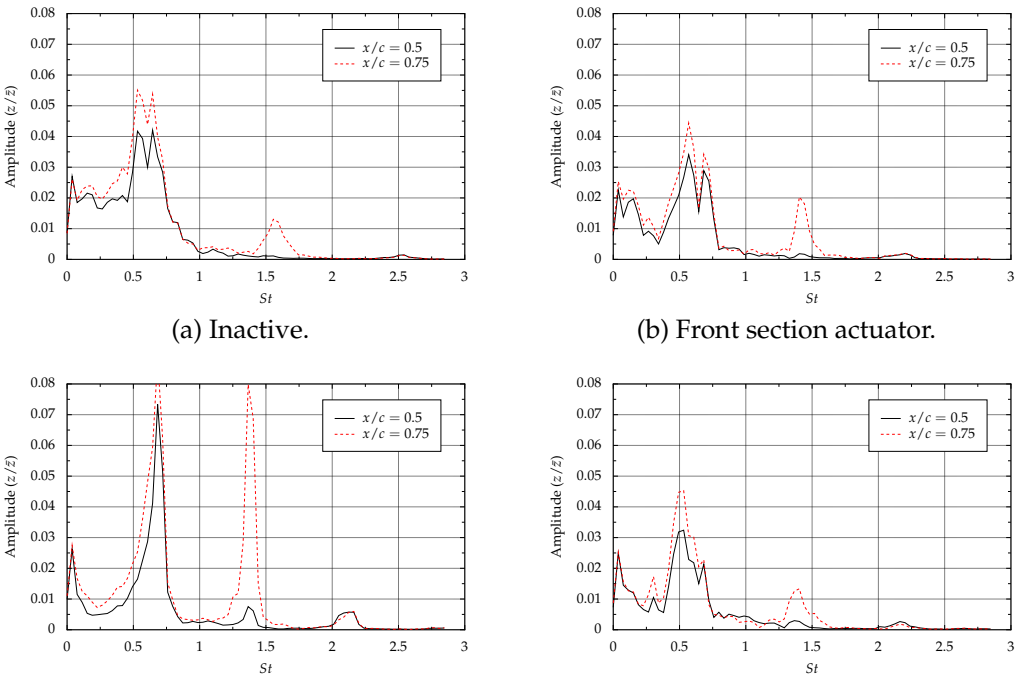

(a) Inactive.

(b) Front section actuator.

(c) Middle section actuator.

(d) Back section actuator.

Figure 5.19: Structural spectra of the displacement around the mean at $\alpha = 20°$.

to-drag ratio along with their root mean square (RMS) and standard deviation (SD). Between the three configurations the one that shows the highest mean lift coefficient at all the angles of attack tested is the membrane with a back section actuation. However at $\alpha = 20°$ its mean lift coefficient is lower than the one generated by a fully-activated membrane. In terms of mean drag reduction there is no advantage in a partial activation of the membrane as at $\alpha = 8°$ and $\alpha = 12°$ the lowest mean drag coefficient is

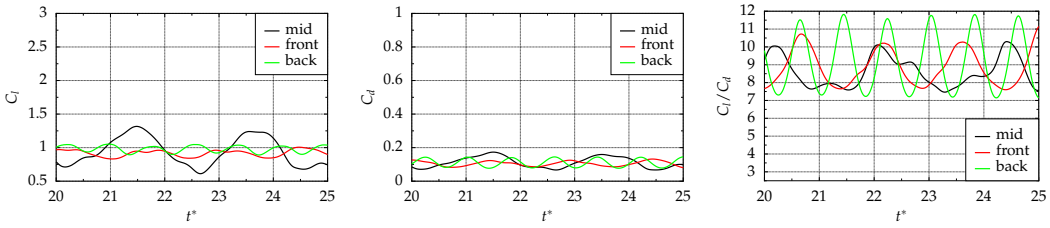

(a) Lift. (b) Drag. (c) Lift-to-drag ratio.

Figure 5.20: Force coefficients and force ratio at $\alpha = 8°$.

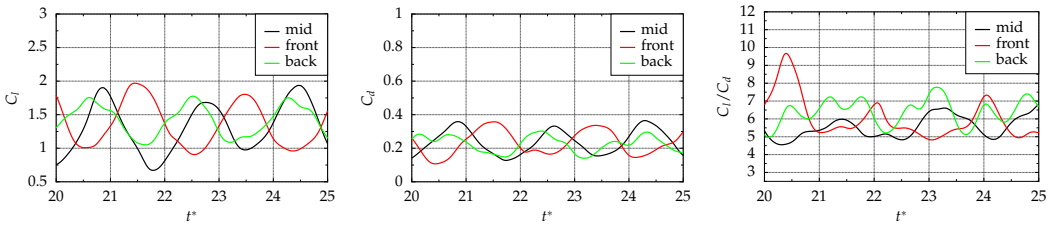

(a) Lift. (b) Drag. (c) Lift/Drag ratio

Figure 5.21: Force coefficients and force ratio at $\alpha = 12°$.

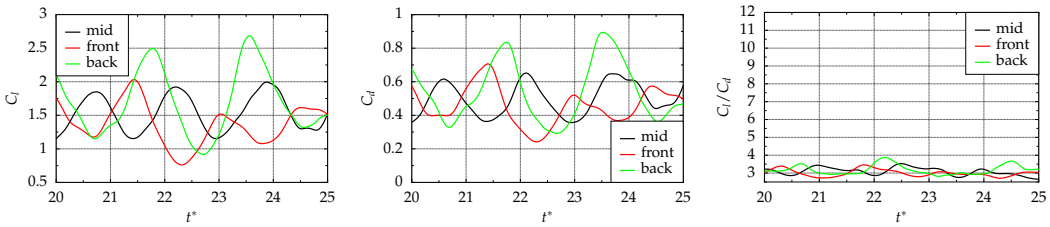

(a) Lift. (b) Drag. (c) Lift/Drag ratio

Figure 5.22: Force coefficients and force ratio at $\alpha = 20°$.

achieved by a fully activated membrane. Only at $\alpha = 20^\circ$ a front activated shows a mean drag coefficient lower than the one of a fully activated membrane. The small amplitude of oscillation of a front and back section activated membrane at low angles of attack make them good candidates for real applications unlike a mid-section activated membrane whose larger amplitudes would make the attitude control of a micro air vehicle more difficult. Moreover, the aerodynamic behaviour at low angles of attack ($\alpha = 8^\circ$) which allows to increase the lift of a membrane activated on the back section more than one activated on the front can be better understood looking at their vorticity fields in Fig. 5.23. The instant taken in consideration corresponds to the time when both membranes experience a maximum lift to drag ratio. Both membranes have a similar maximum camber (Fig. 5.23d). However, the back activated membrane (Fig. 5.23b) oscillating in its second structural mode releases vortices from the leading

		Lift coefficient			Drag coefficient			Lift-to-drag ratio		
		mean	RMS	SD	mean	RMS	SD	mean	RMS	SD
$\alpha = 8^\circ$	mid	0.942	0.966	0.213	0.112	0.116	0.033	8.622	8.665	0.864
	front	0.917	0.918	0.048	0.104	0.105	0.014	8.891	8.921	0.980
	back	**0.981**	0.982	0.048	0.110	0.112	0.022	9.184	9.316	1.563
	all	0.917	0.918	0.044	**0.100**	0.101	0.010	**9.240**	9.275	0.805
	inactive	0.870	0.875	0.097	0.114	0.115	0.017	7.708	7.757	0.869
$\alpha = 12^\circ$	mid	1.320	1.370	0.364	0.241	0.252	0.071	5.518	5.550	0.600
	front	1.339	1.378	0.324	0.230	0.241	0.072	6.050	6.162	1.168
	back	**1.428**	1.445	0.221	0.226	0.231	0.047	6.407	6.446	0.712
	all	1.422	1.424	0.069	**0.204**	0.205	0.018	**6.808**	6.821	0.418
	inactive	1.287	1.345	0.388	0.247	0.259	0.075	5.216	5.240	0.504
$\alpha = 20^\circ$	mid	1.534	1.556	0.263	0.498	0.507	0.093	3.095	3.102	0.212
	front	1.360	1.393	0.299	**0.456**	0.469	0.110	3.002	3.008	0.195
	back	1.684	1.752	0.484	0.537	0.566	0.177	3.181	3.193	0.269
	all	**1.763**	1.821	0.493	0.554	0.586	0.168	**3.735**	3.792	0.650
	inactive	1.703	1.772	0.458	0.570	0.594	0.155	2.989	3.01	0.228

Table 5.2: Force coefficients and lift-to-drag ratio: mean, root mean square (RMS) and standard deviation (SD) at different angles of attack. (in bold: the highest lift coefficient and lift-to-drag ratio and the lowest drag coefficient).

edge at a faster rate. Therefore for a back section activated membrane two vortices travel downstream instead of a single one as is the case of a front activated membrane (Fig. 5.23c). The two vortices on the suction side of the membrane are low pressure zones (peaks in the pressure distribution in 5.23d) which increase the overall lift of the membrane. Moreover, the first low pressure peak on the suction side of the back section activated membrane acts in the front portion of the membrane where the local curvature is negative. This translates in a higher projection of the pressure force in the direction of motion and therefore a reduction in drag.

5.3 Summary

In this chapter the mechanical characteristics of the membrane have been modified by means of electrostriction and its relative fluid-structure coupling has been analysed. In Section 5.1 a constant voltage across the whole membrane has been applied to a prestretched membrane and its aerodynamic performances have been compared with those of a only prestretched one. As consequence of electrostriction producing an in-plane relaxation of the membrane, the mean camber of an activated membrane is larger than a non-activated one. Also, it has been shown that for an activated membrane the mean lift coefficient is larger than that of a non-activate one whereas the mean drag coefficient is smaller. However the difference between force coefficients of an activated and non-activated membrane decreases for increasing angles of attack due to the increasing level of unsteadiness of the fluid-structure coupling. Moreover, the analysis of the instantaneous shape of the membrane when it experiences a local maximum of lift-to-drag ratio revealed that high aerodynamic efficiency is achieved when the point of maximum displacement is shifted towards the front.

In order to verify if this condition could be achieved by a different way of applying the voltage across the membrane, a partial activation has been simulated in Section 5.2. The membrane has been divided chordwise in

three equal parts and a fixed voltage was applied only to the front, the mid or the rear part of the membrane. Even though the point of maximum displacement was shifted towards the front more for a front activated membrane, the configuration which showed the best aerodynamic performance was the membrane activated on the rear part. Especially at low angles of attack this is due to the particular way the vortices are shed from the leading edge. In fact at $\alpha = 8^{\circ}$ a membrane activated on the rear oscillates in its second structural mode at a higher frequency than the other configurations. This translates in a higher shedding frequency from the leading edge and more vortices (low pressure zone) travelling downstream on top of the membrane which increase the overall lift.

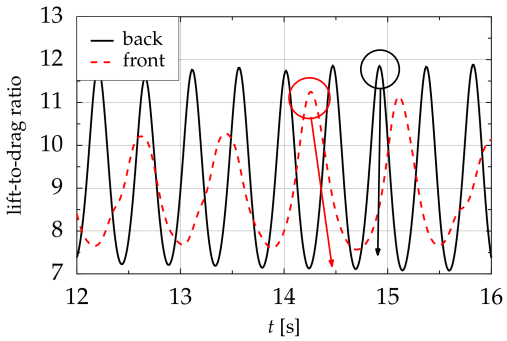

(a) Lift-to-drag ratio history.

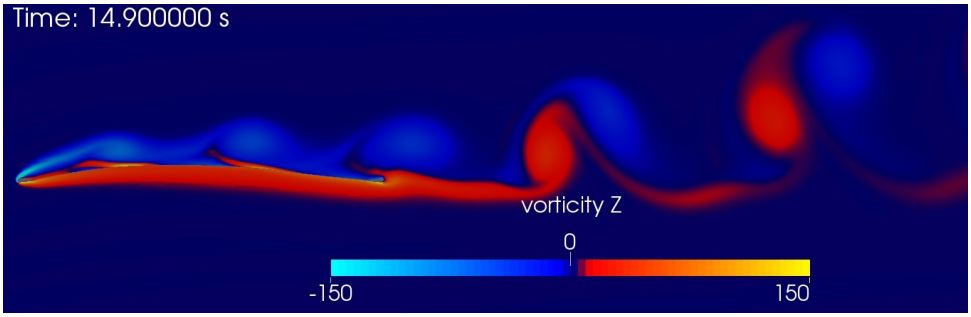

(b) Back activated membrane.

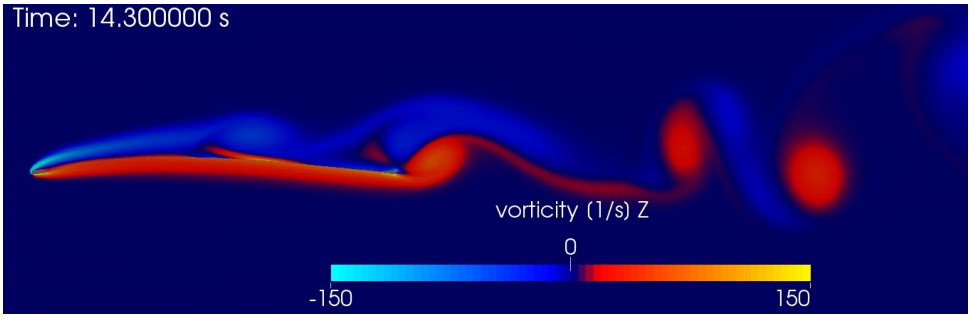

(c) Front activated membrane.

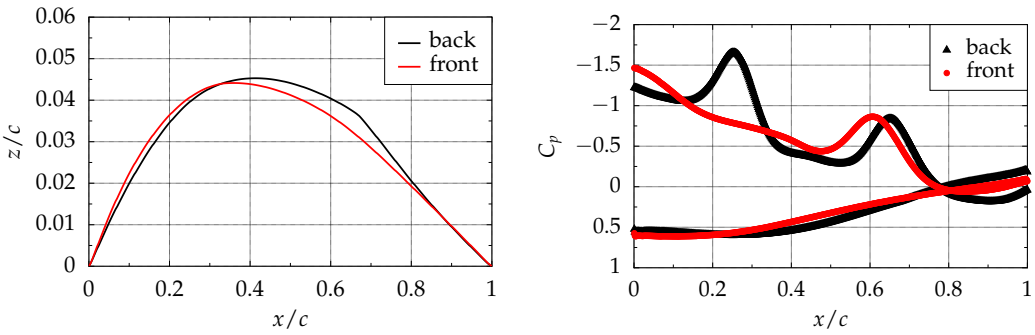

(d) Membrane shape and pressure distribution.

Figure 5.23: Comparison between front and back section activated membrane at high lift-to-drag ratio at $\alpha = 8°$.

Chapter 6

Control of the electroactive membrane

In the previous chapter we have seen how a fixed voltage allows to relax the membrane and therefore increase the camber and the mean lift. In a recent experiment Curet et al. [31] showed that the aerodynamic performance of a membrane wing with variable compliance can be enhanced even more applying a sinusoidal voltage at different frequencies. In his experiments the membrane was flying in a turbulent flow at $Re = 80{,}000$ and the forcing frequency was given in terms of the reduced frequency $k = 2\pi fc/U$, where c is the chord and U is the freestream velocity. Even though the experimental parameters of Curet (3D membrane in a turbulent flow) are different from those presented in this thesis, simulations with a varying voltage have been extended to the current FSI setup (Section 6.1) for the following reasons:

1. gradually increase the complexity of the current FSI solver and verify its robustness in dealing with varying voltages,

2. verify whether the experimental findings of Curet [31] apply also to a membrane in a laminar flow.

As showed in the previous chapter a membrane wing flying at high angles of attack experiences high amplitude oscillations which are not ideal

in operating conditions. A varying voltage might be used also to counteract the effects of the unsteady fluid-structure coupling. A first attempt to reduce the amplitude of oscillations with an open loop control is done in Section 6.1.1. However, the real potential of a dielectric elastomer is to exploit its electromechanic characteristics in order to use the membrane itself as a sensor. Therefore the varying voltage can be controlled in response to the unsteadiness of the flow-structure coupling in order to deliver a more stable flight. These simulations are presented in Sections 6.2.1 and 6.2.2.

6.1 Open Loop Control

Further simulations have been conducted with a dynamic change of the voltage applied across the membrane. The voltage was oscillating around an offset value of 600 Volts with the following sinusoidal law

$$V = A \sin(2\pi f t) + 600,$$

where A is the amplitude of the oscillations and the frequency f is given in terms of the reduced frequency, $k = 2\pi f c/U$. For these simulations the reduced frequency of the forcing voltage has been varied between $0.5 \leq k \leq 4$ and the amplitude assumed the values of 50, 100 and 300 Volts. Simulations have been performed at 4 angles of attack $\alpha = [8^\circ, 12^\circ, 16^\circ, 20^\circ]$.

When only a fixed voltage is applied ($k = 0$) the membrane responds oscillating at a frequency which increases for increasing angles of attack, going from $k = 3$ at $\alpha = 8^\circ$ to $k = 4.5$ at $\alpha = 20^\circ$ as shown in Fig. 6.1 where the spectra of the membrane's midpoint displacement and pressure are reported showing high correlation between them. The increasing frequency with the angle of attack can be justified by the rise of the aerodynamic load experienced by the membrane at increasing angles of attack. In fact, as the lift increases the membrane stretches, increasing the tension and therefore increasing the fundamental frequency.

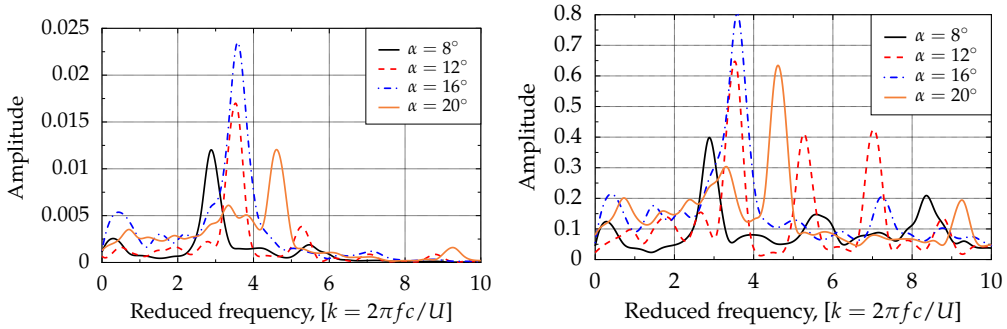

(a) Structure. (b) Pressure.

Figure 6.1: Structural and pressure spectra for $k = 0$.

As long as the electric field oscillates at a low frequency much smaller than the structural one, the membrane is forced to oscillate with an additional frequency whose amplitude is proportional to the input amplitude, A. This is visible from the spectra of the midchord displacement in Fig. 6.2a for a membrane at $\alpha = 16°$ forced with an oscillating voltage at $k = 2$ with different values of input amplitude, A. In this condition (i.e. when the structural and the forcing frequency are separated) the effect of the electro-structural coupling on the vortex shedding frequency is negligible as can be seen in the pressure coefficient spectra reported in Fig. 6.2b.

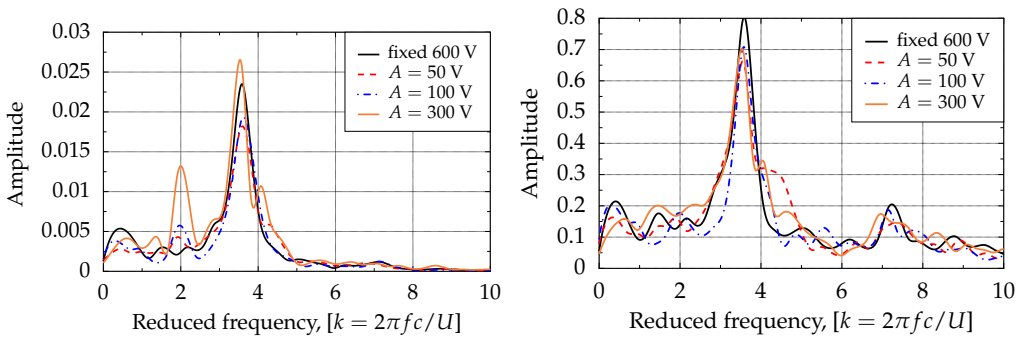

(a) Structure. (b) Pressure.

Figure 6.2: Spectra for $\alpha = 16°$ and $k = 2$.

Also, for a fixed input amplitude, A, the response frequency of the membrane is as the same as the forcing one (Fig. 6.3). However, the

response amplitude increases as the forcing frequencies approaches the natural frequency of the fluid-structure system. The largest amplitude is reached when the forcing frequency matches the natural one and the system is in resonance. The resonance frequency depends on the angle of attack as shown in Fig. 6.3 where it assumes the value of $k = 3$ and $k = 3.5$ at $\alpha = 8°$ and $\alpha = 16°$, respectively.

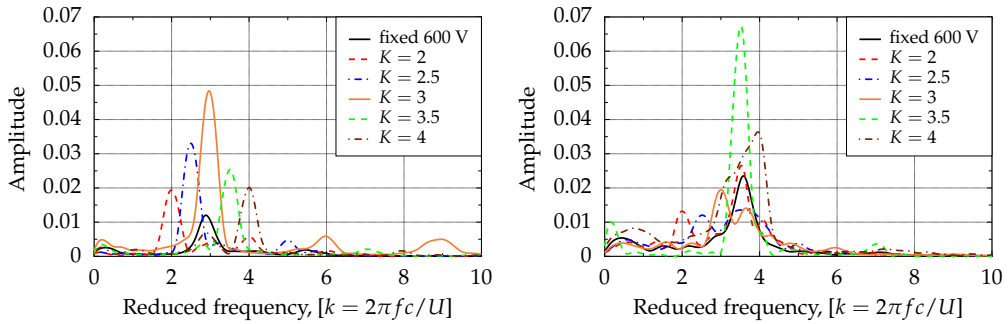

(a) $\alpha = 8°$. (b) $\alpha = 16°$.

Figure 6.3: Structure spectra for different k and $A = 300$ V.

It is worth noting that when the input amplitude is high ($A = 300$ V) and the forcing frequency is very close to the structural frequency, the whole system (structure and vortex shedding) oscillates at the forcing frequency. This is shown for the case at $\alpha = 12°$ in Fig. 6.4. At this angle of attack the system without a sinusoidal electric field oscillates at $k = 3.5$ (black line) and with forcing frequencies up to $k = 2.5$, a peak at $k = 3.5$ is still present in both structural and pressure spectra (red dashed line). However, when the system is excited either at $k = 3$ or at $k = 4$ the structure and the pressure field do not oscillate at $k = 3.5$ anymore but at the new forcing frequency (blue dotted dash and solid orange line).

This phenomenon is known in fluid dynamics as frequency lock-in [12] and it has been extensively investigated in many flow conditions. In the context of low Reynolds number flows, experiments and numerical simulations have been carried out for vortex-induced vibrations of rigid cylinders [16], plunging airfoils [151] and flapping wings [130]. The lock-in is defined as the local synchronization between the vortex shedding fre-

quency and the structural vibration frequency where the risonance may occur in a larger range of frequencies. For the cases analysed in this thesis this is believed to be the first simulated example of frequency lock-in for the fluid-structure interaction of an electroactive membrane wing. In fact in the studies available in literature the excitation of the vortex shedding is produced by the rigid motion of the airfoil whereas in the present work the excitation does not come from a prescribed motion but it is due to the secondary effect of the periodic relaxation/stiffening of the membrane induced by the oscillating voltage.

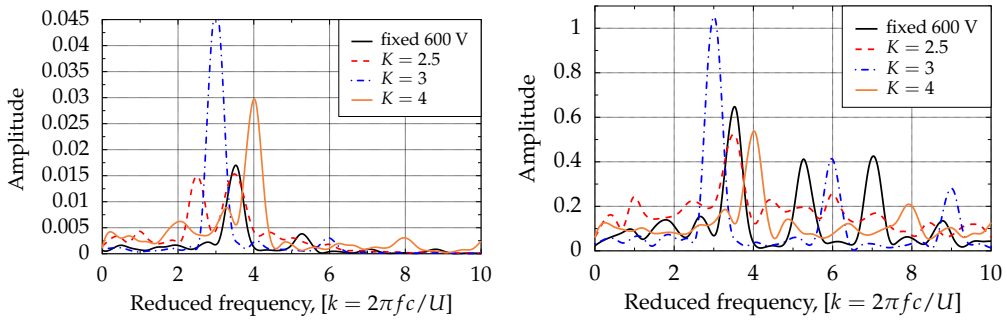

(a) Structure. (b) Pressure.

Figure 6.4: Spectra for $\alpha = 12^\circ$ and $A = 300$ V.

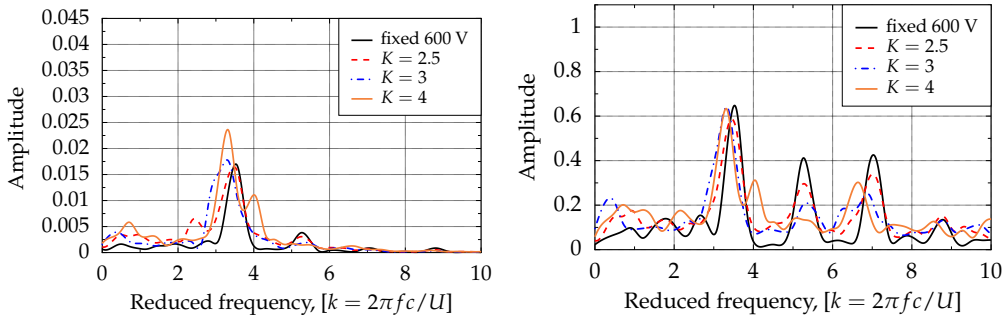

(a) Structure. (b) Pressure.

Figure 6.5: Spectra for $\alpha = 12^\circ$ and $A = 100$ V.

Moreover, the frequency lock-in is triggered in the fluid-structure coupling of an electroactive membrane wing only with a large amplitude of

the forcing frequency ($A = 300$ V). In fact with a smaller input amplitude ($A = 100$ V) the system's response does not show shifts in the main frequency but only exhibits smaller peaks relative to the forcing frequency (Fig. 6.5).

As also reported by Curet [31], excitation at the resonance frequency determines the degradation of the aerodynamic characteristics of the membrane, whereas actuation at a slightly lower frequency determines an overall positive aerodynamic enhancement. This can be attributed to the very high amplitude oscillations which occur at the resonance frequency along with the excitation of many additional modes. This is clear if we look at the displacement contours reported in Fig. 6.6 for an input amplitude $A = 300$ V at angles of attack $\alpha = 8°$ and $\alpha = 20°$. At $\alpha = 8°$ the resonance occurs at $k = 3$ where the membrane shows high displacements with more than one mode of vibration. However, at $k = 2.5$ the membrane oscillates in its first mode with a smaller amplitude than the case at $k = 3$, but still with larger and more coherent oscillations than in the case with a fixed voltage.

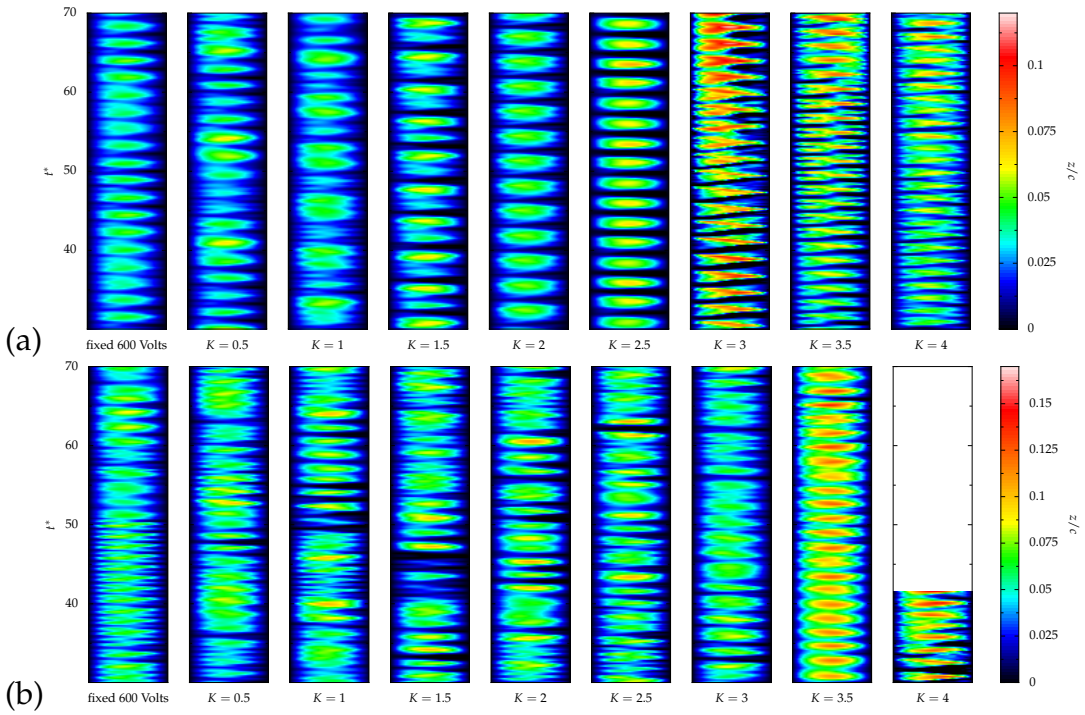

Figure 6.6: Displacement contours for $A = 300$ V. (a) $\alpha = 8°$, (b) $\alpha = 20°$.

The same can be observed at $\alpha = 20^\circ$ and $k = 3.5$ which is the closest frequency to the resonance, occuring at $k = 4.5$. For the case at $\alpha = 20^\circ$ and $k = 4$, data is only available to $t^* = 45$ because the simulations diverged due to the very large membrane displacement. In fact as the frequency lock-in occurred the maximum displacement was growing over time (red line in Fig. 6.7) and exceeded the maximum displacement allowed by the current numerical setup. In particular the mesh motion solver started generating high aspect ratio and high skewness cells and eventually generated negative volume cells which made the fluid mesh invalid.

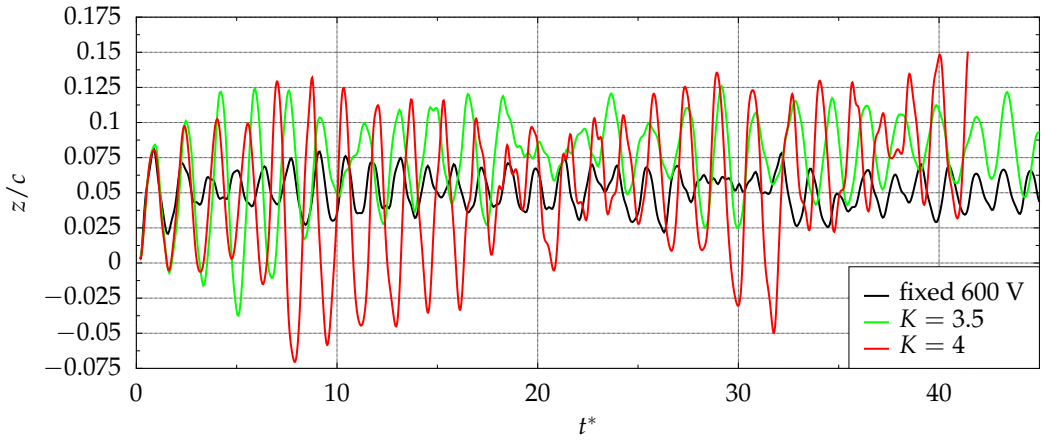

Figure 6.7: Midpoint displacement history for $\alpha = 20^\circ$ and $A = 300$ V.

The increased camber at voltage frequencies close to the resonance is the main reason of the enhanced lift, especially at high angles of attack. Fig. 6.8 shows the lift coefficients for every forcing frequency and every angle of attack. In particular at $\alpha = 20^\circ$ (Fig. 6.8b) an improvement of 8% is observed at $k = 3.5$ whereas a sharp reduction of -4% occurs just at $k = 4$ as the voltage frequency approaches the resonance at $k = 4.5$. On the other hand, for $\alpha = 12^\circ$ (Fig. 6.8b), where the resonance occurs at a lower frequency, a maximum enhancement of the lift coeffcient of 4% exists at $k = 2.5$ and a dramatic drop of -6% occurs right at the resonance frequency of $k = 3.5$. In common with the findings of Curet is also the fact that some combinations of voltage frequency and angles of attack can worsen the aerodynamic performance of the membrane wing as happens

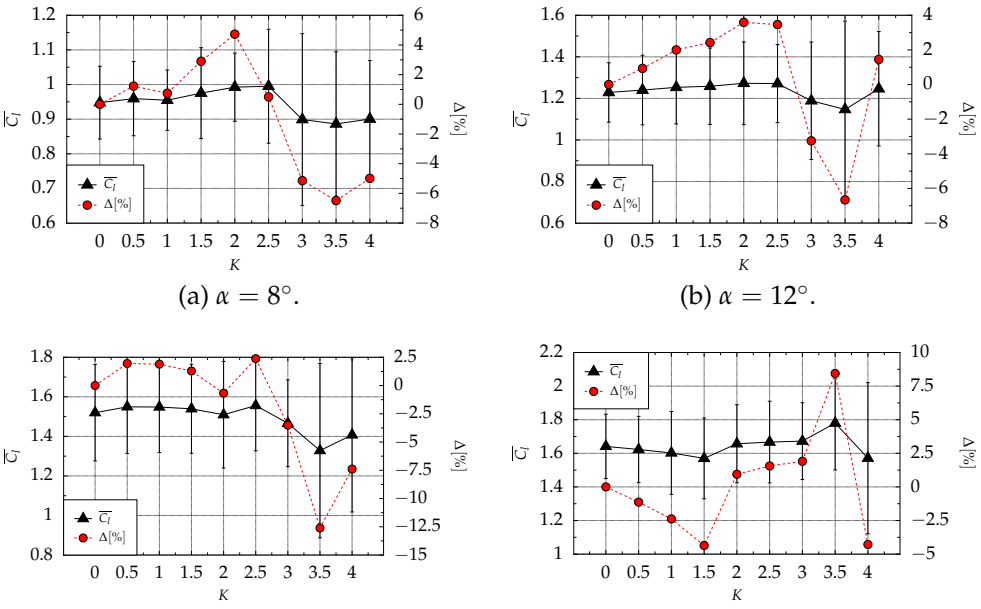

(a) $\alpha = 8°$.

(b) $\alpha = 12°$.

(c) $\alpha = 16°$.

(d) $\alpha = 20°$.

Figure 6.8: Lift coefficient for $A = 300$ V.

for example at $\alpha = 20°$ for reduced frequencies $k < 2$ (Fig. 6.8d).

However, the maximum enhancement in lift from the simulations of this work is smaller than the one found by Curet who reported improvement in the lift coefficient of up to 20%. This gap might be attributed to many differences between the model of the present study and the one of Curet. First, all the simulations presented here are of a 2D laminar flow at $Re = 2500$, whereas the Reynolds number of Curet's experiments is $Re = 57k - 80k$ where the enhancement in lift might be due to transition to a turbulent boundary layer, which is not considered in this work. The oscillations of the membrane in the Reynolds number analyzed by Curet might be acting as boundary-layer trip which has been shown to improve the aerodynamic performance of a wing [24]. Secondly, the material analyzed in this study is different from the acrylic adhesive material VHB 4910 considered by Curet. In fact the constants for the Neo-Hooken formulation used here have been chosen to fit with the results of the material used for the validation of the FSI solver in the previous chapter and recently published by the author [27]. Finally, the initial prestrain and voltages applied

are different between this and Curet's study in order to be consistent with the validation of the Neo-Hookean material.

6.1.1 Membrane forced at its natural frequency

A last test with the open loop control has been made here in order to verify if feeding the membrane with its own structural frequency would eventually attenuate its oscillations. Using the same setup of previous simulations, results for a membrane at $\alpha = 12^\circ$ fed with fixed 900 V show that it oscillates in its first mode at $f = 1.541$ Hz ($k = 5.5$). Therefore this case has been chosen as reference and the voltage at the same oscillating frequency has been applied

$$V = 50 \sin(2\pi f t) + 900.$$

The open loop control is applied to the membrane starting from two different times of the reference case, $t^* = 30$ and $t^* = 30.58$, corresponding to the membrane having respectively a high and a low displacement. The resulting displacement and pressure history are shown in Fig. 6.9 and 6.10. In both cases the oscillations are amplified rather than attenuated. Only for the case when the control starts from a high displacement the oscillations are reduced in the first 5 nondimensional time units. In fact at the beginning of the simulation the forcing and the natural frequencies have opposite phases and they cancel out. However after a short transient the membrane is forced to shift phase and therefore starts to resonate. In the other case the two phases are already aligned and the oscillations grow bigger from the the beginning of the simulation.

This behaviour could have been expected as it is the response of a system excited at its natural frequency. Therefore these simulations showed that an other approach has to be taken if we want to reduce the oscillations of the membrane. In the next section a closed loop control is analyzed where the membrane is used also as a sensor. In fact as the membrane stretches and relaxes in response to the fluid-structure coupling, it induces

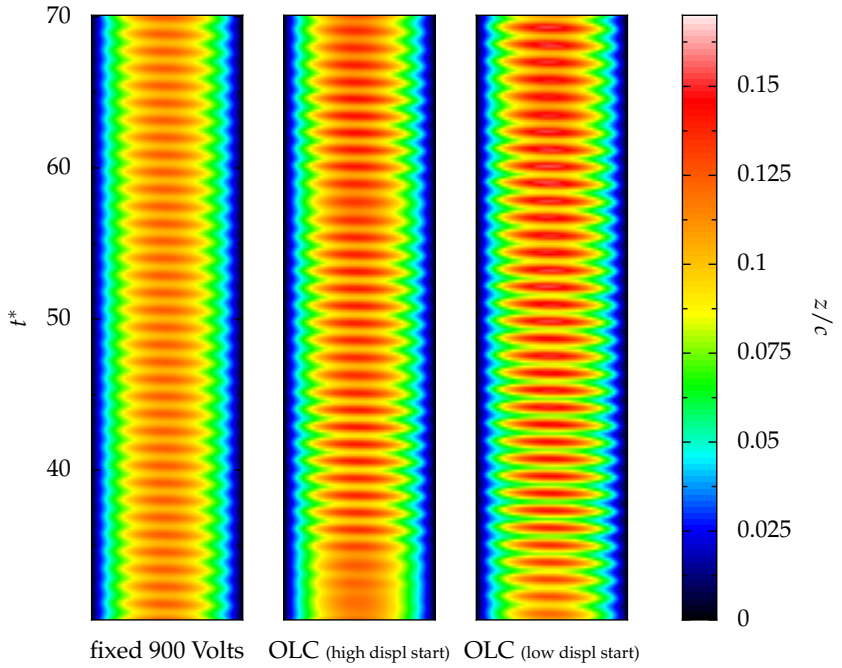

Figure 6.9: Displacement history for a membrane at $\alpha = 12°$ with open loop control (OLC) and same forcing frequency as the natural frequency of the system.

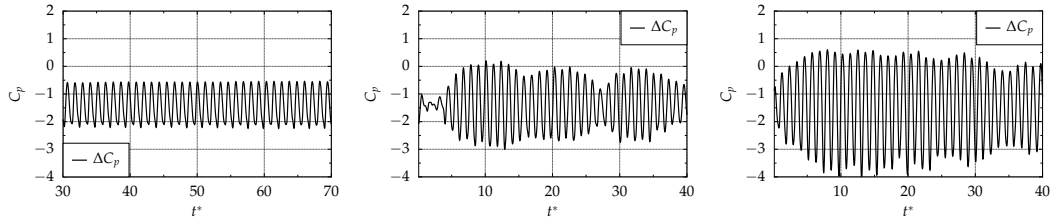

(a) fixed 900 V (b) high displacement start (c) Low displacement start

Figure 6.10: Pressure history

a variation in the voltage across the membrane. This voltage can be used as input for a proportional integral (PI) control.

6.2 Closed loop control

The first step in using a PI controller for the membrane is to define an output to monitor through a sensor. This might be tricky because we ul-

timately want to be able to control an aerodynamic property of the membrane, such as lift coefficient or aerodynamic efficiency. Even though the lift coefficient can be calculated from a CFD simulation and the error can be used to calculate the actuator input, in a real application it is impractical to have a direct measure of the lift. However the electromechanical characteristics of the membrane can be exploited as it would experience a voltage variation in response to a state of mechanical stress. In fact as feeding the membrane with an electric field will generate the Maxwell stresses across it, with the same principle mechanical stresses will modify the thickness of the membrane and therefore the electric field across it. In this way the electroactive membrane itself can be used as a sensor and an indirect measure of the lift can be obtained through the state of stress that it transfers to the membrane. In fact the membrane's lift varies as the mean camber does, but at the same time the membrane's camber varies in response to a voltage input which relaxes or stiffen the membrane.

For an electroactive membrane the total stress is given by the sum of the mechanical and electrical stress (see Section 2.3). Therefore the electrical stress can be modulated in order to compensate the variations of mechanical stress due to the fluid-structure coupling and keep the total stress - and consequently the displacement and the lift coefficient - as constant as possible.

In 2D the Maxwell stress reads

$$\begin{aligned}\sigma_e &= \varepsilon_0\varepsilon_R \left[\underbrace{\begin{pmatrix} 0 & 0 \\ 0 & \left(\frac{\phi}{h}\right)^2 \end{pmatrix}}_{\mathbf{E}\otimes\mathbf{E}} - \frac{1}{2} \underbrace{\begin{pmatrix} \left(\frac{\phi}{h}\right)^2 & 0 \\ 0 & \left(\frac{\phi}{h}\right)^2 \end{pmatrix}}_{(\mathbf{E}\cdot\mathbf{E})\cdot\boldsymbol{I}} \right] \\ &= \varepsilon_0\varepsilon_R \begin{pmatrix} -\frac{1}{2}\left(\frac{\phi}{h}\right)^2 & 0 \\ 0 & \frac{1}{2}\left(\frac{\phi}{h}\right)^2 \end{pmatrix},\end{aligned}$$

therefore a measure of voltage from the state of stress in the chordwise

direction, E_{xx}, can be derived as

$$V_{out} = h\sqrt{\frac{2E_{xx}}{\varepsilon}}.$$

For the purpose of the simulations we have assumed a constant thickness, h, whereas in reality it varies with the stress. However in our simulations the strain along the chord is less than 10% and the thickness variation has a neglectable effect on the fluid-structure coupling (the chord to thickness ratio is 750). In practice using the membrane as sensor can be made applying a second electrode on top of the actuator electrode - isolated from this one - and reading the voltage variations on this second circuit [117]. We assume that the sensor electrode is applied in the same way of the actuator electrode along the whole surface of the membrane, therefore the output voltage is a measure of the average stress across the membrane. The information about the instantaneous state of the stress of the membrane through the voltage reading, V_{out} can be used to design a control law for the actuation voltage, V_{in}.

6.2.1 Proportional Integral Control at $\alpha = 12°$

In the first set of simulations we attempt to reduce the oscillations of the case used previously for the openloop control (Section 6.1.1) at $\alpha = 12°$ with 900 V oscillating in its first mode at $k = 5.5$. The proportional controller reads

$$V_{in} = V_0 + \mu_p \left(V_{out} - V_{target}\right), \tag{6.1}$$

where $V_0 = 900$ is the offset voltage we modulate around, μ_p is the proportional gain, V_{out} is the instantaneous voltage reading from the sensor circuit and V_{target} is the voltage value which corresponds to the constant state of stress we want to achieve. Generally V_0 and V_{target} do not have the same value because they are measured on different circuits (actuator and sensor respectively). In fact the V_{out} might take into account also the offset stress given by the prestrain. V_{target} is chosen as the mean value of V_{out} for the last 50 oscillations of the simulation with a constant $V_{in} = V_0 = 900$ V

and its value is $V_{target} = 1525$.

The simulation with proportional control starts from the instant of the case with fixed 900 V when the membrane experiences its maximum high displacement. The sign of the gain μ_p should be chosen in a way that the controller would compensate the mechanical stress due to the fluid-structure coupling. In this particular case where only the first mode of oscillation is present, when the camber is increasing, the in-plane relaxation of the membrane is increasing as well and the controller should contribute to stiffen the membrane to actively resist the ascending motion. On the contrary, when the camber is decreasing, the membrane is stiffening and the controller should react relaxing the membrane. However, for this first set of simulations values of $\pm\mu_p$ have been tried in order to test the reliability of the code implemented in OpenFOAM. The displacement histories and their respective spectra for different values of the gain μ_p are shown in Fig. 6.11 and 6.12.

As expected positive values of μ_p do not help to reduce the membrane's oscillations, whereas with $\mu_p = -0.5$ the amplitude is reduced by more than 50% (green line in Fig. 6.12). Increasing the negative gain makes the membrane increase its natural frequency without a further reduction in amplitude. From Fig. 6.13 it can be seen how the reduced am-

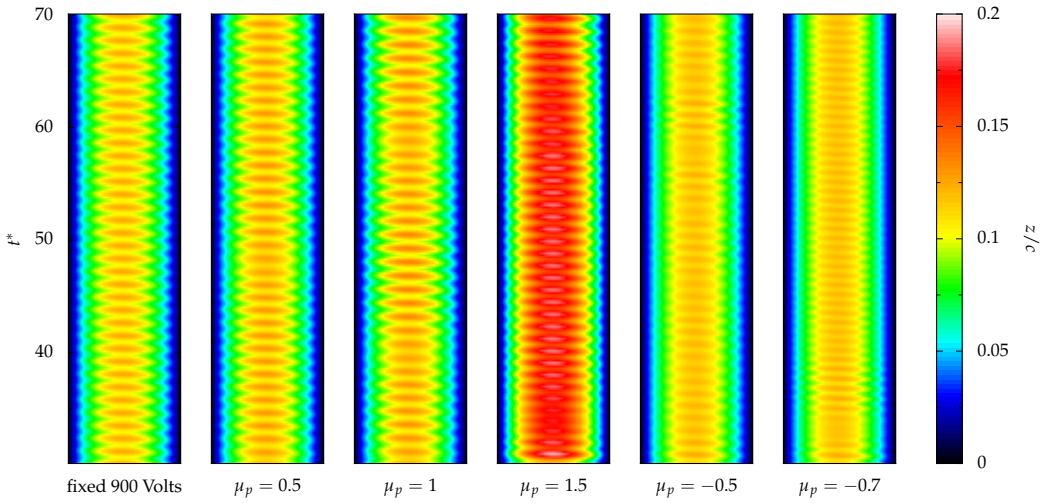

Figure 6.11: Displacement history for different values of μ_p.

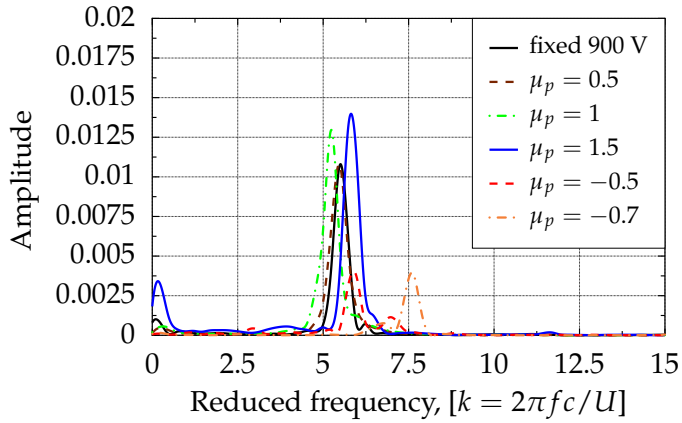

Figure 6.12: Structural spectra for different values of μ_p.

plitude of oscillations occurs when the control drives the input voltage with opposite phase to the output voltage.

The flow field of the membrane with proportional control ($\mu_p = -0.5$) is compared against the case with fixed voltage and open loop control in Fig. 6.14 showing 4 consecutive instants. At each instant the reference case (fixed 900 V) is the center figure, the open loop is the top figure and the proportional control is the bottom figure. The simulation for the open loop

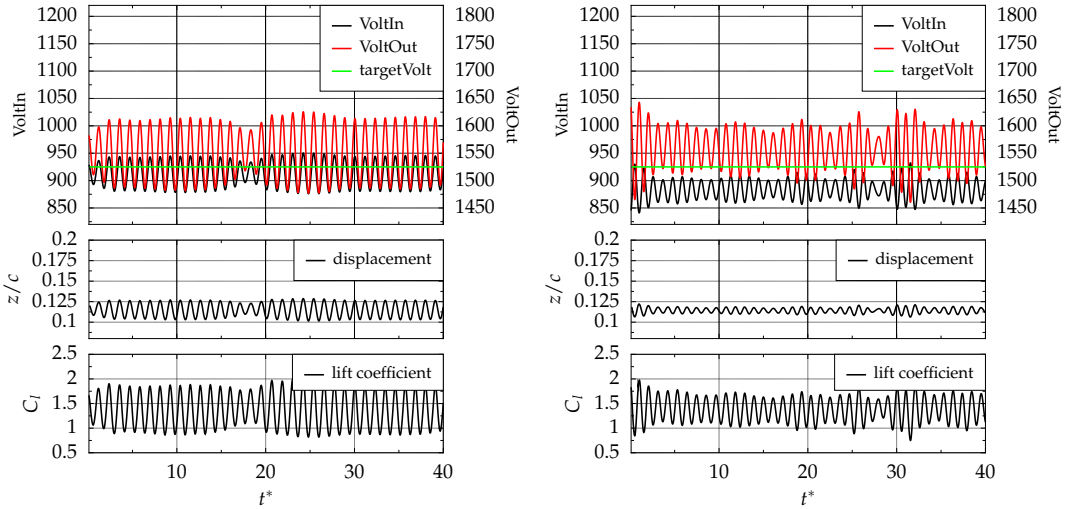

(a) $\mu_p = 0.5$ (b) $\mu_p = -0.5$

Figure 6.13: Input/output history.

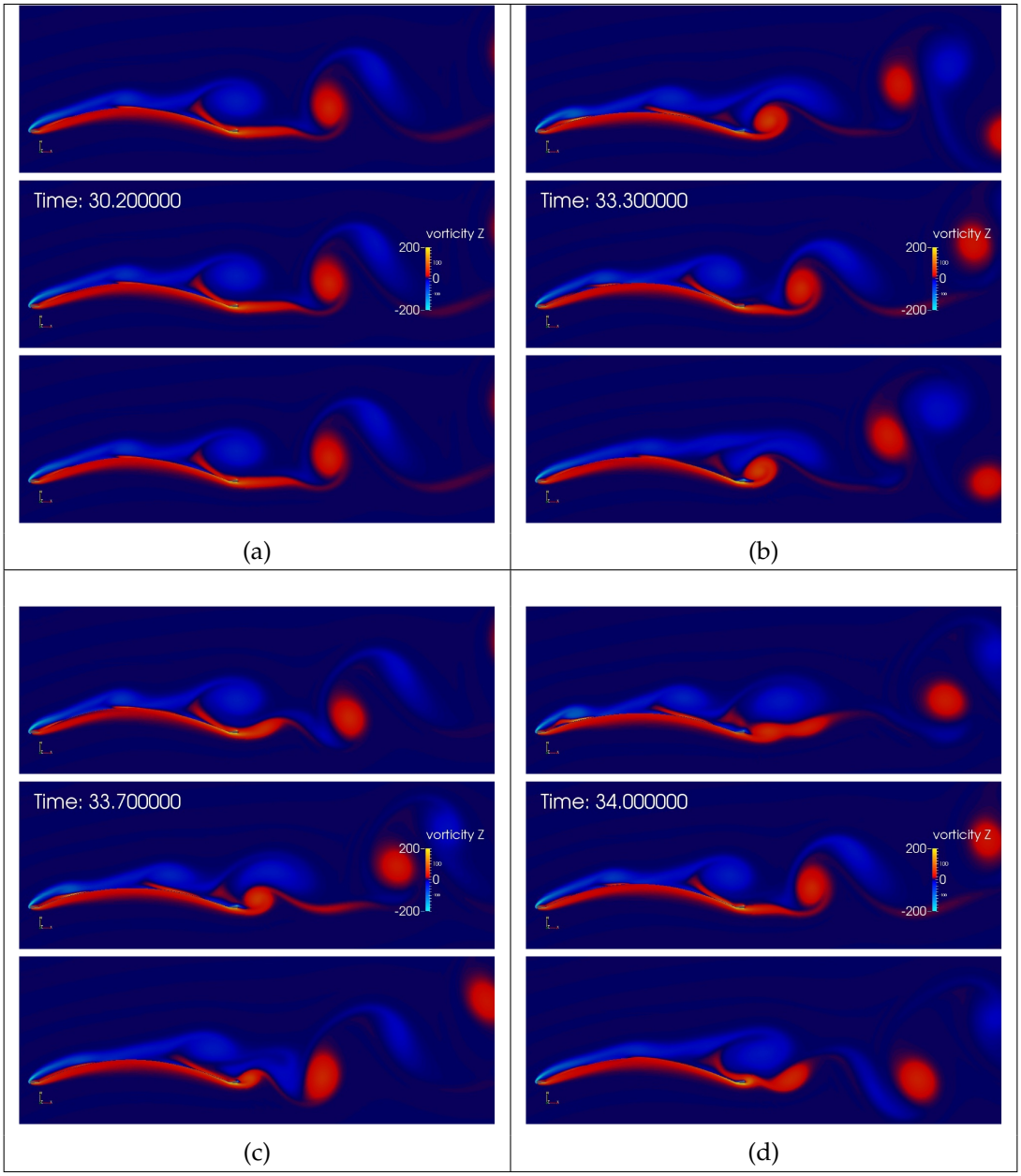

Figure 6.14: Vorticity field comparison (fixed voltage: center; open loop: top; proportional control: bottom)

and the proportional control cases start at $t = 30.2$ s of the fixed voltage run, therefore the top left comparison figure shows an identical flow structure (same initial condition). However as the time increases the beneficial effect of the proportional control becomes evident. In fact for the refer-

ence and the open loop cases the membrane's oscillations are related with the leading edge vortex shedding, whereas with the proportional control (bottom) the flow is more attached and the leading edge vortex shedding is suppressed.

An attempt to stabilize the membrane even more has been made including also an integral control. In this case the controller has the form

$$V_{in} = V_0 + \mu_p \left(V_{out} - V_{target}\right) + \mu_i \int_0^t \left(V_{out} - V_{target}\right) dt,$$

where the integral is calculated adding up the instantaneous differences between the V_{out} and the V_{target} at each time step t_n. Therefore at each time step the input voltage V_{in} is calculated as

$$V_{in}^{t_n} = V_0 + \mu_p \left(V_{out}^{t_n} - V_{target}\right) + \mu_i \sum_0^{t_n} \left(V_{out}^{t_n} - V_{target}\right) \Delta t. \tag{6.2}$$

Here the proportional gain, μ_p has been kept consistent with the value of the simulations with only the proportional control, $\mu_p = \pm 0.5$ and a value of the integral gain $\mu_i = 170$ has been found to reduce significantly the amplitude of oscillations of the monitored output, V_{out}. However looking at the displacement histories and structural spectra in Fig. 6.15 and 6.16 we do not observe a further reduction of structural oscillations with proportional and integral control, but rather a shift to lower frequencies. In fact with proportional control only and $\mu_p = -0.5$ the membrane was oscillating at $k \approx 6$ (red dashed line in Fig. 6.12) whereas adding the integral control there are two main peaks in the structural spectra at $k \approx 3$ and $k \approx 4$ with the same amplitude as the case with proportional control only.

When using also the integral control we notice that the output signal is actually kept around the target value with an amplitude of less than 10 V (red line in Fig. 6.17) whereas for the case with only proportional control the output had an amplitude of 100 V (Fig. 6.13). However now the input voltage varies in a range of 200 V (black line in Fig. 6.17) with many additi-

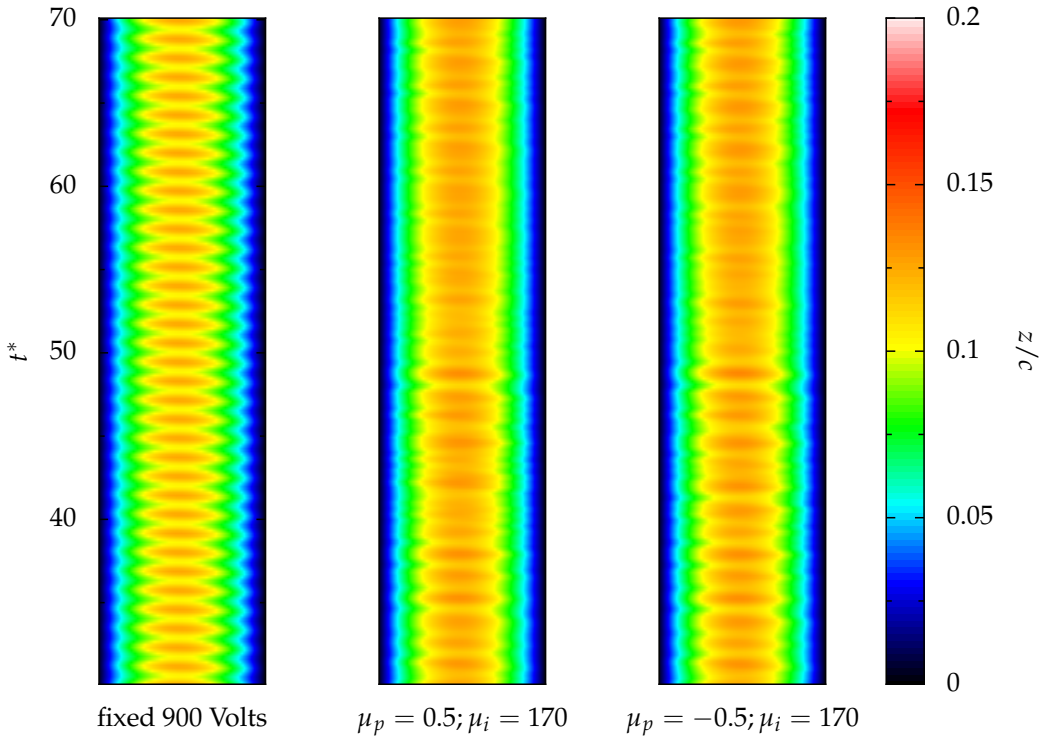

Figure 6.15: Displacement histories of PI control.

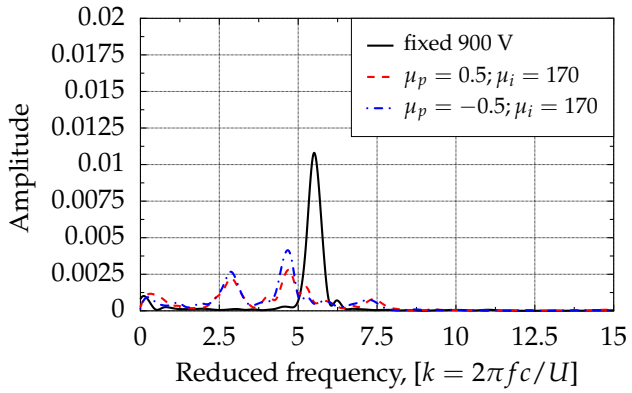

Figure 6.16: Structural spectra for the PI cases.

onal frequencies whereas in the case with only proportional control the input voltage varied in a range of 50 V oscillating at the same structural frequency of the membrane (Fig. 6.13). Also, comparing the V_{in} signal in Fig. 6.17 and 6.13 it is evident how the way the PI control works is

to increase the V_0 in equation 6.2. In fact V_{in} is not oscillating around the initial value of $V_0 = 900$ as in the proportional control, but around a higher value $V_0 \approx 1000$.

From Figs. 6.15 and 6.16 we notice also that when proportional and integral control is applied using either a positive or negative proportional leads to a similar behaviour of the membrane. This can be explained if we compare separately the contribution of the proportional and integral term of equation 6.2 plotted in Fig. 6.18. The integral contribution builds up at the very beginning of the simulation to a value 4 times larger than the proportional contribution and drives the error immediately to a very small value.

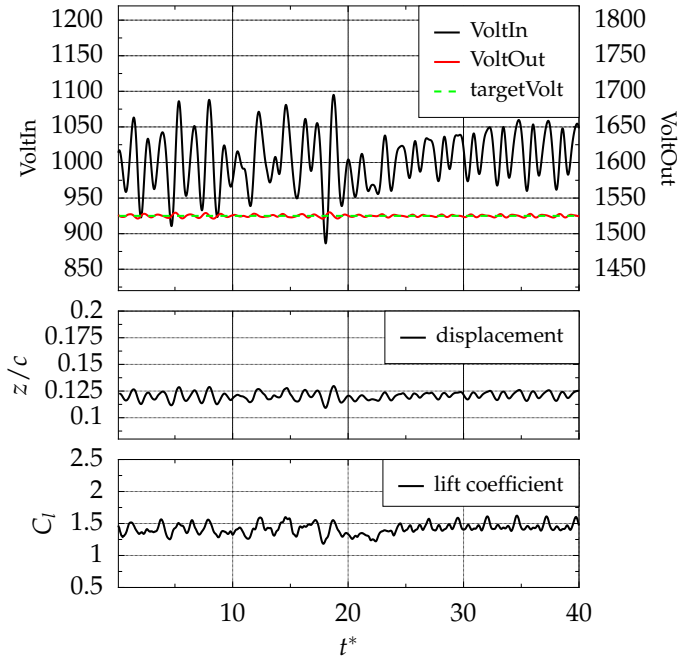

Figure 6.17: Input/output history for $\mu_p = 0.5$ and $\mu_i = 170$.

Already after $t^* = 0.1$, the error is very small and therefore the proportional contribution is negligible. On the contrary the integral term oscillates around the value built from the start of the simulation and its contribution only is able to keep the error at a very low value. In this condition the controller behaves as an integral compensator.

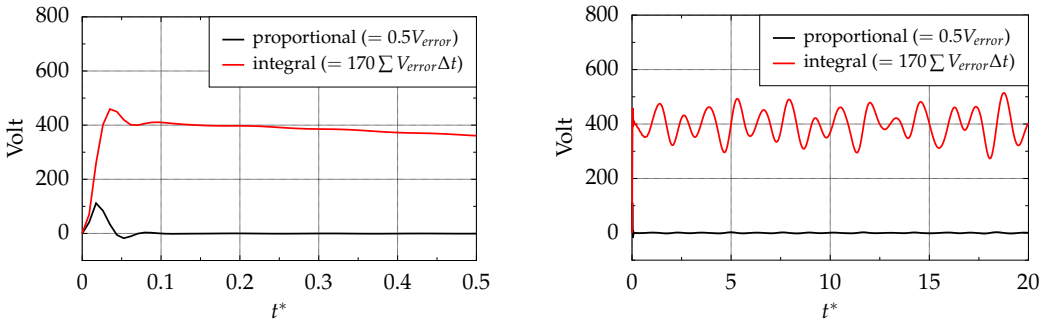

Figure 6.18: Proportional and Integral contribution to the control input. On the left, zoom to the beginning of the simulation.

It is worth pointing out that the choice of the target voltage defines also the mean displacement the membrane is going to oscillate about. Therefore the target voltage can be used to modify the mean camber and consequently the aerodynamic characteristics of the membrane. In this case we chose a target value which was the average of the output voltage during the last 50 cycles of the case with fixed voltage and we would expect a similar mean displacement for the case with fixed and proportional-integral control. However this is not the case as we observe an increment of the 9% in the maximum mean displacement of the membrane as shown in Fig. 6.19. This translates in an increment of the mean lift coefficient by the 1.6% and of the mean drag coefficient by 7% with the beneficial effect of the oscillations being reduced more than 3 times as shown in Fig. 6.20.

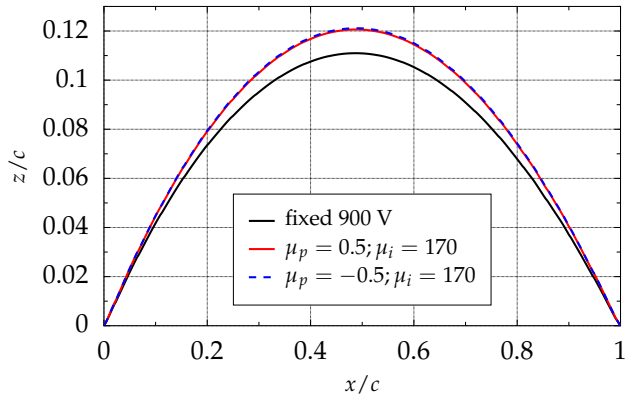

Figure 6.19: Mean displacement of the controlled membrane.

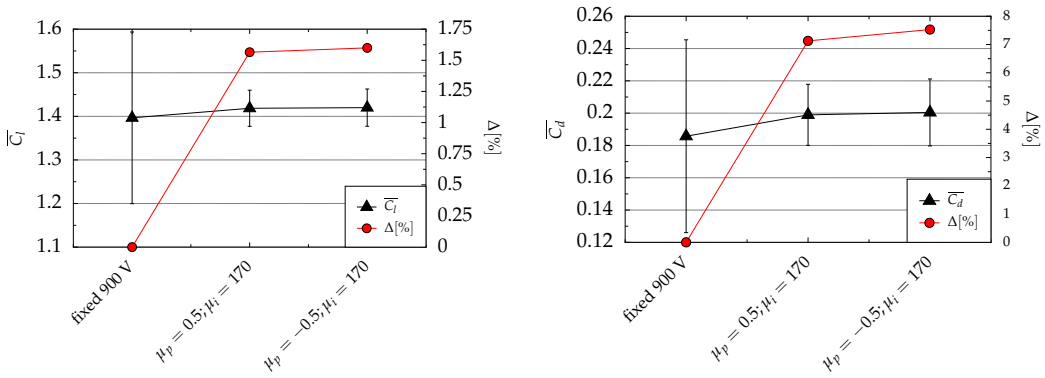

Figure 6.20: Force coefficients of the controlled membrane.

This shows the real potential of controlling a membrane wing with electroactive materials. Without the need of moving mechanisms the stiffness and therefore the camber of the membrane can be modified on demand to obtain the desired aerodynamic performance.

6.2.2 Proportional Integral Control at $\alpha = 20°$

The same type of controllers are now applied to a more complex case in order to understand whether it is possible to stabilize a membrane at a higher angle of attack oscillating with additional structural modes. The reference case is a membrane flying at $\alpha = 20°$ and with a fixed voltage of 600 V across it. With a voltage smaller than the previous case (900 V), the prestretched membrane relaxes less and therefore the maximum displacement of the membrane is smaller than before. However at $\alpha = 20°$ the fluid-structure coupling is more complex and the membrane does not oscillate in its first structural mode anymore. It is worth remembering that we are using a global sensor on the membrane, in fact the output voltage is technically a measure of the average stress across the whole membrane. At the same time the Maxwell stresses induced by the actuator are constant across the whole membrane as the electrodes are spread on the whole membrane's surface. Therefore these simulations are a good test case to evaluate if a global sensor and global actuator are able to control also a highly unstable membrane.

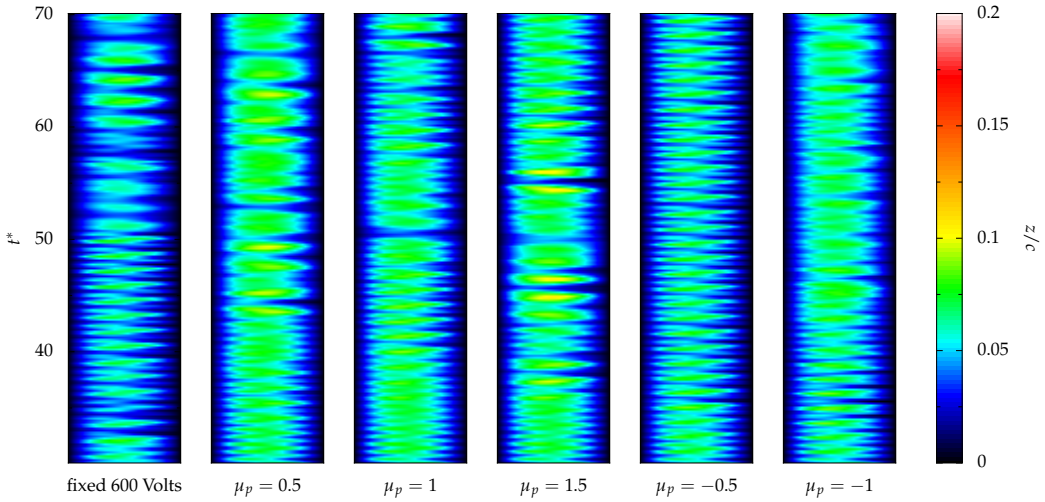

Figure 6.21: Proportional Control at $\alpha = 20°$.

The displacement history for the proportional control with different values of the gain, μ_p are shown in Fig. 6.21 and the input/output signal for $\mu = \pm 0.5$ in Fig. 6.22. Unfortunately, no matter the sign or the absolute value of the proportional gain, μ_p used for the proportional controller, the membrane does not reduce its oscillations amplitude.

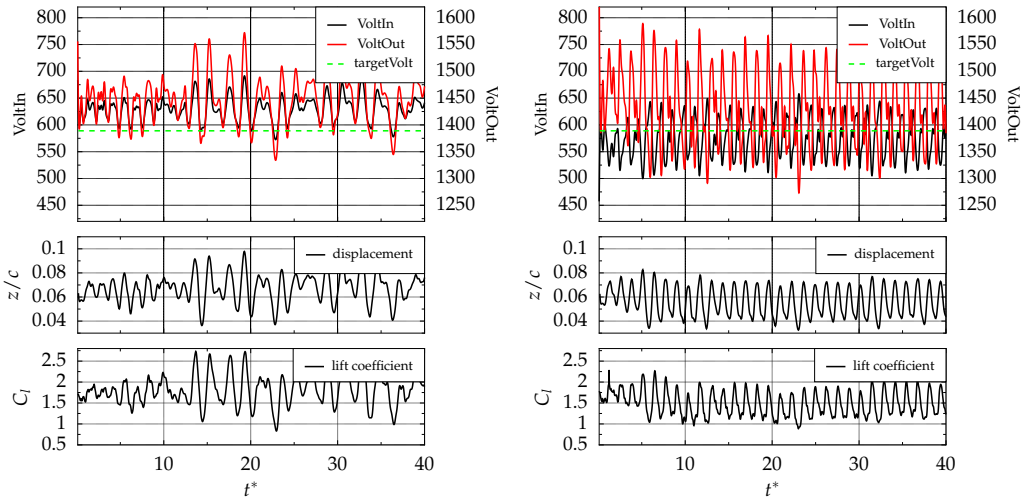

(a) $\mu_p = 0.5$ (b) $\mu_p = -0.5$

Figure 6.22: Input/Output signal at $\alpha = 20°$ with proportional control.

The same behaviour is observed also when a proportional integral control is applied (Fig. 6.23). In this set of simulations also a local sensor (LS) has been considered (center graph). In practice rather than using the average of the stresses to calculate the output voltage, only the stress value at the mid-chord location has been used. This would be a simplification of the condition where a tiny sensor's electrode is applied at the center of the membrane. Unfortunately also in this case the membrane cannot be controlled.

However, if we look at the signal history in Fig. 6.24 we notice that the proportional integral control is actually working in reducing oscillations of the output voltage as its value is always around the target value. This suggests that in these conditions the global output voltage is not representative of the membrane's displacement which is ultimately what has to be controlled.

In fact, looking at the stress distribution along the chord at two instants where the membrane experiences a high and low displacement (Fig. 6.25) we notice that they have a similar average value ($\approx$ 104 Pa) but completely different displacement as we have additional structural modes. Instead, for the case at $\alpha = 12^\circ$ where only the first structural mode is present the

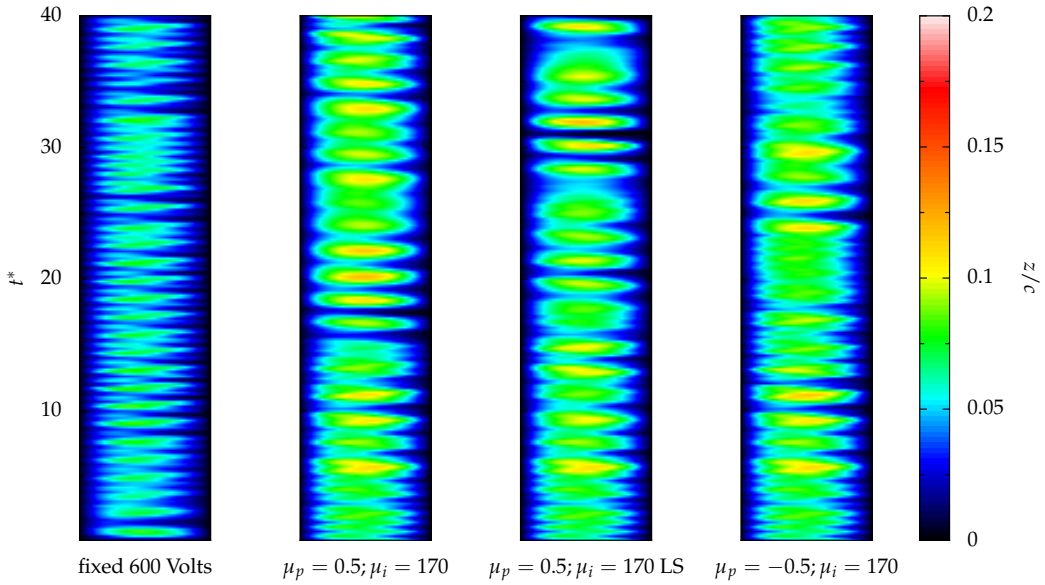

Figure 6.23: Proportional integral control at $\alpha = 20^\circ$.

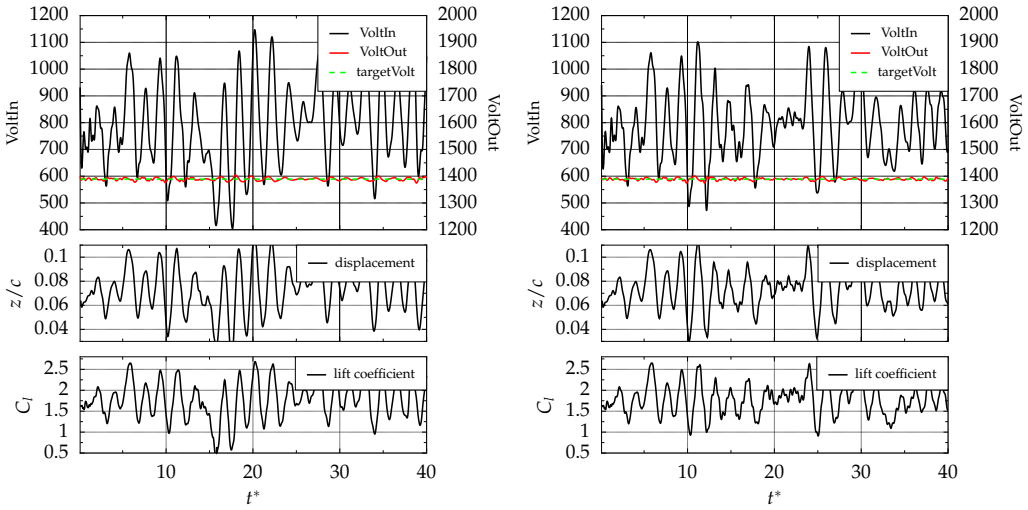

(a) $\mu_p = 0.5$, $\mu_i = 170$. (b) $\mu_p = -0.5$, $\mu_i = 170$.

Figure 6.24: Input/Output history at $\alpha = 20°$ with proportional integral control.

average value of the stress was more representative of the membrane's displacement (Fig. 6.26).

In order to have an effective control of a membrane which experiences many structural modes we should use multiple sensors as well as multiple actuators, each of them taking control of the portion of the membrane where the curvature has the same sign. Moreover, the interaction between different inputs and outputs voltages would make the control of the membrane even more complex. This kind of study would goes far beyond the purpose of this thesis but leaves a wide field of future work on controlling an electroactive membrane wing.

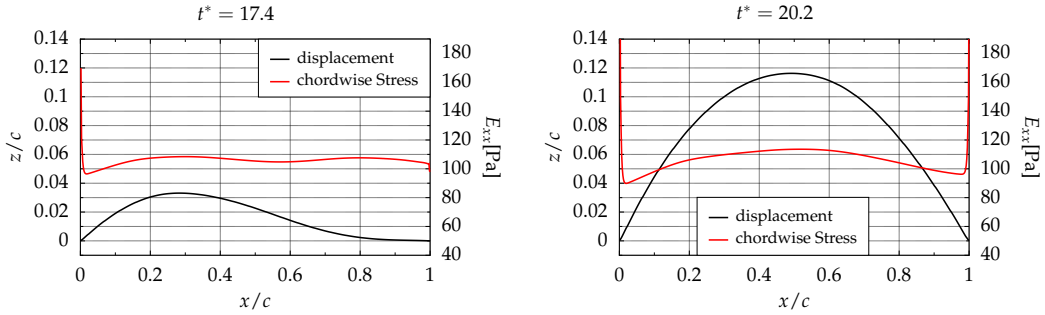

Figure 6.25: Chordwise stress distribution at $\alpha = 20°$.

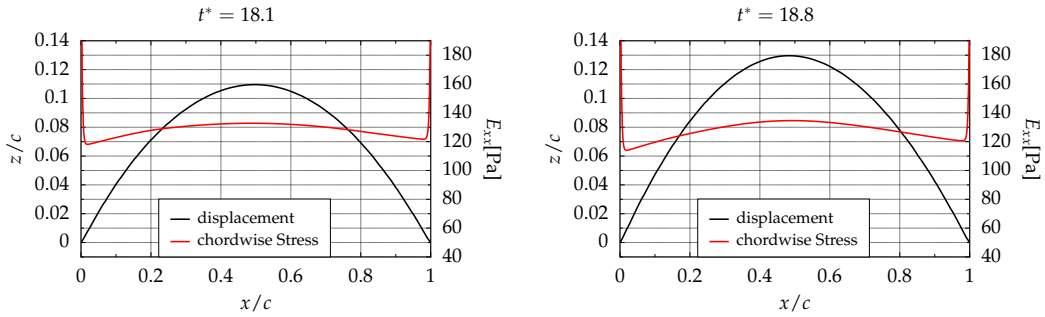

Figure 6.26: Chordwise stress distribution at $\alpha = 12°$.

6.3 Summary

The simulations in this Chapter have investigated the effect of a dynamic change of the stiffness of the membrane due to a time-varying voltage. This has been used in Section 6.1 to evaluate whether the aerodynamic characteristics could be further improved. It has been found that with an open loop control (i.e. feeding the membrane with a sinusoidal voltage) the mean lift is increased with a forcing frequency slightly smaller than the resonance frequency. However, for a large forcing amplitude the frequency lock-in phenomenon occurs and at the resonance frequency the aerodynamic performances worsen abruptly.

Feeding a varying voltage to reduce the oscillations amplitude of the membrane's displacement at high angles of attack has been also investigated. The first experiment in Section 6.1.1 demonstrated that feeding the membrane at its natural frequency but with opposite phase was not enough to cancel out the oscillations, as after the initial transient the membrane was forced to shift phase and kept oscillating at the same frequency. Therefore in Section 6.2 a closed loop control has been considered exploiting the electromechanical characteristics of dielectric elastomers and using the membrane itself as a sensor. In fact the stress due to the fluid-structure coupling can be translated into a voltage reading and used as a control variable for a proportional integral controller. A sensor's electrode spread across the whole surface of the membrane gives a voltage reading propor-

tional to the average state of stress of the membrane and it has been found to be very effective at moderate angles of attack when the membrane oscillates in its first mode. In fact, with a proportional integral control it is possible to reduce the amplitude of oscillations by more than 50%. On the contrary, at higher angles of attack when the membrane oscillates with additional structural modes, a global sensor cannot give representative information of the membrane's displacement and a proportional integral control is not able to reduce the membrane's oscillations. This suggests that more sensors and a more complex control law needs to be considered.

Chapter 7

Conclusions

Fluid-structure interaction simulations of a 2D electroactive membrane in a laminar and incompressible flow have been conducted in the OpenFOAM framework. The existing solver `icoFsiElasticNonLinULSolidFoam` has been used to simulate the same cases as in the reference by Gordnier [51] and the results obtained (Section 4.2) are in good agreement with the reference, suggesting that OpenFOAM is a suitable CFD tool to predict the passive fluid-structure coupling of membranes. This preliminary study has been the base to develop a hyperelastic Neo-Hookean structural solver to take into account the large strains achieved by electroactive polymers. In this thesis an electroactive membrane has been modelled with a compressible Neo-Hookean constitutive law and its compliance has been modified by means of electrostriction. The Neo-Hookean structural solver has been validated (Section 4.3) simulating the experiments of Tagarielli et al. [124]. The validation also allowed to find the range of voltages which have been used to modify the stiffness in the FSI simulations of the hyperelastic membrane (Section 4.4).

Electrostriction is generally applied to prestretched membranes. The prestretch is requested because it increases the break-out strength and decreases the membrane thickness so a smaller value of voltage can be applied. Therefore a prestretched membrane has been simulated first, and a static voltage has been applied afterwards. Results show that for a pre-

stretched membrane the mean camber is reduced compared with a non prestretched one because of the stiffness produced by prestretch. In contrast, since the main effect of the Maxwell stresses is to produce an in-plane relaxation, when a prestretched membrane is affected by electrostriction it can achieve a higher camber. The aerodynamic characteristics of activated and non-activated membranes as well as partially activated ones have been deeply analyzed showing that the lift increases as the camber increases and the aerodynamic efficiency increases significantly as the point of maximum displacement shifts toward the front. Moreover the results reported in this work show an aerodynamic improvement at low angles of attack for membranes whose back section has been activated with a fixed voltage. This improvement is due to the excitation of the second structural mode which is coupled with a higher vortex shedding frequency. The vortices released at the leading edge travel downstream increasing the suction on the top of the membrane and therefore increasing the overall lift.

Further simulations have been performed with a sinusoidal voltage driven at different frequencies across the membrane (Section 6.1). Results show that the mean lift and lift-to-drag ratio are enhanced when the forcing frequency approaches the natural frequency of the system but drop sharply as soon as the resonance is reached. These results are qualitatively consistent with experiments by Curet et al. [31] but quantitative discrepancies are observed and might be explained by the choice of different flow and material characteristics between the experiments and the numerical simulations.

Finally, the last set of cases analysed represents to the author's knowledge, the first documented simulations of the active control of a membrane wing in order to achieve optimized flight performances (Section 6.2). In fact, an offset voltage can be applied to the membrane to modify the mean camber and therefore to achieve a mean target lift coefficient. Varying the mean camber has the same effect as using a flap, but with the advantage of not having any moving mechanism. Moreover as the camber increases it creates more lift at smaller angles of attack where the interaction between the fluid and the structure is not as strong as at high incidences. Around

this offset value the voltage is controlled in time in order to keep the target lift coefficient as constant as possible in response either to a gust or to the intrinsic structural dynamics of the membrane. For this purpose the electromechanical characteristics of the electroactive polymers are exploited in order to use the membrane itself as a sensor. In fact, the interaction between the electric field across the membrane and its mechanical state of stress is represented by the Maxwell stress tensor. In this study the electrodes are spread across the whole surface of the membrane therefore a voltage reading can be taken on a first layer of compliant electrodes as measure of the mean stress across the membrane. This signal can be used to design a control law and feed the input voltage on a second compliant layer to actuate the membrane.

Results show that with this configuration, a proportional integral control is able to reduce the membrane's oscillations at medium angles of attack as long as the membrane oscillates in its first structural mode, delivering a more stable flight and smoother response to a gust. However increasing the angle of attack the fluid-structure interaction becomes more complex and only one actuator applied to the whole membrane is not adequate anymore to damp oscillations. In fact the membrane oscillates with additional structural modes which are not captured when the output signal is function only of the average stress across the membrane. In order to address this issue multiple sensors and actuators as well as a more complex control law need to be considered.

7.1 Original contributions

The numerical tools developed during this thesis not only have allowed to have an insight in the complex physiscs of the fluid-structure interaction of membrane wings, but more importantly showed the great potential that an actuated membrane has to control its flight performances. In summary, the work done in this thesis resulted in the original contributions here highlighted:

1. The development of a strongly coupled FSI solver, `pimpleFsiHyperElasticULSolidFoam`, in the opensource framework OpenFOAM. It extends the capabilities of the existing `icoFSIElasticNonLinULSolidFoam` with the new following features:

   - it uses the PIMPLE algorithm in order to predict a more accurate and stable solution for time steps larger than unity;
   - it allows to choose an arbitrary size of the moving mesh domain through the definition of a `subsetMotion` mesh. This feature drastically reduces the computational time if the moving mesh is smaller than the whole fluid domain;
   - it allows to nondimensionalise the FSI residual by an arbitrary length size. In particular, in this work the FSI residual was expressed as fraction of the membrane thickness.
   - it allows to choose either a Saint Venant-Kirchhoff or a Neo-Hookean constitutive law for the solid;

2. The derivation of a compressible Neo-Hookean constitutive law for hyperelastic materials in the Updated Lagrangian formulation. Moreover, the equation of the Maxwell stress tensor has been included in the Neo-Hookean solver in order to calculate the stress induced by electrostriction. Given an electric potential field as boundary condition for the solid, the Maxwell stress tensor is calculated starting from the electrostatics equations and added to the mechanical stress tensor.

3. The `pimpleFsiHyperElasticULSolidFoam` solver along with time-varying boundary conditions have allowed to design a control law for the activation of the membrane. With an open loop control the electric field across the membrane was forced to oscillate at different frequencies showing that the mean lift was enhanced for forcing frequencies close to the resonance. Also, the open loop control simulations have allowed for the first time to observe the phenomenon of the frequency lock-in for an electroactive membrane wing.

4. The closed loop control simulations have indicated a practical way to exploit the electromechanical characteristics of a dielectric elastomer and use the membrane itself as a sensor. The real time reading of the varying electric field across the membrane due to the mechanical response to the fluid-structure coupling gives an indirect measure of the membrane's displacement. This input can be used in realistic applications (experimental setup or operative flight conditions) to feed a closed loop controller. Moreover, simulations at a moderate angle of attack have showed the effectiveness of a proportional integral control in reducing significantly the amplitude of oscillations of the membrane.

7.2 Future work

The purpose of this thesis was to develop a multiphysiscs simulation framework in order to help the design of membrane wings for micro air vehicle applications. On the one hand the results achieved in this dissertation showed that an electroactive membrane wing is a promising device for future micro air vehicle applications because of its aerodynamic performance and control authority. On the other hand, more work is needed in order for an electroactive membrane wings to achieve the same flight performance that bats and insects have gained in millions of years of evolutions. Therefore, to conclude, the additional features to be considered to further help the understanding and the design of a successful membrane wing in the years to come are here proposed:

3D simulations. A complete design of a membrane wing would include addressing the issues of 3D flow effects. Therefore 3D simulations need to be performed in order to understand the influence of the aspect ratio and wing shape on the overall flight performances.

Turbulence modeling The flow at larger Reynolds numbers needs also to be considered in order to validate the results from the FSI simulations against experimental data. In fact, all the experiments about

membrane wings are performed in a range of Reynolds numbers where turbulence effects cannot be neglected. Phenomena like transition from laminar to turbulent boundary layer can lead to a significant improvement of the aerodynamic characteristics of a membrane [24] and need to be accurately predicted.

Leading and trailing edge effects. The vortices shed from the leading edge play a significant role in the overall flight performance of a membrane wing as it has been shown in this thesis. Not only the movement of the membrane is responsible of how these vortices are shed but also the shape of the leading edge struts [4]. Therefore more simulations with different shapes of the leading and trailing edge might help to find the optimal one. Moreover, in this work the struts where fixed, whereas for a more realistic simulation the contribution of their rigid body rotation to the vortex shedding should be accounted for.

More sophisticated constitutive laws. For validation purposes the structural parameters of the Neo-Hookean membrane used in this thesis have been calculated in order to match the nondimensional ones used by Gordnier (see Section 4.4). Future simulations might be performed with different solid parameters in order to match those of new hyperelastic materials. Moreover, in this thesis the deformation hysteresis due to viscoelasticity effects has been neglected. This property can significantly change the behaviour of the fluid-structure coupling and its effects should be considered using a more sophisticated constitutive law.

Different control laws. The simulations performed in Section 6.2.2 highlighted that at high angles of attack when the membrane oscillates with many structural modes it is not possible to reduce its oscillations using only one global sensor and one global actuator. Therefore for high unsteadiness conditions a more effective control strategy should be considered. The input from multiple sensors should

be used in order to have a meaningful information about the instantaneous shape of the membrane. At the same time multiple actuators should be coordinated by a complex control law in order to locally modify the membrane's stiffness.

Appendix A

Derivation of incremental form of 2nd Piola-Kirchhoff for a Neo-Hookean material

The incremental form of the 2nd Piola-Kirchhoff for a Neo-Hookean material has been derived here by the author in order to use an Updated Lagrangian formulation in the OpenFOAM structural solver.

The 2nd Piola-Kirchhoff stress tensors for a compressible Neo-Hookean material reads

$$\boldsymbol{S} = \frac{\mu}{2} J^{-2/3} \left(\boldsymbol{I} - \frac{1}{3} \mathrm{tr}\left(\boldsymbol{C}\right) \boldsymbol{C}^{-1} \right) + \frac{\kappa}{2} \left(J - 1\right) J \boldsymbol{C}^{-1} \tag{1}$$

where $J = \det\left(\boldsymbol{F}\right)$ and $\boldsymbol{C} = \boldsymbol{F}^T \cdot \boldsymbol{F}$.

In order to calculate its incremental form

$$\delta \boldsymbol{S} = \delta \left(\frac{\mu}{2} J^{-2/3} \left(\boldsymbol{I} - \frac{1}{3} \mathrm{tr}\left(\boldsymbol{C}\right) \boldsymbol{C}^{-1} \right) + \frac{\kappa}{2} \left(J - 1\right) J \boldsymbol{C}^{-1} \right)$$

it is useful to first calculate separetely the derivative of the single terms as derivatives of the determinant, product and inverse of a tensor. Also it is

worth reminding that in the Updated Lagrangian formulation

$$\boldsymbol{F} = \boldsymbol{I} \qquad \text{and} \qquad \delta\boldsymbol{F} = \nabla\delta\boldsymbol{u}.$$

derivative of the determinant

$$\partial\Big(J\Big) = \partial\Big(\det\left(\boldsymbol{F}\right)\Big) = \det\left(\boldsymbol{F}\right)\mathrm{tr}\left(\boldsymbol{F}^{-1}\cdot\delta\boldsymbol{F}\right)$$

derivative of the product

$$\partial\Big(\left(J-1\right)J\Big) = \partial\Big(\left(\det\left(\boldsymbol{F}\right)-1\right)\det\left(\boldsymbol{F}\right)\Big)$$

$$\begin{aligned}
\partial\Big(\left(\det\left(\boldsymbol{F}\right)-1\right)\det\left(\boldsymbol{F}\right)\Big) &= \partial\Big(\det\left(\boldsymbol{F}\right)-1\Big)\cdot\det\left(\boldsymbol{F}\right) \\
&\quad + \left(\det\left(\boldsymbol{F}\right)-1\right)\cdot\partial\Big(\det\left(\boldsymbol{F}\right)\Big) \\
&= \det\left(\boldsymbol{F}\right)\mathrm{tr}\left(\boldsymbol{F}^{-1}\cdot\delta\boldsymbol{F}\right)\det\left(\boldsymbol{F}\right) \\
&\quad + \left(\det\left(\boldsymbol{F}\right)-1\right)\det\left(\boldsymbol{F}\right)\mathrm{tr}\left(\boldsymbol{F}^{-1}\cdot\delta\boldsymbol{F}\right) \\
&= \left(2\det\left(\boldsymbol{F}\right)-1\right)\det\left(\boldsymbol{F}\right)\mathrm{tr}\left(\boldsymbol{F}^{-1}\cdot\delta\boldsymbol{F}\right) \\
&= \mathrm{tr}\left(\nabla\delta\boldsymbol{u}\right)
\end{aligned}$$

derivative of the inverse

$$\partial\left(\boldsymbol{F}^{-1}\right) = -\boldsymbol{F}^{-1}\cdot\delta\boldsymbol{F}\cdot\boldsymbol{F}^{-1}$$

$$\begin{aligned}
\partial\left(\left(\det\left(\boldsymbol{F}\right)\right)^{-2/3}\right) &= -\frac{2}{3}\det\left(\boldsymbol{F}\right)^{-5/3}\partial\Big(\det\left(\boldsymbol{F}\right)\Big) \\
&= -\frac{2}{3}\det\left(\boldsymbol{F}\right)^{-5/3}\det\left(\boldsymbol{F}\right)\mathrm{tr}\left(\boldsymbol{F}^{-1}\cdot\delta\boldsymbol{F}\right) \\
&= -\frac{2}{3}\mathrm{tr}\left(\delta\boldsymbol{F}\right) = -\frac{2}{3}\mathrm{tr}\left(\nabla\delta\boldsymbol{u}\right)
\end{aligned}$$

Substituting the above relations into the differential of the 2nd Piola-Kirchhoff stress tensor

$$\delta \boldsymbol{S} = \delta \left(\frac{\mu}{2} J^{-2/3} \left(\boldsymbol{I} - \frac{1}{3} \mathrm{tr}\left(\boldsymbol{C}\right) \boldsymbol{C}^{-1} \right) + \frac{\kappa}{2} \left(J - 1\right) J \boldsymbol{C}^{-1} \right)$$

$$\begin{aligned}
&= \frac{\mu}{2} \Bigg[\left(-\frac{2}{3} \mathrm{tr}\left(\nabla \delta \boldsymbol{u}\right) \right) \left(\boldsymbol{I} - \frac{1}{3} \mathrm{tr}\left(\boldsymbol{C}\right) \boldsymbol{C}^{-1} \right) \\
&\qquad + J^{-2/3} \left(-\frac{1}{3} \mathrm{tr}\left(\delta \boldsymbol{C}\right) \boldsymbol{C}^{-1} + \frac{1}{3} \mathrm{tr}\left(\boldsymbol{C}\right) \boldsymbol{C}^{-1} \cdot \delta \boldsymbol{C} \cdot \boldsymbol{C}^{-1} \right) \Bigg] \\
&\quad + \frac{\kappa}{2} \left[\mathrm{tr}\left(\nabla \delta \boldsymbol{u}\right) \cdot \boldsymbol{C}^{-1} - \left(J - 1\right) J \boldsymbol{C}^{-1} \cdot \delta \boldsymbol{C} \cdot \boldsymbol{C}^{-1} \right]
\end{aligned}$$

$$\begin{aligned}
&= \frac{\mu}{2} \left[\left(-\frac{2}{3} \mathrm{tr}\left(\nabla \delta \boldsymbol{u}\right) \right) \left(\boldsymbol{I} - \frac{1}{3} \boldsymbol{I} \right) + \left(-\frac{1}{3} \mathrm{tr}\left(\delta \boldsymbol{C}\right) \boldsymbol{I} + \frac{1}{3} \delta \boldsymbol{C} \right) \right] \\
&\qquad + \frac{\kappa}{2} \mathrm{tr}\left(\nabla \delta \boldsymbol{u}\right) \boldsymbol{I}
\end{aligned}$$

$$\begin{aligned}
&= \frac{\mu}{2} \Bigg[-\frac{4}{9} \mathrm{tr}\left(\nabla \delta \boldsymbol{u}\right) \boldsymbol{I} - \frac{1}{3} \mathrm{tr}\left(\nabla \delta \boldsymbol{u} + \left(\nabla \delta \boldsymbol{u}\right)^T + \left(\nabla \delta \boldsymbol{u}\right)^T \cdot \nabla \delta \boldsymbol{u} \right) \boldsymbol{I} \\
&\qquad + \frac{1}{3} \left(\nabla \delta \boldsymbol{u} + \left(\nabla \delta \boldsymbol{u}\right)^T + \left(\nabla \delta \boldsymbol{u}\right)^T \cdot \nabla \delta \boldsymbol{u} \right) \Bigg] \\
&\quad + \frac{\kappa}{2} \mathrm{tr}\left(\nabla \delta \boldsymbol{u}\right) \boldsymbol{I}
\end{aligned}$$

$$\begin{aligned}
&= \frac{\mu}{2} \Bigg[-\frac{10}{9} \mathrm{tr}\left(\nabla \delta \boldsymbol{u}\right) \boldsymbol{I} - \frac{1}{3} \mathrm{tr}\left(\left(\nabla \delta \boldsymbol{u}\right)^T \cdot \nabla \delta \boldsymbol{u} \right) \boldsymbol{I} \\
&\qquad + \frac{1}{3} \left(\nabla \delta \boldsymbol{u} + \left(\nabla \delta \boldsymbol{u}\right)^T + \left(\nabla \delta \boldsymbol{u}\right)^T \cdot \nabla \delta \boldsymbol{u} \right) \Bigg] \\
&\quad + \frac{\kappa}{2} \mathrm{tr}\left(\nabla \delta \boldsymbol{u}\right) \boldsymbol{I}
\end{aligned}$$

$$\begin{aligned}
&= \frac{\mu}{6} \left(\nabla \delta \boldsymbol{u} + \left(\nabla \delta \boldsymbol{u}\right)^T + \left(\nabla \delta \boldsymbol{u}\right)^T \cdot \nabla \delta \boldsymbol{u} \right) \\
&\quad + \left[\left(\frac{\kappa}{2} - \frac{10\mu}{18} \right) \mathrm{tr}\left(\nabla \delta \boldsymbol{u}\right) - \frac{\mu}{6} \mathrm{tr}\left(\left(\nabla \delta \boldsymbol{u}\right)^T \cdot \nabla \delta \boldsymbol{u} \right) \right] \boldsymbol{I}
\end{aligned}$$

And finally

$$\begin{aligned}\delta \boldsymbol{S} = & \frac{\mu}{6}\left(\nabla\delta\boldsymbol{u} + (\nabla\delta\boldsymbol{u})^T + (\nabla\delta\boldsymbol{u})^T \cdot \nabla\delta\boldsymbol{u}\right) \\ & + \left[\left(\frac{\kappa}{2} - \frac{10\mu}{18}\right)\mathrm{tr}\left(\nabla\delta\boldsymbol{u}\right) - \frac{\mu}{6}\mathrm{tr}\left((\nabla\delta\boldsymbol{u})^T \cdot \nabla\delta\boldsymbol{u}\right)\right]\boldsymbol{I}\end{aligned} \tag{2}$$

A.1 Neo-Hookean Updated Lagrangian solver

The linear momentum conservation equation, Eqn. 2.8

$$\int_{V_u} \rho_u \frac{\partial \delta \boldsymbol{v}}{\partial t} \mathrm{d}V_u = \oint_{S_u} \boldsymbol{n}_u \cdot \left(\delta\boldsymbol{S} + \boldsymbol{S}\cdot\delta\boldsymbol{F}^T + \delta\boldsymbol{S}\cdot\delta\boldsymbol{F}^T\right)\mathrm{d}S_u,$$

is solved iteratively in OpenFOAM applying Gauss' theorem

$$\rho\frac{\partial^2\delta\boldsymbol{u}}{\partial t^2} = \nabla\cdot\left(\delta\boldsymbol{S} + \boldsymbol{S}\cdot\delta\boldsymbol{F}^T + \delta\boldsymbol{S}\cdot\delta\boldsymbol{F}^T\right),$$

where $\boldsymbol{S}$ is the total 2nd Piola-Kirchhoff stress tensor at the beginning of the time step given by Eqn. 1, $\delta\boldsymbol{S}$ is the incremental 2nd Piola-Kirchhoff stress given by Eqn. 2 and $\delta\boldsymbol{F}^T = \nabla\delta\boldsymbol{u}$.

```
int iCorr = 0;
do
{ //solves for incremental displacement DU using Newton second
   law
  fvVectorMatrix DUEqn =
  (
    rho*fvm::d2dt2(DU) ==
          fvm::laplacian(mu/6.0 + kappa, DU)
        + fvc::div(
             - kappa*gradDU //this helps convergence as in
                Tukovic2007 [103]
             + (mu/6.0) * (gradDU.T())
             + I*((kappa/2.0) - 10.0*mu/18.0) * tr(gradDU)
             + (mu/6.0) * (gradDU & gradDU.T())
             - I*(mu/6.0) * tr(gradDU & gradDU.T())
             + ((sigma + DSigma) & gradDU),
           )
  );
```

```
    solverPerf = DUEqn.solve();
    DU.relax();
    if(iCorr == 0)
    {
        initialResidual = solverPerf.initialResidual();
    }

  //update the value of gradDU
  gradDU = fvc::grad(DU);

  //calculate DSigma using the constitutive equation
  DEpsilon = symm(gradDU) + 0.5*symm(gradDU & gradDU.T());
  DC = 2*DEpsilon;
  DSigma = (mu/6.0)*DC
      + I*((kappa/2.0) - 10.0*mu/18.0) * tr(gradDU)
      - I*((mu/6.0) * tr(gradDU & gradDU.T()));

  # include "calculateRelativeResidual.H"
}
while
(
  solverPerf.initialResidual() > convergenceTolerance
  && relativeResidual > convergenceTolerance
  && ++iCorr < nCorr
);

#     include "moveMesh.H" //update the mesh to the new
    calculated position
//update the total quantities
volTensorField F = I + gradDU;
U += DU;
epsilon += DEpsilon;
sigma += DSigma;
J = det(F);
// and rotate the stress and strain tensors to the new
    configuration
rho = rho/J;
epsilon = symm(Finv & epsilon & Finv.T());
sigma  = 1/J * symm(F.T() & sigma & F);
```

Appendix B

PIMPLE algorithm for the fluid solver

```
//solveFluid.H
Info<< "Solving␣Fluid␣\n" << endl;
        if (mesh.moving() && checkMeshCourantNo)
        {
        Info<< "\n␣Correct␣mesh␣Courant␣Number␣\n" << endl;
#           include "meshCourantNo.H"
        }

//         Mesh motion update
        if (correctPhi)
        {
        Info<< "Correct␣phi␣\n" << endl;
#           include "correctPhi.H"
        }

#       include "CourantNo.H"

        // Make the fluxes relative to the mesh motion
        fvc::makeRelative(phi, U);    //from pimpleDyMFoam

        // --- PIMPLE loop
        label oCorr = 0;
```

```
        Info<< "\nOuter␣Corrections␣(PIMPLE␣loop):␣" <<
           nOuterCorr <<"␣-----****" <<endl;
        do
        {
            if (nOuterCorr != 1)
            {
                p.storePrevIter();
            }

#           include "UEqn.H"

            // --- PISO loop
            for (int corr = 0; corr < nCorr; corr++)
            {
              Info<< "\n␣pisoCorrection:␣" << corr << endl;

                rAU = 1.0/UEqn.A();

                U = rAU*UEqn.H();
                phi = (fvc::interpolate(U) & mesh.Sf());

                adjustPhi(phi, U, p);

                for (int nonOrth=0; nonOrth<=nNonOrthCorr;
                   nonOrth++)
                {

              Info<< "\n␣nonOrthogonal␣correction:␣" << nonOrth
                 << endl;

                    fvScalarMatrix pEqn
                    (
                        fvm::laplacian(rAU, p) == fvc::div(phi)
                    );

                    pEqn.setReference(pRefCell, pRefValue);

                    if
                    (
```

```
//                          oCorr == nOuterCorr - 1
                        corr == nCorr - 1
                     && nonOrth == nNonOrthCorr
                    )
                    {
                        pEqn.solve
                        (
                            mesh.solutionDict().solver(p.name()
                                + "Final")
                        );
                    }
                    else
                    {
                        pEqn.solve(mesh.solutionDict().solver(p.
                            name()));
                    }

                    if (nonOrth == nNonOrthCorr)
                    {
                        phi -= pEqn.flux();
                    }
                }

#               include "continuityErrs.H"

                // Explicitly relax pressure for momentum
                    corrector
                if (oCorr != nOuterCorr - 1)
                {
                    p.relax();
                }

                // Make the fluxes relative to the mesh motion
                fvc::makeRelative(phi, U);

#               include "movingMeshContinuityErrs.H"

                U -= rAU*fvc::grad(p);
                U.correctBoundaryConditions();
```

```
            }

            turbulence->correct();
        } while (++oCorr < nOuterCorr);
```

Appendix C

Subset mesh motion

Even though explaining the file structure of an OpenFOAM simulation goes beyond the purpose of this thesis, a brief overview is given here in order to show the original work done by the author. For a more complete explanation the reader should refer to the OpenFOAM website.

The file structure of a FSI case solved with `icoFSIelasticNonLinULSolidFoam` looks like the following

```
|----0
|     |----p
|     |----U
|     |----motionU
|     |----solid
|          |----DU
|----system
|     |----controlDict
|     |----fvSchemes
|     |----fvSolution
|     |----tetFemSolution
|     |----solid
|          |-----fvSchemes
|          |-----fvSolution
|----constant
     |----polyMesh
```

```
|----RASProperties
|----transportProperties
|----dynamicMeshDict
|----solid
     |----polyMesh
     |----physicalProperties
     |----rheologyProperties
```

The **0** folder holds information about the initial conditions for the field variables to be solved. The **system** folder contains all the information about the discretization schemes (`fvSchemes`), linear solvers (`fvSolution`) and process (`controlDict`). The **constant** folder contains the mesh (**polyMesh**) and the physical properties. Each of this folders contains the **solid** subfolder where the settings for the solid solver are located.

When the simulation starts the mesh objects for the fluid and solid are created at runtime and the relative field variables are stored in an array having the same size of their respective cell count. The `motionU` field is the array where the displacement for each cell is stored and it has the size of the whole fluid mesh. Since the displacement of the mesh points far away from the membrane is negligible it is more convenient to solve the Laplace smoothing equation only in a small mesh subset in order to save memory and computational time.

The class `subsetMotionSolverFvMesh` is present in the OpenFOAM-extend version, however in order to use it some modifications to the file structure and the source code of `icoFSIelasticNonLinULSolidFoam` need to be done. The new file structure is modified as follow

```
|----0
|     |----p
|     |----U
|     |----motionSubset
|     |     |----motionU
|     |----solid
|          |----DU
|----system
|     |----controlDict
```

```
|     |----fvSchemes
|     |----fvSolution
|     |----motionSubset
|     |     |----tetFemSolution
|     |----solid
|          |-----fvSchemes
|          |-----fvSolution
|----constant
     |----polyMesh
     |----RASProperties
     |----transportProperties
     |----dynamicMeshDict
     |----motionSubset
     |     |----polyMesh
     |     |----dynamicMeshDict
     |----solid
          |----polyMesh
          |----physicalProperties
          |----rheologyProperties
```

The subfolder **motionSubset** contains the coordinates of the points to be moved around the membrane along with the relative dictionary and linear solver settings. However this folder is not seen by the fluid solver and in order to access its information a `motionMesh` object needs to be created at runtime. This is done adding the following line in the main function of the FSI solver

```
const fvMesh& motionMesh =
    runTime.objectRegistry::
    lookupObject<fvMesh>("motionSubset");
```

In addition, the `motionU` field needs to be initialised as belonging to the new `motionMesh` object registry

```
tetPointVectorField& motionU =
    const_cast<tetPointVectorField&>
    (
        motionMesh.objectRegistry::
```

```
        // mesh.objectRegistry:: // not in the fluid mesh
            registry anymore
        lookupObject<tetPointVectorField> ("motionU")
    );
```

Note that there are two dictionaries `dynamicMeshDict`. The one in **`constant`**/**`motionSubset`** contains the actual settings about the Laplace solver, whereas the one in the **`constant`** tells OpenFOAM that a `subsetMotionSolverFvMesh` will be used and what is the addressing between points in the fluid mesh and subset mesh so the position of the points in the fluid mesh can be updated accordingly.

Appendix D

Structural code: calculate prestretch and Maxwell stress at the beginning of the FSI simulation

```
//poisson ratio
scalar nuPoisson = average((3.0*kappa - 2.0*mu)/(6.0*kappa +
    2.0*mu)).value(); //calculate the average because kappa and
    mu are volScalarField

//read from dictionary the type of prestretch and the prestretch
     value
word  stretchType (rheologyProperties.lookup("prestretch")); //
    uniaxial or equibiaxial
scalar  lambda_pre(readScalar(rheologyProperties.lookup("
    prestretchValue")));

//assign prestretch values to the prestretch tensor
tensor  prestretch = I;
if(stretchType == "uniaxial")
{
  prestretch.xx() = lambda_pre;
  prestretch.yy() = Foam::pow(lambda_pre,-nuPoisson);
```

```
  prestretch.zz() = Foam::pow(lambda_pre,-nuPoisson);
}
else if(stretchType == "equibiaxial")
{
  prestretch.xx() = lambda_pre;
  prestretch.yy() = lambda_pre;
  prestretch.zz() = Foam::pow(lambda_pre,-(1.0/nuPoisson));
}

//assign the prestretch value to the deformation tensor field
volTensorField F
(
  IOobject
  (
    "F",
    runTime.timeName(),
    mesh,
    IOobject::NO_READ,
    IOobject::AUTO_WRITE
   ),
   mesh,
   prestretch //I + fvc::grad(DU);
);

//volume ratio
volScalarField J = det(F);

//Green-Lagrangian strain tensor
epsilon = symm(0.5*((F.T() & F) - I));

//Right Cauchy-Green strain tensor
volSymmTensorField C = 2.0*epsilon + I;

if(hyperElasticModel == "Neo-Hookean") //compressible Neo-
    Hookean model
{
  //calculate the Cauchy stress tensor as we already know the
      final configuration
  sigma =   ((mu/2.0)/pow(J,(-2.0/3.0)))
```

```
                *(I - (tr(C)/3.0)*inv(C))
      + (kappa/2.0)*(J-1)*J*inv(C);
}
else if(hyperElasticModel == "SaintVenant-Kirchhoff")
{
  sigma = 2*mu*epsilon + I*(lambda*tr(epsilon));
}

////**** ELECTROSTATICS ****\\\\
//reading the phi boundary condition
volScalarField phi
(
  IOobject
  (
    "phi",
    runTime.timeName(),
    mesh,
    IOobject::MUST_READ,
    IOobject::AUTO_WRITE
  ),
  mesh
);

//Gauss' Law
solve
(
  fvm::laplacian(phi) + rhoE/epsilon0
);
//Electric field
E = -fvc::grad(phi);
//Maxwell stress tensor
sigmaE = epsilon0*symm(E * E - 0.5*(E & E) * I); //this is
    cauchy stress

//Sum up mechanical and Maxwell stress tensor
sigma += sigmaE;
```

Bibliography

[1] R. Albertani, B. Stanford, and P. Hubner, J.and Ifju. Aerodynamic coefficients and deformation measurements on flexible micro air vehicle wings. *Experimental Mechanics*, 47:625–635, 2007.

[2] I. Anderson, T. Hale, T. Gisby, T. Inamura, T. McKay, B. O'Brien, S. Walbran, and E. Calius. A thin membrane artificial muscle rotary motor. *Applied Physics*, 98:75–83, 2010.

[3] J. D. Anderson Jr. *Fundamentals of Aerodynamics*. McGraw-Hill Inc., 1991.

[4] S. Arbos, Z. Pang, B. Ganapathisubramani, and R. Palacios. Leading and trailing edge effects on the aeromechanics of membrane aerofoils. In *Preprint submitted to Journal of Fluids and Structures*, February 2012.

[5] E.M. Arruda and M.C. Boyce. A three-dimensional constitutive model for the large stretch behavior of rubber elastic materials. *J. Mech. Phys. Solids*, 41:389–412, 1993.

[6] M. Astorino, F. Chouly, and M.A. and Fernandez. Robin based semi-implicit coupling in fluid-structure interaction: stability analysis and numerics. *SIAM J. Sci. Comput.*, 31:4041–4065, 2009.

[7] M.M. Attard and G.W. Hunt. Hyperelastic constitutive modeling under finite strain. *Int. J. Solid Struct.*, 41:5327–5330, 2004.

[8] B. Augier, P. Bot, F. Hauville, and D. Mathieu. Dynamic behaviour of a flexible yacht sail plan. *Ocean Engineering*, 66:32–43, 2013.

[9] I. Babuska and M. Suri. Locking effects in the finite element approximation of elasticity problems. *Numer. Math*, 62:439–463, 1992.

[10] H. Baek and G. E. Karniadakis. A convergence study of a new partitioned fluid-structure interaction algorithm based on fictitious mass and damping. *Journal of Computational Physics*, 231:629–652, 2012.

[11] S. Banerjee. *3-dimensional Effects on Flag Flapping Dynamics*. PhD thesis, MIT, Department of Mechanical Engineering, 2013.

[12] P.W. Bearman. Vortex shedding from oscillating bluff bodies. *Annual Review of Fluid Mechanics*, 16:195–222., 1984.

[13] M. Beck, R. Fiolka, and A. Stemmer. Variable phase retarder made of a dielectric elastomer actuator. *Optic Letters*, 34:803–805, 2009.

[14] I. Bijelonja, I. Demirdzic, and S. Muzaferija. A finite volume method for large strain analysis of incompressible hyperelastic materials. *International Journal for Numerical Methods in Engineering*, 64:1594–1609, 2005.

[15] K.L. Bishop. The relationship between 3-d kinematics and gliding performance in the southern flying squirrel, glaucomys volans. *J Exp Biol*, 4:689–701, 2006.

[16] R. Bourguet, G. E. Karniadakis, and M.S. Triantafyllou. Lock-in of the vortex-induced vibrations of a long tensioned beam in shear flow. *Journal of Fluid and Structures*, 27:838–847, 2011.

[17] T. Bower. *The PID Controller*. LabVIEW Robotics Programming Guide, 2015.

[18] P. Brochu and Q. Pei. Advances in dielectric elastomers for actuators and artificial muscles. *Macromol. Rapid Commun.*, 31:10–36, 2010.

[19] S. L. Brunton and C. W. Rowley. Modeling the unsteady aerodynamic forces on small-scale wings. *47th AIAA Aerospace Sciences Meeting*, 2009.

[20] E. Burman and M.A. Fernandez. Stabilization of explicit coupling in fluid-structure interaction involving fluid incompressibility. *Comput Methods Appl Mech Eng*, 198:766–784, 2009.

[21] R. L. Campbell. *Fluid-structure interaction and inverse design simulations for flexible turbomachinery*. PhD thesis, The Pennsylvania State University, 2010.

[22] P. Cardiff. *Development of the Finite Volume Method for Hip Joint Stress Analysis*. PhD thesis, University College Dublin, 2012.

[23] P. Cardiff, A. Karac, and A. Ivankovic. A large strain finite volume method for orthotropic bodies with general material orientations. *Comput Methods Appl Mech Eng*, 268:318–335, 2014.

[24] B.H. Carmichael. Low reynolds number airfoil survey. Technical report, NASA CR-165803, 1982.

[25] F. Carpi, S. Bauer, and D. De Rossi. Stretching dielectric elastomer performance. *Science*, 330:1759–1761, 2010.

[26] P. Causin, J.F. Gerbeau, and F. Nobile. Added-mass effect in the design of partitioned algorithms for fluid-structure problems. *Comput. Methods Appl. Mech. Eng.*, 194:4506–4527, 2005.

[27] G. Cetraro and R. Sandberg. High fidelity simulations of electroactive membrane wings. In *AIAA SciTech*, 2015. doi: 10.2514/6.2015-1301. URL http://arc.aiaa.org/doi/abs/10.2514/6.2015-1301.

[28] G. Cetraro and R. Sandberg. Fluid-structure interaction simulations of a membrane wing with variable compliance. In *AIAA SciTech*, 2016. doi: 10.2514/6.2016-1351. URL http://arc.aiaa.org/doi/abs/10.2514/6.2016-1351.

[29] J.A. Cheney, N. Konow, K.M. Middleton, K.S. Breuer, T.J. Roberts, E.L. Giblin, and S.M. Swarts. Membrane muscle function in the compliant wings of bats. *Bioinspiration & Biomimetics*, 9:025007, 2014.

[30] Hemisphere Publishing Corporation, editor. *Numerical heat transfer and fluid flow*. Patankar, S.V., 1981.

[31] Oscar M. Curet, Alex Carrere, Rye Waldman, and Kenneth S. Breuer. Aerodynamic characterization of a wing membrane with variable compliance. *AIAA Journal*, 52:1749–1756, 2014. URL http://dx.doi.org/10.2514/1.J052688.

[32] J. De Hart, G. Peters, P. Schreurs, and F. Baaijens. A three-dimensional computational analysis of fluid-structure interaction in the aortic valve. *Journal of Biomechanics*, 36:103–112, 2003.

[33] I. Demirdzic and D. Martinovic. Finite volume method for thermo-elasto-plastic stress analysis. *Comput Methods Appl Mech Eng*, 109: 331–349, 1993.

[34] I. Demirdzic and M. Peric. Space conservation law in finite volume calculations of fluid flow. *Int. J. Num. Meth. Fluids*, 8:1037–1050, 1988.

[35] J. Barbic E. Sifakis. *Finite Element Method Simulation of 3D Deformable Solids*. Morgan & Claypool, 2015.

[36] N. Fallah, C. Bailey, M. Cross, and C. A. Taylor. Comparison of finite element and finite volume methods application in geometrically non-linear stress analysis. *Applied Mathematical Modelling*, 24: 439–455, 2000.

[37] C. Farhat, P. Geuzaine, and G. Brown. Application of a three-field nonlinear fluid-structure formulation to the prediction of the aeroelastic parameters of an f-16 fighter. *Computers and Fluids*, 32:3–29, 2003.

[38] C. Farhat, K.G. van der Zee, and P. Geuzaine. Provably second-order time-accurate loosely-coupled solution algorithms for transient nonlinear computational aeroelasticity. *Comput. Methods Appl. Mech. Eng*, 195:1973–2001, 2006.

[39] C. Felippa, K. Park, and C. Farhat. Partitioned analysis of coupled mechanical systems. *Computer Methods in Applied Mechanics and Engineering*, 190:3247–3270, 2001.

[40] M.A. Fernandez and M. Moubachir. A newton method using exact jacobians for solving fluid-structure coupling. *Comput. Struct*, 83: 127–142, 2005.

[41] M.A. Fernandez, J.F. Gerbeau, and C. Grandmont. A projection semi-implicit scheme for the coupling of an elastic structure with an incompressible fluid. *Int. J. Numer. Methods Eng.*, 69:794–821, 2007.

[42] P. J. S. A. Ferreira De Sousa and J. J. Allen. Thrust efficiency of harmonically oscillating flexible flat plates. *Journal of Fluid Mechanics*, 674:43–66, May 2011. doi: 10.1017/S0022112010006373.

[43] J. H. Ferziger and M. Peric. *Computational Methods for Fluid Dynamics*. Springer-Verlag Berlin, 2002.

[44] C.A. Figueroa, Vignon-Clementel I.E., K.E. Jansen, T. J. R. Hugues, and C. A. Taylor. A coupled momentum method for modeling blood flow in three-dimensional deformable arteries. *Comput. Methods Appl. Mech. Eng*, 195:5685–5706, 2006.

[45] V.L. Finkenstadt. Natural polysaccharides as electroactive polymers. *Applied Microbiology and Biotechnology*, 67:735–745, 2005.

[46] C. Förster, W. A. Wally, and E.s Ramm. Artificial mass instabilities in sequential staggered coupling of nonlinear structures and incompressible viscous flows. *Comput Methods Appl Mech Eng*, 196:1278–1293, 2007. URL http://www.sciencedirect.com/science/article/pii/S0045782506002544#.

[47] Jacquet-Richardet G. and Rieutord P. A three-dimensional fluid-structure coupled analysis of rotating flexible assemblies of turbomachines. *Journal of Sound and Vibration*, 209:61–76, 1998.

[48] R. Galvao, E. Israeli, A. Song, X. Tian, K. Bishop, S. Swartz, and K. Breuer. The aerodynamics of compliant membrane wings modelled on mammalian flight mechanics. *Fluid Dynamics*, 2866:1–12, 2006.

[49] M.W. Gee, U. Küttler, and W.A. Wall. Truly monolithic algebraic multigrid for fluidstructure interaction. *Int. J. Numer. Methods Eng.*, 8:987–1016, 2011.

[50] J. Gerbeau, M. Vidrascu, and P. Frey. Fluid-structure interaction in blood flows on geometries based on medical imaging. *Computers and Structures*, 83:155–165, 2005.

[51] R. E. Gordnier. High fidelity computational simulation of a membrane wing airfoil. *Journal of Fluids and Structures*, 25(5):897–917, 2009. ISSN 0889-9746. URL http://www.sciencedirect.com/science/article/pii/S088997460900036X.

[52] I.S. Grant and W.R. Phillips. *Electromagnetism (2nd Edition)*. Manchester Physics, 2008.

[53] C. Greenshields and H. Weller. A unified formulation for continuum mechanics applied to fluid-structure interaction in flexible tubes. *International Journal for Numerical Methods in Engineering*, 64:1575–1593, 2005.

[54] C.J. Greenshields, H.G. Weller, and A. Ivankovic. A finite volume formulation for fluid structure interaction. In *Problems and Perspectives, Finite Volumes for Complex Applications, vol. II,*. Hermes Science, 1999.

[55] G.A. Holzapfel. *Nonlinear Solid Mechanics*. 2001.

[56] Tobias Holzmann. *Mathematics, Numerics, Derivations and OpenFOAM*. Holzmann CFD, 2014.

[57] J. Hron and S. Turek. A monolithic fem/multigrid solver for ale formulation of fluid-structure interaction with applications in biomechanics. *Lecture Notes in Computational Science and Engineering*, 53: 146–170, 2006.

[58] J. Huang, T. Li, C.C. Foo, J. Zhu, D. Clarke, and Z. Suo. Giant, voltage-actuated deformation of a dielectric elastomer under dead load. *Appl. Phys. Lett.*, 100:041911, 2012.

[59] J. Hubner, E. Walhorn, and D. Dinkler. A monolithic approach to fluid-structure interaction using space-time finite elements. *Computer methods in applied mechanics and engineering*, 193:2087–2104, 2004.

[60] S.R. Idelsohn and E. Onate. Finite volumes and finite elements: two "good friends". *International Journal for Numerical Methods in Engineering*, 37:3323–3341, 1994.

[61] D. Ishihara and S. Yoshimura. A monolithic approach for interaction of incompressible viscous fluid and an elastic body based on fluid pressure poisson equation. *International Journal for Numerical Methods in Engineering*, 64:167–203, 2005.

[62] R.I. Issa. Solution of the implicitly discretized fluid flow equations by operator-splitting. *J. Comp. Physics*, 62:40–65, 1986.

[63] H. Jasak and Z. Tukovic. Automatic mesh motion for the unstructured finite volume method. *Transactions of FAMENA*, 30:n2, 2007.

[64] H. Jasak and H. G. Weller. Application of the finite volume method and unstructured meshes to linear elasticity. *International Journal for Numerical Methods in Engineering*, 48(2):267–287, 2000. ISSN 1097-0207. URL http://dx.doi.org/10.1002/(SICI)1097-0207(20000520)48:2<267::AID-NME884>3.0.CO;2-Q.

[65] Hrvoje Jasak. *Error Analysis and Estimation for the Finite Volume Method with Applications to Fluid Flows*. PhD thesis, Imperial College, 1996.

[66] J. W. Jaworski and R. E. Gordnier. High-order simulations of low reynolds number membrane airfoils under prescribed motion. *Journal of Fluids and Structures*, 31(0):49–66, 2012. ISSN 0889-9746. URL http://www.sciencedirect.com/science/article/pii/S0889974612000801.

[67] R. Kamakoti and W. Shyy. Fluid-structure interaction for aeroelastic application. *Progress in Aerospace Sciences*, 40:535–558, 2004.

[68] A. Karac. *Drop impact of fluid-filled polyethytlene containers*. PhD thesis, Imperial College, University of London, 2003.

[69] A. Kelly and M.J. O'Rourke. Fluid, solid and fluid-structure interaction simulations on patient-based abdominal aortic aneurysm models. *Proc. Inst. Mech. Eng. Part H*, 226:288–304, 2012.

[70] C. Keplinger, T. Li, R. Baumgartner, Z. Suo, and S. Bauer. Harnessing snap-through instability in soft dielectrics to achieve giant voltage-triggered deformation. *Soft Matter*, 8:285–288, 2012.

[71] A. Khalak and C.H.K. Williamson. Motions, forces and mode transitions in vortex-induced vibrations at low mass-damping. *Journal of Fluid and Structures*, 13:813–851, 1999.

[72] Myke King. *Process Control: A Practical Approach*. 2010.

[73] G. Kofod, R. Kornbluh, R. Pelrine, and P. S. Larsen. Actuation response of polyacrylate dielectric elastomer. *J. Intell. Mater. Syst. Struct.*, 14:787–793, 2003.

[74] S. J. A. Koh, T. Li, J. Zhou, X. Zhao, W. Hong, J. Zhu, and Z. Suo. Mechanisms of large actuation strain in dielectric elastomers. *J. Polym. Sci, Part B: Polym. Phys.*, 49:504–515, 2011.

[75] R. Kornbluh, R. Pelrine, J. Joseph, R. Heydt, Q. Pei, and S. Chiba. High-field electrostriction of elastomeric polymer dielectrics for actuation. *Proc. SPIE*, 3669:149–161, 1999.

[76] Y. Lian and W. Shyy. Laminar-turbulent transition of a low reynolds number rigid or flexible airfoil. *AIAA Journal*, 45:1501–1513, 2007.

[77] Y. Lian, W. Shyy, D. Viieru, and B. Zhang. Membrane wing mechanics for micro air vehicles. *Progress in Aerospace Sciences*, 39:425–465, 2003.

[78] Z. Lilek and M Peric. A fourth-order finite volume method with collocated variable arrangement. *Computers and Fluids*, 24(3):239–252, 1995.

[79] M. Lombardi, N. Parolini, A. Quarteroni, and G. Rozza. Numerical simulation of sailing boats: Dynamics, fsi, and shape optimization. In *Variational Analysis and Aerospace Engineering: Mathematical Challenges for Aerospace Design*. Springer, 2012.

[80] T. Lu, J. Huang, C. Jordi, G. Kovacs, R. Huang, D. Clarke, and Z. Suo. Dielectric elastomer actuators under equal-biaxial forces, uniaxial forces, and uniaxial constraint of stiff fibers. *Soft Matter*, 8:6167, 2012.

[81] Lawrence E. Malvern. *Introduction to the Mechanics of a Continuous Medium*. Prentice-Hall, 1969.

[82] K. Maneeratana. *Development of the finite volume method for non-linear structural applications*. PhD thesis, Imperial College, University of London, 2000.

[83] K. Maneeratana and A. Ivankovic. Finite volume method for large deformation with linear hypoelastic materials. In *Finite Volumes for Complex Applications II*. HERMES Science, 1999.

[84] H.G. Matthies and J. Steindorf. Partitioned but strongly coupled iteration schemes for nonlinear fluid-structure interaction. *Comput. Struct.*, 80:27–30, 2002.

[85] W. J. McCroskey. The phenomenon of dynamic stall. *NASA TM 81264*, 1981.

[86] C. Michler, S. Hulshoff, E. van Brummelen, and de Borst R. A monolithic approach to fluid-structure interaction. *Computer and Fluids*, 33:839–848, 2004.

[87] D. Mok, W. Wall, and E. Ramm. Accelerated iterative substructuring schemes for instationary fluid-structure interaction. In USA) Elsevier, Cambridge (MA, editor, *First MIT Conference on Computational Fluid and Solid Mechanics*, pages 1325–1328, 2001.

[88] M. Mooney. A theory of large elastic deformation. *Journal of Applied Physics*, 11(9):582–592, 1940. URL http://scitation.aip.org/content/aip/journal/jap/11/9/10.1063/1.1712836.

[89] A. M. Mountcastle and S.A. Combes. Wing flexibility enhances load-lifting capacity in bumblebees. *Proc. R. Soc B*, 280, 2013.

[90] B.G. Newman. Aerodynamic theory for membranes and sails. *Prog Aerosp Sci*, 24:1–27, 1987.

[91] R. W. Odgen. *Nonlinear Elastic Deformations*. 1984.

[92] R.W. Odgen. Large deformation isotropic elasticity on the correlation of theory and experiment for incompressible rubberlike solids. *Proc. R. Soc. Lond. A Math. Phys. Sci.*, 326:565–584, 1972.

[93] K. Park, C. Felippa, and J. De Runtz. Stabilization of staggered solution procedures for fluid-structure interaction analysis. *AMD*, 26: 95–124, 1977.

[94] S.V. Patankar and D.B. Spalding. A calculation procedure for heat, mass and momentum transfer in three-dimensional parabolic flows. *International Journal of Heat and Mass Transfer*, 15:1787–1806, 1972.

[95] R. Pelrine, R. Kornbluh, Q.B. Pei, and J. Joseph. High-speed electrically actuated elastomers with strain greater than 100%. *Science*, 287: 836–839, 2000.

[96] R. Pelrine, R. Kornbluh, Q. Pei, B. Stanford, S. Oh, J. Eckerle, R. Full, M. Rosenthal, and K. Mejer. Dielectric elastomer artificial muscle actuators: toward biomimetic motion. *Proc. SPIE*, 126, 2002.

[97] R.W. Penn. Volume changes accompanying the extension of rubber. *Transactions of the Society of Rheology*, 14(4):509–517, 1970.

[98] The OpenFOAM Extend Project. http://www.extend-project.de. 2014.

[99] A. Quaini and A. Quarteroni. A semi-implicit approach for fluid-structure interaction based on an algebraic fractional step method. *M3AS*, 17:957–983, 2007.

[100] A. Quarteroni, M. Tuveri, and A. Veneziani. Computational vascular fluid dynamics: problems, models and methods. *Comput. Visual Sci. 2*, 4:163–197, 2000.

[101] Debabrata Ray. *Computation of Nonlinear Structures: Extremely Large Elements for Frames, Plates and Shells*. John Wiley & Sons, Ltd., Chichester, 2015.

[102] R.S. Rivlin. Large elastic deformations of isotropic materials. iv. further developments of the general theory. *Philos. TRans. R. Soc. A*, 241:379–397, 1948.

[103] P. Rojratsirikul, Z. Wang, and I. Gursul. Unsteady fluid-structure interactions of membrane airfoils at low reynolds numbers. *Experiments in Fluids*, 46:859–872, 2009.

[104] S. Sane. The aerodynamics of insect flight. *J. Exp. Biol.*, 206:4191–4208, 2003.

[105] T. Sawada and T. Hisada. Fluid-structure interaction analysis of a two-dimensional flag-in-wind problem by the ale finite element method. *JSME International Journal Series A*, 49:170–179, 2006.

[106] M. Schafer. *Computational Engineering - Introduction to Numerical Methods*. Springer, 2006.

[107] W. E. Schiesser. *The Numerical Method of Lines*. 1991.

[108] W. Shyy and R. Smith. A study of flexible airfoil aerodynamics with application to micro aerial vehicles. *AIAA*, 1933, 1997.

[109] W. Shyy, F. Kelvebring, M. Nilsson, J. Sloan, B. Carroll, and C. Fuentes. Rigid and flexible low reynolds number airfoils. *Journal of Aircraft*, 36, 1999.

[110] W. Shyy, P. Ifju, and D. Viieru. Membrane wing-based micro air vehicles. *Applied Mechanics Reviews*, 58:283–301, 2005.

[111] W. Shyy, B. Stanford, P. Ifju, and R. Albertani. Fixed membrane wings for micro air vehicles: Experimental characterisation, numerical modelling and tailoring. *Progress in Aerospace Sciences*, 44:258–294, 2008.

[112] A. K. Slone, K. Pericleous, C. Bailey, M. Cross, and C. Bennett. A finite volume unstructured mesh approach to dynamic fluid-structure interaction: an assessment of the challenge of predicting the onset of flutter. *Applied mathematical modelling*, 28:211–239, 2004.

[113] A.K. Slone, C. Bailey, and M. Cross. Dynamic solid mechanics using finite volume methods. *Applied Mathematical Modeling*, 27:69–87, 2003.

[114] R. Smith and W. Shyy. Computational model of flexible membrane wings in steady laminar flow. *AIAA Journal*, 33(10):1769–1777, 1995.

[115] R. Smith and W. Shyy. Computation of unsteady laminar flow over a flexible two-dimensional membrane wing. *Physics of Fluids*, 9:2175–2184, 1995.

[116] R. Smith and W. Shyy. Computation of aerodynamic coefficients for a flexible membrane airfoil in turbulent flow: a comparison with classical theory. *Phys Fluids*, 8:3346–3353, 1996.

[117] S. Son and N.C. Goulbourne. Dynamic response of tubular dielectric elastomer transducers. *International Journal of Solids and Structures*, 47:2672–2679, 2010.

[118] A. Song and K. Breuer. Dynamics of a compliant membrane as related to mammalian flight. *AIAA Paper*, 41:1257–1265, 2004.

[119] A. Song, X. Tian, E. Israeli, R. Galvao, K. Bishop, S. Swartz, and K. Breuer. Aeromechanics of membrane wings with implications for animal flight. *AIAA Journal*, 46:2096–2196, 2008.

[120] K. Stein, R. Benney, V. Kalro, T. Tezduyar, J. Leonard, and M. Accorsi. Parachute fluid-structure interactions: 3-d computation. *Computer Methods in Applied Mechanics and Engineering*, 190:373–386, 2000.

[121] J. Steindorf and H. Matthies. Numerical efficiency of different partitioned methods for fluid-structure interaction. *Journal of Applied Mathematics and Mechanics*, 2:557–558, 2000.

[122] Z. Suo. Theory of dielectric elastomers. *Acta Mecanica Solida Sinica*, 23:549–578, 2010.

[123] S.M. Swartz, J. Iriarte-Diaz, D.K. Riskin, A. Song, X. Tian, D. Willis, and K.S. Breuer. Wing structure and the aerodynamic basis of flight in bats. *Proceedings of the 45th AIAA aerospace sciences meeting and exhibit*, 42, 2007.

[124] V.L. Tagarielli, R. Hildick-Smith, and J.E. Huber. Electro-mechanical properties and electrostriction response of a rubbery polymer for

eap applications. *International Journal of Solids and Structures*, 49: 3409–3415, 2012.

[125] C. A. Taylor, T. J. R. Hugues, and C. K. Zarins. Finite element modeling of blood flow in arteries. *Computer methods in applied mechanics and engineering*, 158:155–196, 1998.

[126] G.A. Taylor, C. Bailey, and M. Cross. Solution of the elastic/viscoplastic constitutive equations: a finite volume approach. *Applied Mathematical Modeling*, 19:746–760, 1995.

[127] T. Tezduyar, S. Sathe, R. Keedy, and K. Stein. Space-time finite element techniques for computation of fluid-structure interactions. *Comput. Methods Appl. Mech. Eng.*, 195:2002–2027, 2006.

[128] T. Tezduyar, S. Sathe, T. Cragin, B. Nanna, B.S. Conklin, J. Pausewang, and M. Schwaab. Modelling of fluid-structure interactions with the space-time finite elements: arterial fluid mechanics. *International Journal for Numerical Methods in Fluids*, 54:901–922, 2007.

[129] T. Theodorsen. General theory of aerodynamic instability and the mechanics of flutter. *NACA Report*, 496:413–433, 1935.

[130] L. Tregidgo, Z. Wang, and I. Gursul. Frequency lock-in phenomenon for self-sustained roll oscillations of rectangular wings undergoing a forced periodic pitching motion. *Physiscs of Fluids*, 24:117101, 2012.

[131] D. Trimarchi. *Analysis of downwind sail structures using non-linear shell finite elements*. PhD thesis, University of Southampton, June 2012.

[132] Z. Tukovic and H. Jasak. Updated lagrangian finite volume solver for large deformation dynamic response of elastic body. *Transactions of FAMENA*, 31 n1, 2007.

[133] S. Turek and J. Hron. Proposal for numerical benchmarking of fluid-structure interaction between an elastic object and laminar incompressible flow. *Lecture Notes in Computational Science and Engineering*, 53:371–385, 2006.

[134] K.S. Valanis and R.F. Landel. The strain-energy function of a hyperelastic material in terms of the extension ratios. *J. Appl. Phys.*, 7: 2997–3002, 1967.

[135] Vance J. Van, Doren. *Loop Tuning Fundamentals*. Reed Business Information, 2003.

[136] H Vangerko and L.R.G Treloar. The inflation and extension of rubber tube for biaxial strain studies. *Journal of Physics D: Applied Physics*, 11:1969–1978, 1978.

[137] H. Versteeg and W. Malalasekera. *An introduction to computational fluid dynamics: the finite volume method*. Pearson Education Ltd, 2007.

[138] J. Videler and E. Samhuis. Leading-edge vortex lifts swifts. *Science*, 306:1960–1962, 2004.

[139] J. Vierendeels, L. Lanoye, J. Degroote, and P. Verdonck. Implicit coupling of partitioned fluid-structure interaction with reduced order models. *Comput. Struct.*, 85:970–976, 2007.

[140] J. Vierendeels, K. Dumont, and P. Verdonck. A partitioned strongly coupled fluid-structure interaction method to model heart valve dynamics. *Journal of Computational and Applied Mathematics*, 215:602–609, 2008.

[141] William P. Walker and Mayuresh J. Patil. Unsteady aerodynamics of deformable thin airfoils. *Journal of Aircraft*, 51:1673–1680, 2014.

[142] W. A. Wall, C. Forster, M. Neumann, and E. Ramm. Advances in fluid-structure interaction. In *Proceedings of 17th international conference on the application of computer science and mathematics in architecture and civil engineering*, 2006.

[143] H. Weller, G. Tabor, H. Jasak, and C. Fureby. A tensorial approach to computational continuum mechanics using object orientated techniques. *Comput. Phys.*, 12:620–631, 1998.

[144] P. Wesseling. *Principles of Computational Fluid Dynamics*. Springer-Verlag Berlin, 2001.

[145] M. A. Wheel. Geometrically versatile finite volume formulation for plane strain elastostatic stress analysis. *Journal of Strain Analysis for Engeneering Design*, 31:111–116, 1996.

[146] C.H.K. Williamson and A. Roshko. Vortex formation in the wake of an oscillating cylinder. *Journal of Fluids and Structures*, 2:355–381, 1988.

[147] M. Wissler and E. Mazza. Modeling and simulation of dielectric elastomer actuators. *Smart Materials and Structures*, 14:1396–1402, 2005.

[148] B. Wolters, M. Rutten, Schurink G., U. Kose, J. De Hart, and F. Van De Vosse. A patient-specific computational model of fluid-structure interaction in abdominal aortic aneurysms. *Medical Engineering and Physics*, 27:871–883, 2005.

[149] G Xing-long, Z. Qing-bin, and T. Qian-gang. Fluid-structure interaction simulation of parachute in low speed airdrop. *Proceedings of the World Congress on Engineering*, 3, 2013.

[150] O.H. Yeoh. Some forms of the strain energy function for rubber. *Rubber Chem. Technol.*, 66:754–771, 1993.

[151] J. Young and J.C.S. Lai. Vortex lock-in phenomenon in the wake of a plunging airfoil. *AIAA Journal*, 45:485–490, 2007.

[152] J.G. Ziegler and N.B. Nichols. Optimum settings for automatic controllers. *Transactions of the ASME*, 64:759–768, 1942.

[153] O.C. Zienkiewicz and R.L. Taylor. *The Finite Element Method. Basic Formulation and Linear Problems*. McGraw-Hill, 1989.